学位論文

Systematic analysis of Ca^{2+}-regulatory mechanisms based on chemical-genetic interaction profiles of *Saccharomyces cerevisiae*

化合物‐遺伝子間相互作用プロファイルによる出芽酵母 Ca^{2+}制御機構の網羅的な解析

吉田　光範

Doctoral thesis

Systematic analysis of Ca^{2+}-regulatory mechanisms based on chemical-genetic interaction profiles of *Saccharomyces cerevisiae*

Mitsunori Yoshida

Department of Integrated Biosciences

Graduate School of Frontier Sciences

The University of Tokyo

2015

Table of contents

Acknowledgements

I would like to express my deepest appreciation to Prof. Yoshikazu Ohya for his constant supervision including constructive advice and insightful discussion, and patient encouragement throughout this study.

I would like to express my appreciation to Associate Prof. Kuninori Suzuki for his constructive advice and insightful discussion throughout this study.

I also express my appreciation to Dr. Satoru Nogami for constructive advice, insightful discussion, and technical support throughout this study.

I am grateful to Dr. Shinsuke Ohnuki for his advice, discussion, warm encouragement, and technical support particularly in statistical analyses throughout this study.

I am also grateful to Dr. Takahiro Negishi and Dr. Hiroki Okada for their advice, discussion, warm encouragement, and technical support throughout this study.

I would like to express my gratitude to Dr. Yoko Yashiroda for her experimental contributions to initial step of this study.

I thank all members of Laboratory of Signal Transduction, Department of Integrated Biosciences, Graduate School of Frontier Sciences, The University of Tokyo, for their warm encouragement throughout this study.

Finally, I thank my parents and grandparents from the bottom of my heart for their warm encouragement and financial support throughout this study.

List of tables

List of figures

Abbreviations

–Ca^{2+}: YPD medium treatment

+Ca^{2+}: YPD medium treatment supplemented with 100 mM $CaCl_2$

AIC: Akaike information criterion

ANCOVA: analysis of covariance

ANOVA: analysis of variance

AU *P* value: approximately unbiased probability value

C-VPS: class C vacuolar protein sorting

CCR: cumulative contribution ratio

CLS, *cls*: calcium-sensitive

CORVET: class C core vacuole/endosome tethering

CV: coefficient of variation

DAPI: 4',6-diamidino-2-phenylindole

ER: endoplasmic reticulum

FAD: flavin adenine dinucleotide

FITC-Con A: fluorescence isothiocyanate concanavalin A

G1 phase: gap 1 phase

G2 phase: gap 2 phase

GFP: green fluorescent protein

GLM: generalized linear model

GO: gene ontology

HACS: high affinity Ca^{2+} influx system

HC: Hierarchical clustering

HOPS: homotypic fusion and protein sorting

M phase: mitotic phase

PC: principal component

PCA: principal components analysis

PBS: phosphate buffered saline

PCC: Pearson product-moment correlation coefficient

PCR: polymerase chain reaction

PIP_2: phosphatidylinositol 4,5-bisphosphate

S. cerevisiae: *Saccharomyces cerevisiae*

S phase: synthetic phase

UTR region: untranslated region

V-ATPase: vacuolar proton-translocating ATPase

YPD: rich media contains yeast extract, polypeptone and dextrose

YPG: rich media contains yeast extract, polypeptone and glycerol

Summary

Calcium (Ca^{2+}) is one of essential elements for all eukaryotic organisms, plays key roles in diverse intracellular regulatory mechanisms. Genetic studies in the budding yeast *Saccharomyces cerevisiae* have identified key components that required for Ca^{2+}-regulatory mechanisms and the maintenance of Ca^{2+}-homeostasis. Mutants that are unable to grow in the presence of 100 mM $CaCl_2$ are called Ca^{2+}-sensitive (*cls*: calcium sensitive) mutants, exhibiting their unique morphological changes upon exposure to high-concentration of Ca^{2}. In this study, I exploited morphological phenotyping of *cls* mutants for systematic functional analysis of *CLS* genes.

In the first chapter, I quantified morphological phenotype of 62 *cls* mutants in a high-dimensional manner, and scored the degree of Ca^{2+}-dependent morphological changes of the *cls* mutant by accounting for the interaction terms between chemical (Ca^{2+}) and genetic (*cls*) effects. Ca^{2+}-*cls* interactions for morphological phenotypes were categorized into three types: negative, positive, and hyper-positive interaction in relationship to Ca^{2+}-dependent morphological changes of the wild-type. Cluster analysis based on the Ca^{2+}-*cls* interaction profiles revealed nine functional gene-units with their unique properties. Class I and II *CLS* genes were involved in maintaining Ca^{2+} homeostasis. The functional gene-units with large number of Ca^{2+}-*cls* interactions (Class I, II and IV *CLS*) have large impact on cell morphology under high concentration of Ca^{2}. Ca^{2+}-calmodulin dependent phosphatase (calcineurin) inhibitor, FK506 confers either alleviating or aggravating effects on the cell growth of the *cls* mutants under high

concentration of Ca^{2}, reflecting their different intracellular functions. Finally, correlation analysis of the interaction profiles revealed relationships between the nine functional gene-units, proposing global, and system-level view of Ca^{2+}-regulatory network in eukaryotic cell.

In the second chapter, I focused on a *cls* mutant, *cls5-1*, whose mutation is allelic to profilin-encoding-gene *PFY1* that is essential for yeast cell growth. To reveal the mechanisms of the Ca^{2+}-sensitive phenotype, I investigated the genes concomitantly responsible for the sensitivity and its interaction network. Involvement of profilin in the maintenance of intracellular Ca^{2+} homeostasis was supported by the fact that both exchangeable and non-exchangeable intracellular Ca^{2+} pools in the *cls5-1* mutant are higher than those of the wild-type strain. Several deletions of the genes whose proteins physically interact with profilin resulted in the Ca^{2+}-sensitive phenotype. Examination of the intracellular Ca^{2+} pools indicated that Bni1p, Bem1p, Rho1p, and Cla4p are also required for the maintenance of Ca^{2+} homeostasis. Quantitative morphological analysis revealed that the Ca^{2+}-*cls* interaction profiles in *cls5-1* cells are similar to *bem1Δ* and *cls4-1* cells. Common Ca^{2+}-dependent morphological changes were an increase in cell size and a decrease in the ratio of budded cells in the population. Since the mutation of *cls4-1* is allelic to *CDC24* gene, I suggest that profilin, Bem1p, and Cdc24p are required for Ca^{2+}-modulated bud formation. Thus, profilin is involved in Ca^{2+} regulation in two ways: the first is Ca^{2+} homeostasis in coordination with Bni1p, Bem1p, Rho1p, and Cla4p, and the second is the requirement in Ca^{2+}-modulated bud formation in coordination with Bem1p and Cdc24p.

General introduction

Calcium is a ubiquitous element in nature. In the process of biological evolution, calcium ion (Ca^{2+}) was selected for a cellular regulator because it satisfy several prerequisites: non-metabolic, fast kinetics, easy recognition, and it can bind to proteins of many pathways (Williams, 1999). Consequently, Ca^{2+} to date performs structural, enzymatic, and signaling roles in enormous range of eukaryotic cell types including fungal, plant, and animal which differentiated billions of years ago. At the same time as these essential roles of Ca^{2+}, high level of cytosolic free Ca^{2+} can also be harmful mainly because it precipitate organic anions readily. Thus cells must be able to acquire, utilize, and store Ca^{2+} effectively, and have orchestrated homeostatic mechanisms to keep intracellular levels of Ca^{2+} in a certain range to avoid its toxicity (Cyert and Philpott, 2013). Functional abnormalities in intracellular Ca^{2+} homeostasis in humans lead to myriad of diseases such as skeletal-muscle, skin, psychiatric, and neurodegenerative diseases (Missiaen *et al.*, 2000; Wang and Sun, 2010).

To allow intracellular Ca^{2+}-regulatory mechanisms function properly, resting cells keep the cytosolic free Ca^{2+} concentration very low despite dramatic fluctuations in the gradient across the plasma membrane (De Waard *et al.*, 1996; Berridge *et al.*, 2003). In the budding yeast *Saccharomyces cerevisiae*, one of the best eukaryotic model organism, the concentration of cytosolic free Ca^{2+} is maintained between 50 and 200 nM in the presence of environmental Ca^{2+} ranging from 1 μM to 100 mM (Halachmi and Eilam, 1993; Cui and Kaandorp, 2006; Cui *et al.*, 2009). Intracellular Ca^{2+} is known to be compartmentalized in yeast cells. Ca^{2+} pools are classified

as exchangeable or non-exchangeable based on pulse/chase experiments (Eilam, 1982). Most of the non-exchangeable pools reside in cellular compartments such as the vacuole and the endoplasmic reticulum, and the exchangeable pools are located in the cytosol (Eilam, 1982; Eilam *et al.*, 1985; Tanida *et al.*, 1996).

Genetic studies in the budding yeast have revealed molecular mechanisms of maintaining intracellular Ca^{2+} homeostasis and Ca^{2+} regulatory pathways. The yeast vacuole is the primary Ca^{2+} storage, containing more than 90 % of intracellular Ca^{2+} (Dunn *et al.*, 1994). A vacuole P-type ATPase Pmc1p plays crucial role in sequestering cytosolic Ca^{2+} into the vacuole. The *pmc1* mutation leads to reduced vacuolar Ca^{2+} content and shows Ca^{2+}-sensitive growth (Cunningham and Fink, 1994). These phenotypes are aggravated by disruption of a vacuolar H^{+}-Ca^{2+} exchanger Vcx1p, implying that Pmc1p and Vcx1p coordinate to maintaining cytosolic Ca^{2+} homeostasis. In response to an elevation of cytosolic Ca^{2+}, calcinerin, the Ca^{2+}/Calmodulin-dependent phosphatase, up-regulates transcription of *PMC1* by activation of a transcription factor Crz1p, whereas it negatively regulates Vcx1p through an unknown mechanism (Cunningham and Fink, 1996; Stathopoulos and Cyert, 1997; Pittman *et al.*, 2004).

Vacuolar proton-translocating ATPases (V-ATPases) are also important for maintaining Ca^{2+} homeostasis (Ohya *et al.*, 1991b; Umemoto *et al.*, 1991; Bachhawat *et al.*, 1993; Hirata *et al.*, 1993; Ho *et al.*, 1993). Studies have revealed in detail that the proton motive force driven by V-ATPase is required for activation of Ca^{2+} transporters in the vacuole, including Vcx1p (Cunningham and Fink, 1996; Pozos *et al.*, 1996; Forster and Kane, 2000). Mutants with inactive

V-ATPase were not able to take up Ca^{2+} to the vacuole, showing the growth defect under high concentrations of Ca^{2+} in the medium (Ohya *et al.*, 1991b). Clearly, these studies indicate that the vacuole is essential for intracellular Ca^{2+} homeostasis after exposure to high environmental Ca^{2+}. However, the vacuole also has a counteracting Ca^{2+} release channel, Yvc1p, which is dependent on cytosolic Ca^{2+} elevation for its activity (Chang *et al.*, 2010). Overexpression of Yvc1p resulted in elevation of cytosolic Ca^{2+} and Ca^{2+} sensitivity (Denis and Cyert, 2002).

Likewise, since the yeast endoplasmic reticulum (ER) contains a number of Ca^{2+}-dependent enzymes, the ER-lumenal Ca^{2+} concentration are maintained much higher than the cytosol (Demaurex and Frieden, 2003). Cls2p/Csg2p is a membrane protein localized to the ER and is involved in regulation of Ca^{2+} homeostasis in the lumen of the ER (Beeler *et al.*, 1994; Takita *et al.*, 1995; Tanida *et al.*, 1996). Another mechanism to regulate Ca^{2+} influx is high affinity Ca^{2+} influx system (HACS) in the plasma membrane, which requires at least three channel proteins, Cch1p, Ecm7p, and Mid1p (Cunningham, 2011). Maintaining Ca^{2+} homeostasis trough HACS is necessary for appropriate adaptation and survival of the cell in these conditions (Iida *et al.*, 1994; Fischer *et al.*, 1997; Martin *et al.*, 2011). Above findings indicate that many proteins in various organelles are necessary for maintaining intracellular Ca^{2+} homeostasis and Ca^{2+} regulatory pathways in yeast cells.

Genome-scale isolation of Ca^{2+}-sensitive mutants in *S. cerevisiae* have led to identify key components (Ohya *et al.*, 1986b; Sambade *et al.*, 2005; Ohnuki *et al.*, 2007; Zhao *et al.*, 2013), trying to provide further clues to mechanisms of intracellular Ca^{2+} homeostasis and Ca^{2+}

regulatory pathways. Sambade *et al.* screened several haploid yeast mutants showing growth defects at high pH and Ca^{2+} to investigate mechanism of organelle acidification which is crucial for sequestration of cytosolic free Ca^{2+} into intracellular compartment (Sambade *et al.*, 2005). Another genetic study identified set of diploid yeast mutants showing growth defect under 400 mM $CaCl_2$ condition (Zhao *et al.*, 2013). Ohya *et al.* isolated 18 complementation groups of *cls* (*cls*: calcium sensitive) mutants that were unable to grow well in the presence of 100 mM $CaCl_2$ after EMS mutagenesis (Ohya *et al.*, 1986b). Ohnuki *et al.* isolated 58 *cls* mutants from a comprehensive gene deletion set that covers all non-essential yeast genes (Ohnuki *et al.*, 2007). These previous studies indeed identified building blocks of Ca^{2+} regulatory mechanisms. However, how individual factors function in Ca^{2+}-regulatory mechanisms is not fully understood, and their functional relationships remain elucidated.

In the presence of high concentration of Ca^{2+} in the medium, the wild-type yeast cells show several responses to its cell morphology, even in the concentration that are not deleterious to its growth. In the presence of 100 mM $CaCl_2$, rounded cells with centered nuclei accumulate at G1 phase, and cells with a straightened budding site, a wide neck and large actin regions accumulate at the S/G2 phase (Ohnuki *et al.*, 2007). It should be noted that *cls* mutants exhibit unique cell morphology distinct from the wild-type under the Ca^{2+}-rich conditions (Ohnuki *et al.*, 2007; Yoshida *et al.*, 2013). For instance, the *cls4* mutant cells showed terminal phenotype of multinuclear, large, unbudded cell shape in the presence of 100 mM $CaCl_2$, having defects in bud emergence (Ohya *et al.*, 1986a). Another *cls* mutant *zds1* accumulates cells with one nucleus and

elongated bud because of G2/M arrest under high Ca^{2+} condition (Yu *et al.*, 1996; Ohnuki *et al.*, 2007). These observations implied that a part of the Ca^{2+}-responses of the wild-type are emphasized as unique cell morphologies of the *cls* mutants. Therefore systematic and statistical analysis of the unique phenotypes would provide clues to understand the specific cellular defects caused by the *cls* mutation in response to high concentration of Ca^{2+}.

Ca^{2+}-induced morphological changes are unique in each *cls* mutant (Ohnuki *et al.*, 2007; Yoshida *et al.*, 2013). To evaluate morphological phenotypes that are unique to individual *cls* mutants, I exploited the high-dimensional morphological phenotypic traits acquired from CalMorph (Ohtani *et al.*, 2004). This system is an image processing software package that make it possible to quantify 501 cell morphology parameters from fluorescence images of the cell wall, actin, and nuclear DNA of yeast cells (Ohya *et al.*, 2005). High-dimensional morphological analyses have yielded several novel findings: relationships between gene functions and morphological phenotypic traits (Ohya *et al.*, 2005), identification of genetic factors that are essential for the survival of the natural yeasts in diverse environments (Yang *et al.*, 2014), dissecting complex cellular processes (Ohnuki *et al.*, 2007; Okada *et al.*, 2010, 2014), and target identification of specific drugs (Ohnuki *et al.*, 2010, 2012; Iwaki *et al.*, 2013). Thus quantification of cellular morphology has been proven to be a powerful tool in dissecting molecular mechanisms in the cell, and in this study, I applied CalMorph to Ca^{2+} treated cells of the wild-type and *cls* mutants in order to evaluate their morphology.

Specifically in the first chapter, I generated Ca^{2+}-*cls* interaction profiles of 62 *cls* mutants as Ca^{2+}-response signatures (Fig. 1). Using the Ca^{2+}-*cls* interaction profiles, properties of Ca^{2+}-*cls* interaction were examined. I also demonstrated that the Ca^{2+}-*cls* interaction profiles can be used to group *CLS* genes, and to construct a system-level overview of Ca^{2+} homeostasis and Ca^{2+}-regulatory network in the yeast. Subsequently in the second chapter, I focused on a *cls* mutant *cls5*, whose mutation is allelic to the profilin-encoding-gene *PFY1* (Takita, 1997). The *cls5* mutant has elevated Ca^{2+} content and initial Ca^{2+} uptake (Ohya *et al.*, 1986b), and shows altered cell morphology under high Ca^{2+} condition. I identified factors that functions in Ca^{2+}-regulatory mechanisms cooperatively with profilin. Measurement of intracellular Ca^{2+} pools and analysis of Ca^{2+}-*cls* interaction profiles in these factors (Fig. 2) revealed a functional network of genes involved in intracellular Ca^{2+} homeostasis and cell morphogenesis under high Ca^{2+} condition. Above results demonstrated that my strategy for generalizing high-dimensional chemical-genetic interaction profiles can be applicable to systematic analysis of genes at different scales, from genome-wide functional characterization to focused mechanistic investigations.

Figures

Fig. 1

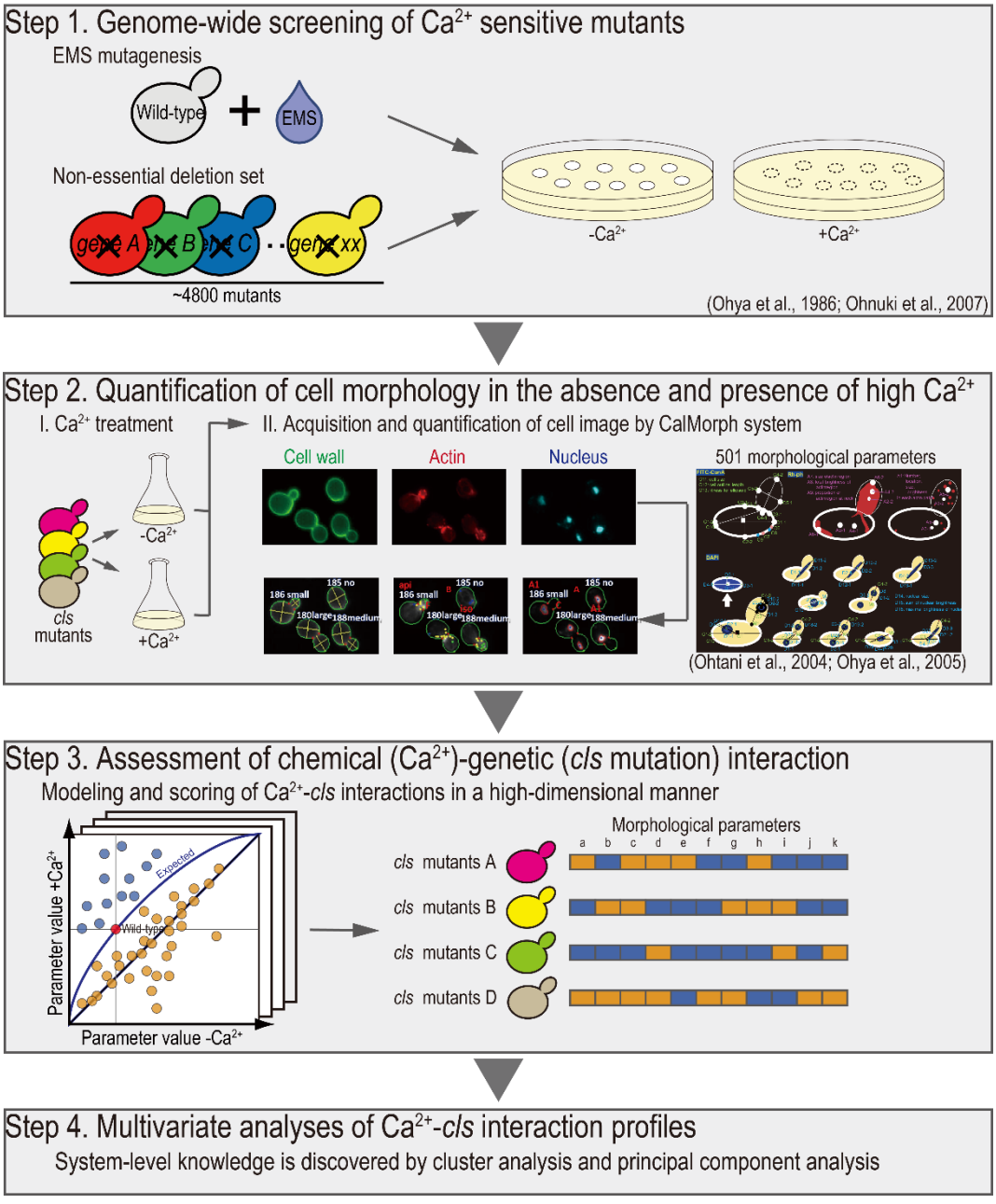

Figure 1. Description of experiments and analysis conducted in Chapter I.

Fig. 2

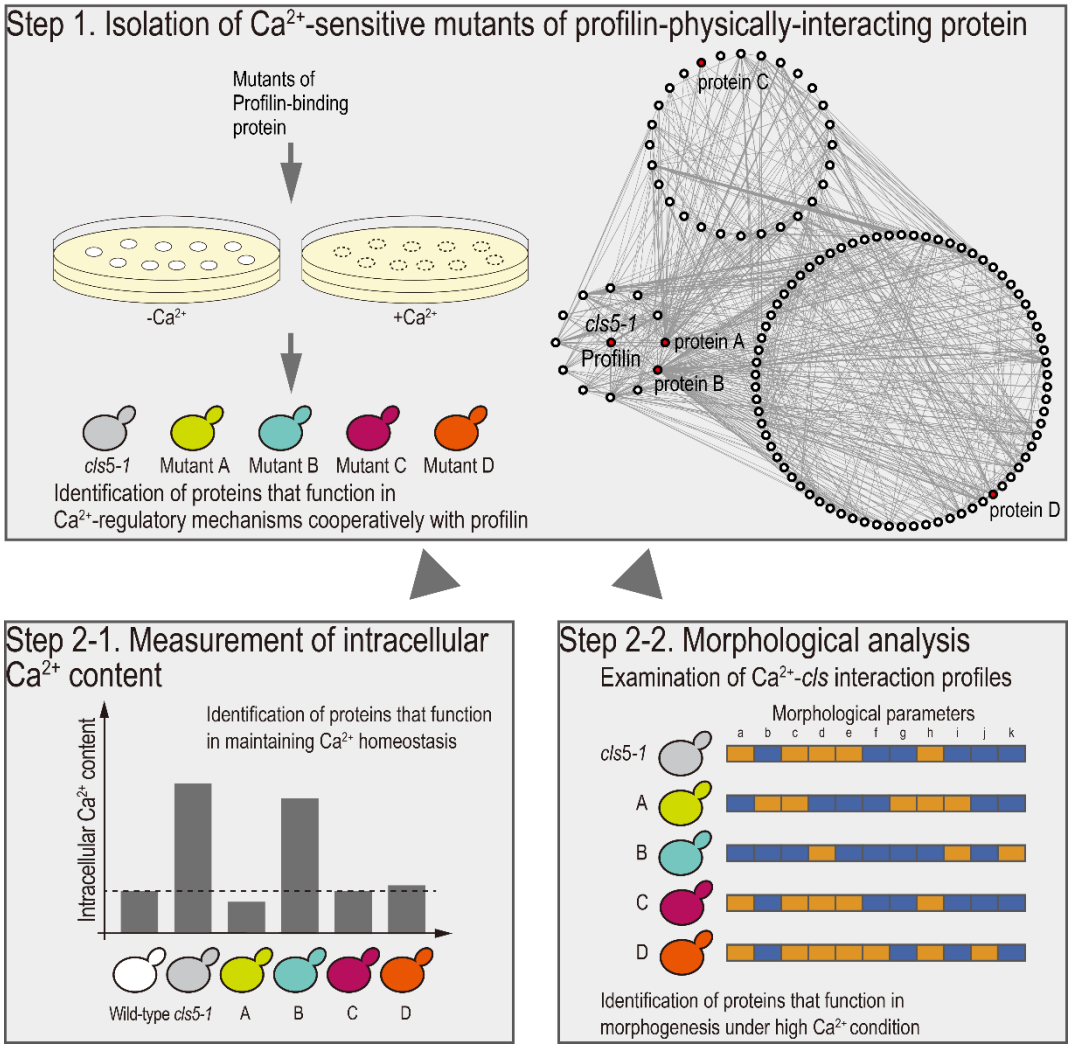

Figure 2. Description of experiments and analysis conducted in Chapter II.

Chapter I

High-dimensional chemical-genetic interaction profiles reveal a global view of Ca^{2+} homeostasis and Ca^{2+}-regulatory pathways in yeast

Introduction

Ohya *et al.* (1986) isolated 18 complementation groups of *cls* (*cls*: calcium sensitive) mutants after EMS mutagenesis (Ohya *et al.*, 1986b). Ohnuki *et al.* screened a comprehensive gene deletion set that covers all non-essential yeast genes and identified 58 *cls* mutants (Ohnuki *et al.*, 2007). However, how individual *CLS* genes involves in Ca^{2+} homeostasis and Ca^{2+} regulatory pathways is not fully understood, and their functional relationships among them also are not elucidated. Hence seeing the system-level whole picture of cellular Ca^{2+}-regulatory mechanisms remains challenging.

As mentioned in the General introduction, the wild-type yeast cells show several responses to its cell morphology under high Ca^{2+} condition, even in the concentration that are not deleterious to its growth (Ohnuki *et al.*, 2007). More importantly, *cls* mutants exhibit unique cell morphology distinct from the wild-type under the Ca^{2+}-rich conditions (Ohnuki *et al.*, 2007; Yoshida *et al.*, 2013), implying that a part of the Ca^{2+}-responses of the wild-type are emphasized as unique cell morphologies of the *cls* mutants. Therefore systematic and statistical analysis of the unique phenotypes must be informative for functional characterization of the *CLS* genes.

In this chapter, I computed Ca^{2+}-*cls* gene interaction scores by using the high-

dimensional morphological phenotypic traits. Specifically, with image processing software CalMorph (Ohtani *et al.*, 2004; Ohya *et al.*, 2005), I quantified cell morphology of 62 *cls* mutants in the presence or absence of 100 mM $CaCl_2$, and applied generalized linear model to the morphological data so as to calculate interaction scores between chemical (Ca^{2+}) and mutational (*cls*) effects. My multivariate analyses revealed properties of Ca^{2+}-*cls* interaction, functional gene-units of the *CLS* genes and a global view of Ca^{2+} homeostasis and Ca^{2+} regulatory network in the eukaryotic cell.

Results

Three types of Ca^{2+}-*cls* interaction by using morphological phenotypes

In order to identify morphological features in which combinational effects of Ca^{2+} and *cls* mutations were observed, I applied generalized linear model to high-dimensional morphological data of wild-type and the *cls* mutants incubated in YPD and 100 mM $CaCl_2$ medium. I found that at least one significant Ca^{2+}-*cls* interaction was detected in the 209 morphological parameters ($P < 0.05$, likelihood ratio test). To extract independent morphological features in 209 morphological parameters, I applied a principal component analysis (PCA) as described previously (Ohnuki *et al.*, 2012). PCA is an exploratory multivariate statistical technique for identifying independent morphological features. The 209 parameters were explained by 19 independent principal components at a cumulative contribution ratio (CCR) > 0.70. Parameters significantly correlated with each principal component (PC) were listed in Fig.

S1 ($P < 0.01$, *t* test). Ca^{2+}-*cls* interactions were detected in many kinds of morphological features such as mother and bud cell size, nuclear position and motility, actin localization, and also detected in several phenotypic noises. These results implied that Ca^{2+}-*cls* interactions of the 62 *cls* mutants were observed in various cellular aspects and at the different phases of the cell cycle.

I next scored degree of Ca^{2+}-dependent morphological changes by only accounting for interaction terms between Ca^{2+} and *cls* mutational effects (namely π score). The π scores were given by the difference between the typical Ca^{2+}-induced morphological change expected from the wild-type and the measured Ca^{2+}-induced morphological change of the *cls* mutant. Three examples (*cls4-1*, *rib4* and *vma1*) of the Ca^{2+}-*cls* interactions were illustrated in Fig. 3. First example is the "negative" interaction observed in *cls4-1*. At S/G2 phase, actin region in the bud of the wild-type cells increased in the presence of 100 mM $CaCl_2$ (Fig. 3 A, B). In this parameter, the Ca^{2+}-induced morphological change of *cls4-1* was in the same direction to the wild-type, and higher than the change of the wild-type (Fig. 3 B, C, Fig. 4 A). The negative interaction can be interpreted as a sensitized Ca^{2+}-response by the *cls* mutation. It is regarded as an analog of negative genetic interaction for fitness as previously described (Dixon *et al.*, 2009).

Second example is the "positive" interaction observed in *rib4.* In *cls* mutants like *rib4* whose parameter values were hardly changed whereas that of the wild-type increased in the presence of 100 mM $CaCl_2$ (Fig. 3 B, C). Since this type of Ca^{2+}-*cls* interaction described the *cls* mutant exhibiting less Ca^{2+}-induced morphological change than that expected from the wild-type, it can be interpreted as suppression or masking of normal Ca^{2+}-response by the *cls* mutation (Fig.

4 A). This is regarded as an analog of positive genetic interaction for fitness as previously described (Dixon *et al.*, 2009).

The last example is the "hyper-positive" interaction observed in *vma1*. In the *cls* mutants like *vma1* whose parameter values were changed in the opposite direction to the wild-type (lower than the diagonal line in Fig. 3 C), and lower than that of the wild-type in the presence of 100 mM $CaCl_2$ (lower than horizontal black line in Fig. 3 C). This type of interaction is characteristic of phenotypic data that change bidirectionally, like cell morphology, but not characteristic of those that change unidirectionally like fitness of loss of function mutants and endogenous sensor (Dixon *et al.*, 2009; Jonikas *et al.*, 2009). Thus, I systematically identified three types of Ca^{2+}-*cls* interactions in each of the 62 mutants for further analysis.

Characterization of the Ca^{2+}-*cls* interactions

In order to understand the physiological implication of Ca^{2+}-*cls* interaction, I investigated the features of the interaction. First, I observed that larger number of positive Ca^{2+}-*cls* interactions was detected than that of negative ones (Fig. S2 A). In 51 of the 62 *cls* mutants (83 %), number of positive Ca^{2+}-*cls* interactions was higher than that of negative ones. Among the 62 *cls* mutants, 77% of detected Ca^{2+}-*cls* interactions were positive ones (1630 out of 2112 C^{2+}-*cls* interactions). Second, the number of Ca^{2+}-*cls* interactions was not correlate with that of Ca^{2+}-induced morphological changes (Ohnuki *et al.*, 2007) in *cls* mutants (Fig S2 B). A correlation coefficient between the number of Ca^{2+}-*cls* interactions and that of significantly changed parameters was 0.27 ($P < 0.05$, *t* test), suggesting that Ca^{2+}-*cls* interactions had different

characteristics from Ca^{2+}-induced morphological changes. Third, although the number of Ca^{2+}-*cls* interaction in each of *cls* mutants were widely distributed, about 80 % of *cls* mutants exhibited under 60 Ca^{2+}-*cls* interactions (Fig. S2 C), showing that a small proportion of *cls* mutants had large number of the Ca^{2+}-*cls* interaction. I thus reason that *CLS* genes with large number of the Ca^{2+}-*cls* interaction may serve as the hubs that play key role for cell proliferation under high Ca^{2+} condition. Finally, the *cls* mutants with large number of the Ca^{2+}-*cls* interaction tended to show more severe growth defects than others in the presence of 100 mM $CaCl_2$ (Fig. S2 D). Therefore, I concluded that Ca^{2+}-*cls* interaction data provided the unique source for functional interaction between Ca^{2+} and the *cls* mutation.

Clustering analysis of high-dimensional Ca^{2+}-*cls* interaction profiles

In order to explore whether Ca^{2+}-*cls* interaction profiles can be used for grouping *CLS* genes, I applied a cluster analysis to the 62 Ca^{2+}-*cls* interaction profiles (Fig. 5). Using multiscale bootstrap technique (Suzuki and Shimodaira, 2006), nine classes for a total 49 *cls* mutants (79 %) were identified at AU *P* value > 0.95 (Fig. 5). Interestingly, cellular function of several classes can be annotated by gene ontology (GO) (Table 1). For instance, class I consisted of 17 *vma* mutants defective in V-ATPase localized in acidic compartments (Ohya *et al.*, 1991a; Kane, 2006). Class II contained many mutants of core subunits in HOPS and CORVET complexes involved in membrane fusion at endosomes, vacuole, and lysosomes (Balderhaar and Ungermann, 2013). Class IV consisted of *cls4-1* and *bem1* both of which were involved in Ca^{2+}-modulated bud formation (Yoshida *et al.*, 2013). Class VIII included *fet3* and *ftr1* both of which were iron ion

transporter (Kwok *et al.*, 2006). These results suggested that *cls* mutants with similar Ca^{2+}-*cls* interaction profiles tended to have defects in the similar functional gene-units with their unique properties. It is also noted that intracellular Ca^{2+} contents of the *cls* mutants in class I except for *vma22* were 0.6 fold lower than that of the wild-type whereas those of the *cls* mutants in class II were all 3.1-fold higher than that of the wild-type cell (Table 1), suggesting that these two classes function in opposite ways during maintaining intracellular Ca^{2+} homeostasis.

Characterization of Ca^{2+}-*cls* interaction in each functional gene units

In order to know whether different class mutants have distinct Ca^{2+}-*cls* interaction properties, I investigated the number of the Ca^{2+}-*cls* interaction in each class (Fig. 6 A). I found that the number of the Ca^{2+}-*cls* interaction biased in each of classes. Particularly, *cls* mutants of class I (V-ATPase), II (C-VPS), IV (Ca^{2+}-modulated bud formation) showed on average 7.4, 6.3, and 7.5 times more interactions than that of class VIII (Fe ion transporter) (Table 1). This suggested that the genes responsible for class I, II, and IV *cls* mutations may function as important hubs under high Ca^{2+} conditions. I also found that some classes of *cls* mutants showed bias in interaction type. Class III and IV *cls* mutants showed a high proportion of negative Ca^{2+}-*cls* interaction (Fig. 6 B). The proportion of negative Ca^{2+}-*cls* interactions in class III and IV *cls* mutants were on average 3.2 and 4.1 times higher than that in class I *cls* mutants. Class IV *cls* mutants sheared 14 negative Ca^{2+}-*cls* interactions which were observed at all phases of the cell cycle (Fig. S3 B), suggesting that class IV *cls* mutation sensitize Ca^{2+}-responses of the wild-type through the cell cycle. Meanwhile, class III *cls* mutants tended to show negative Ca^{2+}-*cls*

interactions at G1 and S/G2 phase of the cell cycle (Fig. S3 A), suggesting that class III *cls* mutation sensitize the Ca^{2+}-response mainly at G1 and S/G2 phase. These results implied that the negative Ca^{2+}-*cls* interactions in class III and IV contained rich functional information.

The effects of calcineurin were reflected in Ca^{2+}-*cls* interaction profiles

A major target of intracellular Ca^{2+} is calmodulin, a ubiquitous Ca^{2+}-binding protein in eukaryotic cells. The Ca^{2+}/calmodulin signaling pathway therefore plays important roles in the response to high concentration of Ca^{2+}. It has been known that Ca^{2+}/calmodulin binds to activate calcineurin, and subsequently calcineurin elicits several cellular responses (Cyert, 2001, 2003). The calcineurin activity is inhibited by the immunosuppressant drug FK506 (Heitman *et al.*, 1991), and previous genetic studies showed that inactivation of calcineurin by FK506 confers either alleviating or aggravating effects on the cell growth of the *cls* mutants: FK506 suppressed Ca^{2+}-sensitive growth of *pmc1*, while it enhanced that of *vma* mutants (Cunningham and Fink, 1994; Tanida *et al.*, 1995). Here I investigated the FK506 effects on the 62 *cls* mutants under condition of high Ca^{2+}, and found that the Ca^{2+}-sensitive phenotype of 13 *cls* mutants (21 %) were suppressed and that of 40 *cls* mutants (65 %) were enhanced (Fig. 7 A, Fig. S4, Table, S1). Interestingly, *cls* mutants that failed to maintain intracellular Ca^{2+} homeostasis tended to show FK506-enhanced Ca^{2+} sensitivity (Fig. S5), being coincident with the fact that the calcineurin regulates intracellular Ca^{2+} homeostasis (Tanida *et al.*, 1995; Cunningham and Fink, 1996). I also found that each class mutant has common response to FK506. Class I, II and III *cls* mutants showed FK506-enhanced Ca^{2+} sensitivity, while class IV, VI and VIII mutants showed FK506-

suppressed Ca^{2+} sensitivity (Table 1), suggesting that the FK506 effects were similar in each class.

I further investigated the interaction profiles of FK506-suppressed and enhanced *cls* mutants after performing principal component analysis. I found that the interaction profiles of these *cls* mutants were distinguishable on two-dimensional Ca^{2+}-*cls* interaction space, particularly in the first principal component (PC1) and the second principal component (PC2) (Fig. 7 B, Fig. S6). The interaction of the class I and II showed increased PC1 scores and those of class III showed decreased PC2 scores (Fig. 7 B). Subsequently, five and three representative features accompanied with the PC1 and PC2 were identified, respectively (Fig. S7 A). Figure S7 B to E illustrates representative Ca^{2+}-*cls* interactions reflecting the effects of FK506 on class I, II, and III *cls* mutants. In these parameters, class I, II, and III *cls* mutants tended to show hyper-positive interactions whose parameter values were changed in the opposite direction with the wild-type. For example, in S/G2 phase, ratio of class I *cls* mutant cells with apical and isotropic growth were decreased in the presence of 100 mM $CaCl_2$ whereas that of the wild-type cells were increased (Fig. S7 C, D), suggesting that effects of FK506 were reflected in localization of actin to nascent bud in S/G2 phase. Correspondingly, ratio of class I *cls* mutant cells with large bud were decreased in the presence of 100 mM $CaCl_2$ in S/G2 phase (Fig. S7 E). These results implied a mechanism that calcineurin regulates actin localization in G2/S phase, which were required for budding (Shitamukai *et al.*, 2004), to resist high environmental Ca^{2+} under circumstances where class I, II, and III *CLS* functions are declined.

Global view of Ca^{2+} homeostasis and Ca^{2+} regulatory pathways

Whole cellular response to high concentration of extracellular Ca^{2+} must be orchestrated by several Ca^{2+}-regulatory mechanisms (Cyert and Philpott, 2013). To overview the relationship of the cellular functions involved in Ca^{2+} homeostasis and Ca^{2+} regulatory pathways, I constructed a network of the *CLS* genes based on the correlation between the Ca^{2+}-*cls* interaction profiles (Fig. 8). This network provides system-level understandings of Ca^{2+}-regulatory mechanisms localized in several organelle. Functions of class I (V-ATPase) and II (C-VPS), which were localized to vacuole membrane and endosome involved in the maintenance of Ca^{2+} homeostasis, were expected to play central roles under high Ca^{2+} condition as shown as large nodes. As presented with many blue lines, Ca^{2+}-*cls* interaction profiles of class I and II *cls* mutants tended to correlate negatively with those of other *cls* mutants (Fig. S8), illustrating that class I and II *CLS* gene functions are different from others in the network. Since FK506 enhanced Ca^{2+} sensitivity of these *cls* mutants, calcineurin may up-regulate compensatory mechanisms of class I and II *CLS* gene functions to buffer deleterious effects of high environmental Ca^{2+}. In contrast, Ca^{2+}-*cls* interaction profiles of class IV to IX *cls* mutants tended to correlated positively with each other (Fig. S8), suggesting that these classes may share common functional role for the global Ca^{2+}-regulatory network. FK506 suppressed Ca^{2+} sensitivity of class IV, VI, and VIII *cls* mutants. Thus calcineurin-mediated regulation of class IV (Ca^{2+}-modulated bud formation), VI (riboflavin biosynthesis) and VIII (Fe ion transporter) *CLS* gene functions may be opposite to that of class I and II *CLS* gene functions, showing that common calcuneurin-mediated regulation might contribute to positive correlation between Ca^{2+}-*cls* interaction profiles of class IV, IV, and VIII *cls*

mutants. This also suggested that calcineurin down-regulate compensatory mechanisms of class VI, IV, and VIII *CLS* gene functions under high Ca^{2+} condition.

Discussion

I quantified high-dimensional chemical-genetic interaction profiles for the first time using morphological phenotypic traits, and analyzed a Ca^{2+} responsive morphological signature in each Ca^{2+}-sensitive mutant. Since morphological phenotypes change bidirectionally, I first identified "hyper-positive" interaction in which the direction of the interaction is opposite to the wild-type response. My multivariate analyses revealed a series of processes involved in the maintenance of Ca^{2+} homeostasis and Ca^{2+} regulatory pathways. These processes included a wide range of cellular activities such as vacuolar acidification, vacuolar morphogenesis, Ca^{2+}-modulated bud formation, riboflavin biogenesis, protein sorting, and Fe ion transporter, as well as unknown functional processes localized in the cytoplasm, the nucleus or the endoplasmic reticulum. The analyses of the Ca^{2+}-response signatures also enable us to construct a system-level global view of Ca^{2+} homeostasis and Ca^{2+} regulatory pathways in the yeast cell. Since the yeast deletion mutants of all non-essential genes were used to screen Ca^{2+}-sensitive mutants, my network covers genome-wide gene functions essential for cell proliferation under high Ca^{2+} condition. Thus this study serves a blueprint for system-level understanding of Ca^{2+}-homeostasis and Ca^{2+}-regulatory pathways.

Positive and negative Ca^{2+}-*cls* interactions for morphological phenotypes

A term “genetic interaction” refers to a phenotype caused by combining the effects of individual genetic variants (Dixon *et al.*, 2009). Generally, based on the difference between the observed and expected double-mutant phenotype, genetic interactions can be classified into two groups, one is positive interaction and the other is negative interaction (Dixon *et al.*, 2009). The negative genetic interactions describe double mutant whose phenotype is stronger than expected. Most extreme case of negative interaction for fitness is synthetic lethality, in which the combination of two mutations results in an inviable phenotype (Mani *et al.*, 2008; Baryshnikova *et al.*, 2013). In analogy with genetic interaction, chemical-genetic interaction refers to a phenotype caused by combining the effects of chemicals and genetic variants. Chemical synthetic lethality is the negative interaction in which a chemical compound confers lethal effects to the mutants. Ca^{2+}-sensitive mutants exhibit lethality (or sickness) in high concentration of Ca^{2+}, thus showing negative interaction. The negative Ca^{2+}-*cls* interactions for morphological phenotypes identified in this study are equivalent to the negative interaction for fitness. Since negative Ca^{2+}-*cls* interaction for morphological phenotype describe *cls* mutant exhibiting a stronger Ca^{2+}-induced morphological change than expected in the same direction with the wild-type, this phenotype can be interpreted as sensitized Ca^{2+}-response by the *cls* mutation.

I observed two types of positive Ca^{2+}-*cls* interactions in morphological phenotyping. One describes *cls* mutants exhibiting less Ca^{2+}-induced morphological change than expected from that of the wild-type. This can be interpreted as situation where Ca^{2+}-response of the wild-type was suppressed (or masked) by the *cls* mutation, equivalent to positive interaction for fitness. The

other type (termed "hyper-positive interaction") describes *cls* mutants exhibiting Ca^{2+}-induced morphological change in the opposite direction to the wild-type. This type is unique in morphological phenotype-based interaction because morphological phenotype can change bidirectionally. I observed that hyper-positive Ca^{2+}-*cls* interactions tended to be observed in *cls* mutants showing FK506-enhanced Ca^{2+} sensitivity, particularly in class I and II *cls* mutants. Since calcineurin-mediated regulation for cell proliferation is enhanced under high Ca^{2+} condition, I think that a fraction of positive Ca^{2+}-*cls* interaction for morphological phenotypes may reflect "gain-of-function" effect.

CLS genes showing similar Ca^{2+}-_cls_ interaction pattern share intracellular function

Quantitative genetic interaction profiles have been used to group genes based on intracellular functions, proposing that the genes belonging to the same pathway or biological process tend to share similar genetic interaction profile (Tong *et al.*, 2004; Schuldiner *et al.*, 2005; Pan *et al.*, 2006; Jonikas *et al.*, 2009; Costanzo *et al.*, 2010). In this study, I performed hierarchical clustering based on the Ca^{2+}-*cls* interaction scores, and identified nine robust functional gene-units functioning in Ca^{2+} homeostasis and Ca^{2+} regulatory pathways. This result indicates that the *CLS* genes sharing the same cellular function tend to show similar pattern of Ca^{2+}-*cls* interactions for morphological phenotype, each of which represents altered response to high environmental Ca^{2+} by the *cls* mutation.

Previously, Ohnuki *et al*. (2007) performed a cluster analysis of 59 *CLS* genes based on the similarity of Ca^{2+}-induced morphological change. Fifty-one percent of the *cls* mutants were

classified into seven groups, and three groups were functionally annotated. The present study was successful in classifying the 79% mutants into nine groups, and six classes were annotated functionally. These results indicated that the cluster analysis performed in this study had higher resolution than the previous one. Ca^{2+}-*cls* interaction profiles were used in this study, improving the resolution of clustering analysis. For estimation of Ca^{2+}-induced morphological changes, Ohnuki *et al.* (2007) calculated rank-order based *U* statistic obtained from replicated experiments in the absence or presence of high concentration of Ca^{2+}. Then, the modified *U* statistic that reflect the direction of the morphological changes was applied to the cluster analysis (Ohnuki *et al.*, 2007). Since the wild-type yeast cells showed several responses in cell morphology in the presence of high concentration Ca^{2+} in the medium (Ohnuki *et al.*, 2007), Ca^{2+}-induced morphological changes of *cls* mutant includes both "altered Ca^{2+}-response by *cls* mutation" and "normal Ca^{2+}-response of the wild-type". In contrast, the GLM-based method in this study enabled to extract the interaction terms representing "altered Ca^{2+}-response of *cls* mutant" by calculating deviation of actual parameter value from the expected value which was assumed to be no interaction between high concentration of Ca^{2+} and the *cls* mutation.

Identified clusters can be used to predict the function of the uncharacterized *CLS* genes. One of the examples was class VI, to which three Ca^{2+}-sensitive mutants *rib4*, *gly1*, and *yel045c* belonged. Rib4p are required for riboflavin biosynthesis which is a precursor of flavin adenine dinucleotide (FAD) (Oltmanns and Bacher, 1972), Gly1p is a glycine biosynthetic enzyme threonine aldolase (McNeil *et al.*, 1994), and the *YEL045C* is dubious open reading frame

opposite to the *GLY1* gene. In a filamentous fungus *Ashbya gossypii* closely related to yeast, production of riboflavin were improved by over expression of the *GLY1* gene (Monschau *et al.*, 1998), suggesting that Gly1p are involved in the riboflavin biosynthesis. Although molecular mechanism remains to be elucidated, intracellular Ca^{2+} may regulate production of FAD which is required for several reactions in metabolism. Since Ca^{2+} sensitivity of the three *cls* mutants were suppressed by FK506, compensatory mechanism for this pathway may be down-regulated by calcineurin. Thus the pathway are essential under high Ca^{2+} condition. Another example is class II *cls* mutants where *cls5-1* was classified accompanied with *vps18, vps33, vps11,* and *vps16*, all of which are known to be core subunit of both CORVET complex and HOPS complex which functions in endosome-endosome fusion and homotypic vacuole fusion (Balderhaar and Ungermann, 2013). Several lines of evidence suggested common function of these five proteins. First, intracellular Ca^{2+} content and initial Ca^{2+} uptake of the five mutants were higher than those of wild-type cells (Ohya *et al.*, 1986b), suggesting that these five proteins were involved in maintaining intracellular Ca^{2+} homeostasis. An immunoprecipitation experiment showed that Cls5p (Pfy1p) localized with Vps16p and Vps33p at vacuole membrane (Xu and Wickner, 2006). The 4 *vps* mutants were originally isolated as class I *vam* (vacuolar morphology) whose vacuole were tiny or disappeared (Wada *et al.*, 1992) whereas vacuoles in *cls5-1* were fragmented in the presence of high environmental Ca^{2+} (data not shown). I therefore proposed the possibility that these vacuolar-membrane-localized five proteins are all involved in vacuolar biogenesis but Cls5p may function in different step from other 4 VPS proteins.

Number of Ca^{2+}-*cls* interactions

Studies of several model organisms have proposed that the majority of genes have few genetic interactions, whereas a small number of the genes are highly connected and serve as network hubs (Dixon *et al.*, 2009). In my work, a small number of *CLS* genes exhibited large number of Ca^{2+}-*cls* interactions. Moreover, number of Ca^{2+}-*cls* interactions in each of *cls* mutants were strongly biased according to the nine functional classes. Particularly, class I (V-ATPase), II (C-VPS), and IV (Ca^{2+}-modulated bud formation) exhibited large number of Ca^{2+}-*cls* interactions. Since *cls* mutation exhibiting large number of Ca^{2+}-*cls* interactions have a large impact on cell morphology in the presence of high concentration of Ca^{2+}, *CLS* genes with large number of Ca^{2+}-*cls* interactions may be more important for the integrity of overall cellular response to high environmental Ca^{2+} than others. I therefore think that number of Ca^{2+}-*cls* interactions in each of Ca^{2+}-sensitive mutants may be correlates with degree of contribution to overall Ca^{2+}-response. To support of the idea, *cls* mutants with high number of Ca^{2+}-*cls* interaction tended to show severe Ca^{2+}-sensitive phenotypes.

Positive or negative regulation of calcineurin on the functional units of Ca^{2+} homeostasis and Ca^{2+} regulatory pathways

The immunosuppressant drug FK506 forms inactive complex with calcineurin, resulting in decreased calcineurin activity (Cunningham and Fink, 1994). I examined how calucineurin is involved in cellular responses to high concentration of Ca^{2+} by testing Ca^{2+} sensitivity of a series of *cls* mutants in the presence of FK506. My results suggested that calcineurin functioned either

positively or negatively with the functional gene-units. FK506 enhanced Ca^{2+} sensitivity of all class I *cls* (*vma*) mutants lacking vacuolar membrane H^+-ATPase. Cytosolic Ca^{2+} concentration of several *vma* mutants was higher, while Ca^{2+} uptake into vacuole of these mutants was lower than those of the wild-type cell, indicating that the activity of Ca^{2+} transport into vacuole in class I *cls* mutants decreased (Ohya *et al.*, 1991b; Tanida *et al.*, 1995). Yeast cells have another compensatory mechanism of Ca^{2+} transport into vacuole such as Ca^{2+}-ATPase Pmc1p (Cunningham and Fink, 1994), and the calcineurin positively regulates Pmc1p through activation of a transcription factor Crz1p (Stathopoulos and Cyert, 1997). Because the positive feedback via calineurin is inhibited in the presence of FK506, Ca^{2+} sequestration into vacuole may decrease in class I *cls* mutants. It is of interest to note that *vma3* mutant cells have decreased cytosolic Ca^{2+} and increased organellar-stored Ca^{2+} after treatment with FK506 (Tanida *et al.*, 1995). These findings implied another regulatory mechanism in which the calcineurin negatively regulates Ca^{2+} sequestration into other organelle such as the endoplasmic reticulum and the Golgi complex (Cunningham, 2011) under high Ca^{2+} condition. In agreement with this, previous studies reported that the calcineurin might regulate Ca^{2+} sequestration into the ER in cooperative manner with Cls2p, which is localized in the ER membrane (Beeler *et al.*, 1994; Takita *et al.*, 1995; Tanida *et al.*, 1996). Since FK506 has little effect on Ca^{2+} sensitivities of most of class V *cls* mutants including *cls2*, Class V *CLS* genes may function downstream of the calcineurin. Correspondingly, Ca^{2+}-*cls* interaction profiles of class I *cls* (V-ATPase) mutants negatively correlated with that of class V *cls* (localized to the ER) mutants, suggesting that opposite regulations of Ca^{2+} homeostasis

by the calcineurin are reflected in their Ca^{2+}-*cls* interaction profiles.

My results also suggested that the calcineurin negatively regulates bud formation under high Ca^{2+} condition. Ca^{2+} sensitivities of class IV (Ca^{2+}-modulated bud formation) *cls* mutants were suppressed by FK506. Ca^{2+}-*cls* interaction profiles of class IV *cls* tended to correlate negatively with that of class I *cls* (V-ATPase) mutants, suggesting opposite direction of their regulations. Since elevated cytosolic Ca^{2+} have harmful effects on several cellular physiology (Missiaen *et al.*, 2000), one of the interesting idea is that the calcineurin may function as a check point which senses cytosolic Ca^{2+}, and if cytosolic Ca^{2+} are elevated, the calcineurin up-regulates Ca^{2+} sequestration to the vacuole, as well as down-regulates bud formation to avoid toxic effects of Ca^{2+} until cytosolic Ca^{2+} homeostasis are maintained.

Perspectives

In eukaryotic model organism *S. cerevisiae*, deletion set of non-essential genes (Winzeler *et al.*, 1999) and recent developed libraries of essential genes harboring conditional and hypomorphic alleles (Mnaimneh *et al.*, 2004; Ben-Aroya *et al.*, 2008; Li *et al.*, 2011; Jin *et al.*, 2012) have enable rapid and comprehensive identification of factors which function in cellular processes of interest. However, functional characterization of these genes, which generally requires specific gene-by-gene follow-up investigations, remains to be a bottleneck. My chemical-genetic interaction approach allow systematic characterization and the functional interrelationship of individual factors, which provides molecular bases for the focused mechanistic studies. In general, interaction studies based on high-dimensional morphological

phenotyping described here may provide crucial relationship among the multiple inputs (e.g. gene perturbation, chemical perturbation, environmental stress, and etc.). Therefore, my strategy can be applicable to wide range of studies such as determining mode-of-action of novel drugs, understanding mechanical bases of drug synergy, genetic interactions, as well as cellular response to various environmental stresses in future.

Tables

Table 1. Summary of phenotypes of nine gene-units.

Class[a]	I	II	III	IV	V	VI	VII	VIII	IX
Mutant[b]	*vma1*, *vma2*, *vma3*, *vma4*, *vma5*, *vma6*, *vma7*, *vma8*, *vma10*, *vma11*, *vma12*, *vma16*, *vma22*, *ypr099c*, *ykl118w*, *cwh36*, *yor331c* (17)	*cls5-1*, *vps11*, *vps16*, *vps18*, *vps33* (5)	*afg3*, *pkr1*, *tef4*, *vma13*, (4)	*bem1*, *cls4-1* (2)	*cls2*, *pdr13*, *psl10*, *swi3*, *trk1*, *zuo1*, *whi3* (7)	*gly1*, *rib4*, *yel045c* (3)	*bud32*, *och1*, *rpl22a*, *vps15*, *vps34* (5)	*fet3*, *ftr1* (2)	*sac1*, *ubp3*, *vps45*, *zds1*, (4)
Gene ontology[c]	V-ATPase	(C-Vps)		bud formation		(riboflavin biosynthesis)	(protein sorting)	Fe ion transporter	
Relative Ca^{2+} content (-fold)[d]	< 0.62*	3.1 >	0.5–2.8	1.1–3.1	1.0–3.3	0.9–2.0	0.4–11	1.0–1.2	0.8–2.8
Quinacrine staining[e]	No	m.d.			Yes	Yes		Yes	
Pet phenotype[f]	-	-		-				-	
$+Ca^{2+}$ +FK506[g]	Syn.	Syn.	Syn.	Sup.	Unaltered*	Sup.	Syn.*	Sup.	
Number of Ca^{2+}-*cls* interactions[h]	Many (59)	Many (50)	Medium (38)	Many (61)	Few (16)	Medium (24)	Medium (22)	Few (8)	Medium (22)
Proportion of negative Ca^{2+}-*cls* interaction			Many negative	Many negative	(Many negative)				

[a]Mutants were classified as described in the legend of Fig. 5.
[b]Values in parentheses indicate number of *cls* mutants in each class.
[c]Reference; *Saccharomyces* Genome Database (http://www.yeastgenome.org/). Enriched GOs are shown in parentheses.
[d]Compared to the wild-type cells. Data were obtained from Ohnuki *et al.*, (2007) and Yoshida *et al.*, (2013). Asterisk indicates the range of relative Ca^{2+} content with the exception of *vma22*.
[e]Yes, vacuole was stained with quinacrine; No, vacuole was not stained with quinacrine; m.d., morphological defect in vacuole. Data were obtained from Ohnuki *et al.*, (2007)
[f]Data were obtained from Ohnuki *et al.*, (2007).
[g]Sup. and Syn., Ca^{2+} sensitivity of *cls* mutant were alleviated and aggravated by the addition of 0.4 μg/ml FK506; Unaltered, Ca^{2+} sensitivity of *cls* mutant were not altered by the addition of 0.4 μg/ml FK506. Asterisks indicate unaltered Ca^{2+} sensitivity and FK505-enhanced Ca^{2+} sensitivity with the exception of *swi3* and *rpl22a*, respectively.
[h]Average number of significant Ca^{2+}-*cls* interactions within each class ($P < 0.05$, Wald test). Values in parentheses indicate average number of Ca^{2+}-*cls* interactions in each class.

Table S1. Summary of phenotypes of *cls* mutants.

No.	Mutant	Growth Type[a]	Divalent cation sensitivity				Pet phenotype	Quinacrine[b]	Relative Ca^{2+} content (-fold)[c]	$+Ca^{2+}$ +FK506[d]	Class[e]
1	*afg3*	C	Ca				-	Yes	1.330	Syn.	III
2	*bem1*	C	Ca				-	m.d.	3.125	Sup.	IV
3	*bud25*	B	Ca				-	Yes	2.623	Syn.	
4	*bud32*	B	Ca				-	Yes	0.394	Syn.	VII
5	*cls2*	A	Ca				+	Yes	1.104	Unaltered	V
6	*cls4-1*	A	Ca				+		1.071	Sup.	IV
7	*cls5-1*	B	Ca				+	m.d	5.378	Syn.	II
8	*ctr1*	A	Ca				-	Yes	0.436	Unaltered	
9	*cwh36*	B	Ca				-	No	0.435	Syn.	I
10	*fet3*	A	Ca				-	Yes	1.104	Sup.	VIII
11	*ftr1*	A	Ca				-	Yes	0.972	Sup.	VIII
12	*gly1*	B	Ca				+	Yes	1.104	Sup.	VI
13	*gon7*	B	Ca				+	Yes	0.342	Syn.	
14	*not5*	B	Ca				-	No	1.915	Sup.	
15	*och1*	B	Ca				-	Yes	10.377	Syn.	VII
16	*pdr13*	C	Ca				+	Yes	1.425	Unaltered	V
17	*pho85*	A	Ca		Mn		-	Yes	2.632	Syn.	
18	*pkr1*	C	Ca		Mn		+	No	0.577	Syn.	III
19	*psl10*	C	Ca			Mg	+	Yes	3.094	Unaltered	V
20	*pmc1*	C	Ca				+	Yes	0.182	Sup.	
21	*pro1*	B	Ca				+	No	1.142	Sup.	
22	*rcs1*	B	Ca	Zn	Mn	Mg	-	Yes	0.738	Syn.	
23	*rib4*	B	Ca	Zn		Mg	-	Yes	1.887	Sup.	VI
24	*rpl22a*	C	Ca				+	Yes	1.057	Unaltered	VII
25	*sac1*	C	Ca				+	Yes	1.547	Syn.	IX
26	*sod1*	A	Ca				+	Yes	1.123	Syn.	
27	*swi3*	A	Ca		Mn		-	Yes	1.132	Syn.	V
28	*tef4*	A	Ca		Mn		-	No	0.724	Syn.	III
29	*tpd3*	C	Ca		Mn		-	Yes	1.000	Syn.	
30	*trk1*	C	Ca				+	Yes	1.566	Unaltered	V
31	*ubp3*	A	Ca				+	Yes	1.189	Sup.	IX
32	*vma1*	B	Ca	Zn	Mn	Mg	-	No	0.467	Syn.	I
33	*vma10*	B	Ca	Zn	Mn	Mg	-	No	0.399	Syn.	I
34	*vma11*	B	Ca	Zn	Mn	Mg	-	No	0.361	Syn.	I
35	*vma12*	B	Ca	Zn	Mn	Mg	-	No	0.409	Syn.	I

Continued on following page

Fig. S1 —Continued

No.	Mutant	Growth Type[a]	Divalent cation sensitivity				Pet phenotype	Quinacrine[b]	Relative Ca^{2+} content (-fold)[c]	$+Ca^{2+}$ +FK506[d]	Class[e]
36	*vma13*	B	Ca	Zn	Mn	Mg	-	No	0.429	Syn.	III
37	*vma16*	B	Ca	Zn	Mn	Mg	-	No	0.261	Syn.	I
38	*vma2*	B	Ca	Zn	Mn	Mg	-	No	0.342	Syn.	I
39	*vma21*	B	Ca	Zn	Mn	Mg	-	No	0.491	Syn.	
40	*vma22*	B	Ca	Zn	Mn	Mg	-	No	1.085	Syn.	I
41	*vma3*	B	Ca	Zn	Mn	Mg	-	No	0.314	Syn.	I
42	*vma4*	B	Ca	Zn	Mn	Mg	-	No	0.550	Syn.	I
43	*vma5*	B	Ca	Zn	Mn	Mg	-	No	0.508	Syn.	I
44	*vma6*	B	Ca	Zn	Mn	Mg	-	No	0.375	Syn.	I
45	*vma7*	B	Ca	Zn	Mn	Mg	-	No	0.424	Syn.	I
46	*vma8*	B	Ca	Zn	Mn	Mg	-	No	0.442	Syn.	I
47	*vps11*	A	Ca	Zn	Mn		-	m.d	4.245	Syn.	II
48	*vps15*	C	Ca	Zn	Mn	Mg	-	m.d	3.745	Syn.	VII
49	*vps16*	A	Ca	Zn		Mg	-	m.d	5.802	Syn.	II
50	*vps18*	A	Ca	Zn	Mn	Mg	-	m.d	4.283	Syn.	II
51	*vps33*	A	Ca	Zn		Mg	-	m.d	3.142	Syn.	II
52	*vps34*	B	Ca	Zn	Mn	Mg	-	m.d	4.462	Syn.	VII
53	*vps36*	C	Ca				+	m.d	0.883	Sup.	
54	*vps45*	A	Ca				-	m.d	1.764	Syn.	IX
55	*whi3*	C	Ca				-	Yes	0.923	Unaltered	V
56	*yel045c*[f]	B	Ca				+	Yes	0.799	Sup.	VI
57	*ykl118*[g]	B	Ca	Zn	Mn	Mg	-	No	0.616	Syn.	I
58	*yor331c*[h]	B	Ca	Zn	Mn	Mg	-	No	0.469	Syn.	I
59	*ypr099c*[i]	B	Ca	Zn	Mn	Mg	-	No	0.380	Syn.	I
60	*zap1*	C	Ca				+	Yes	1.113	Sup.	IX
61	*zds1*	C	Ca				+			Unaltered	IX
62	*zuo1*	C	Ca		Mn		+	Yes	2.425	Unaltered	II

[a]A, normal growth in YPD and complete growth defect in Ca^{2+}-rich medium; B, slow growth in YPD medium and complete growth defect in Ca^{2+}-rich medium; C, normal growth in YPD and partial growth defect in Ca^{2+}-rich medium.
[b]Yes, vacuole was stained with quinacrine; No, vacuole was not stained with quinacrine; m.d, morphological defects in vacuole;
[c]Compared to intracellular Ca^{2+} content of the wild-type cells. Data were obtained from Ohnuki *et al.*,（2007）and Yoshida *et al.*, (2013).
[d]Sup. and Syn., Ca^{2+} sensitivity of *cls* mutant were alleviated and aggravated by the addition of 0.4 μg/ml FK506; Unaltered, Ca^{2+} sensitivity of *cls* mutant were not altered by the addition of 0.4 μg/ml FK506.
[e]Mutants were classified as described in Fig. 5.
[f]Dubious ORF opposite *GLY1*.
[g]Dubious ORF opposite *VMA1*.
[h]Dubious ORF opposite *VMA4*.
[i]Dubious ORF.

Figures

Fig. 3

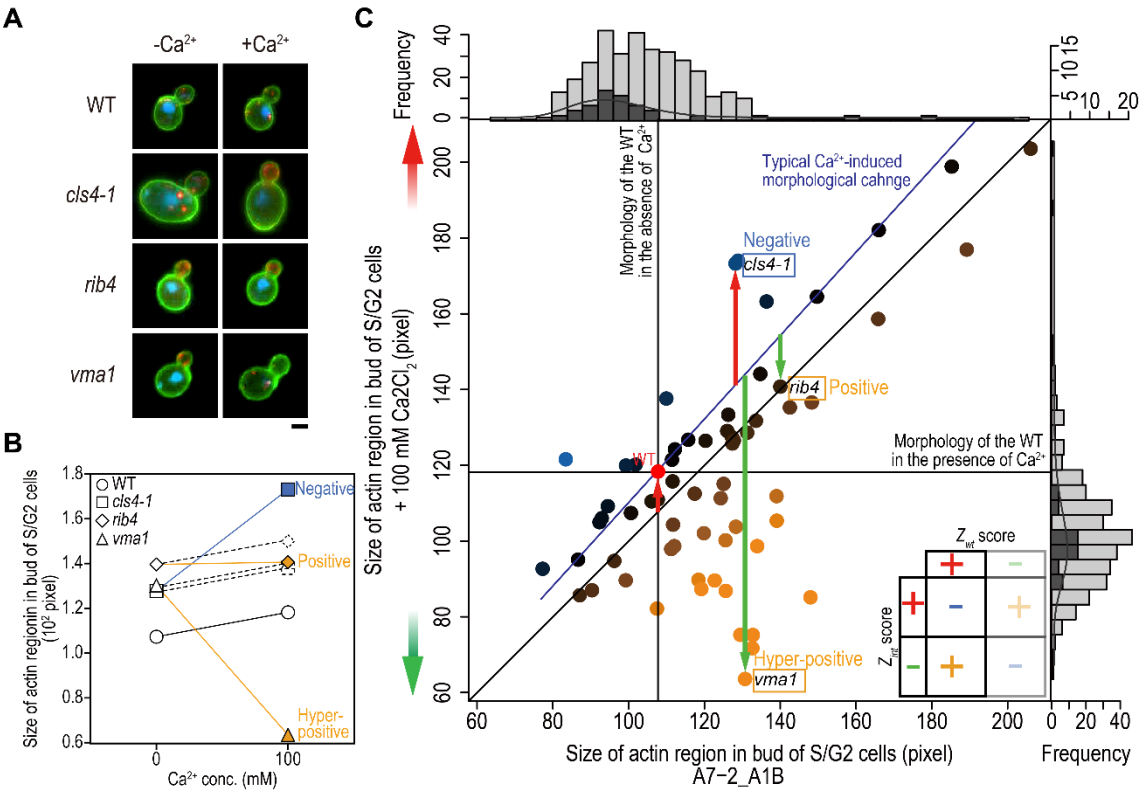

Figure 3. Systematic identification of Ca^{2+}-*cls* interactions. A. Representative cell images at S/G2 phase from five independent experiments are shown. Colors indicate the cell wall (green), actin (red), and DNA (blue). Bar, 1 μm. **B.** Size of actin region in bud of S/G2 cells of the wild-type and indicated *cls* mutant cells in YPD supplemented with or without 100 mM $CaCl_2$ were calculated from CalMorph parameter value A7-2_A1B. Dashed lines indicate expected morphological change of each *cls* mutant expected from morphological change of the wild-type. Orange and blue symbols indicate *cls* mutants representing positive and negative Ca^{2+}-*cls* interactions, respectively. **C.** Parameter values of A7-2_A1B in each of the wild-type cells and the 62 *cls* mutants in the absence (x axis) or presence (y axis) of 100 mM $CaCl_2$. Orange or blue circle indicate positive or negative Ca^{2+}-*cls* interaction of corresponding *cls* mutant, respectively. Vertical and horizontal black lines indicate parameter value of the wild-type cell in the absence or presence of 100 mM $CaCl_2$, respectively. A navy curve traces typical parameter values expected from Ca^{2+}-induced parameter change of the wild-type. Dark and light gray histograms indicate distribution of the wild-type and the *cls* mutants in the absence (upper) or presence (light) of 100 mM $CaCl_2$. Gray curves in the histograms indicate probability densities of the wild-type cells in each condition. Inset; signs of phenotypic interaction score (termed π score) calculated from Z_{wt} score which indicates degree of Ca^{2+}-induced morphological change of the wild-type and Z_{int} score which indicates degree of Ca^{2+}-*cls* interaction (see Materials and methods).

Fig. 4

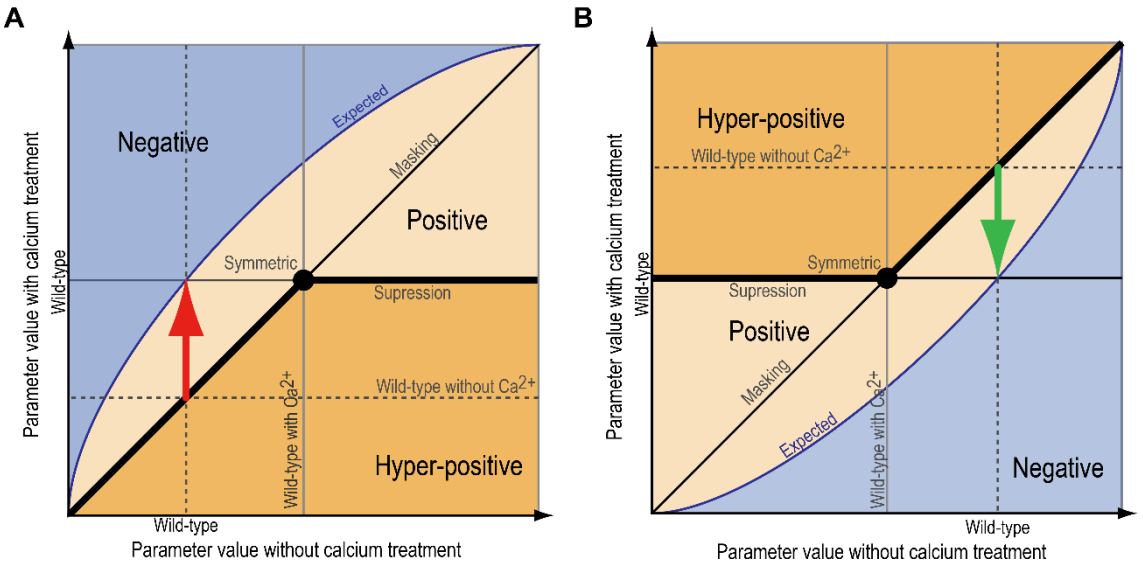

Figure 4. A graphical representation of the three types of Ca^{2+}-*cls* interactions for morphological phenotype. A. B. Red and green arrows indicate cases where parameter values of the wild-type are increased and decreased by Ca^{2+} treatment, respectively. Blue curves traces typical parameter values in the presence of high Ca^{2+} expected from Ca^{2+}-induced morphological changes of the wild-type. Deviations from the expected value in the same direction with Ca^{2+}-induced morphological change of the wild-type are scored as negative Ca^{2+}-*cls* interaction (blue-colored area). Deviations from the expected values in the opposite direction with Ca^{2+}-induced morphological change of the wild-type are classified into positive or hyper-positive interactions. In case of positive Ca^{2+}-*cls* interactions (light-orange-colored area), *cls* mutants exhibit less Ca^{2+}-induced morphological change than that expected from the wild-type, which is classified into symmetric, masking, and suppression subcategories, as described previously (Dixon *et al.*, 2009). In case of hyper positive Ca^{2+}-*cls* interactions (dark-orange-colored area), *cls* mutants exhibit Ca^{2+}-induced morphological change in the opposite direction to that of the wild-type (lower or higher than the diagonal line in Fig. 4 A or B, respectively), and lower or higher level compared to that of the wild type in the presence of 100 mM $CaCl_2$ (lower or higher than horizontal black line in Fig. 4 A or B, respectively).

Fig. 5

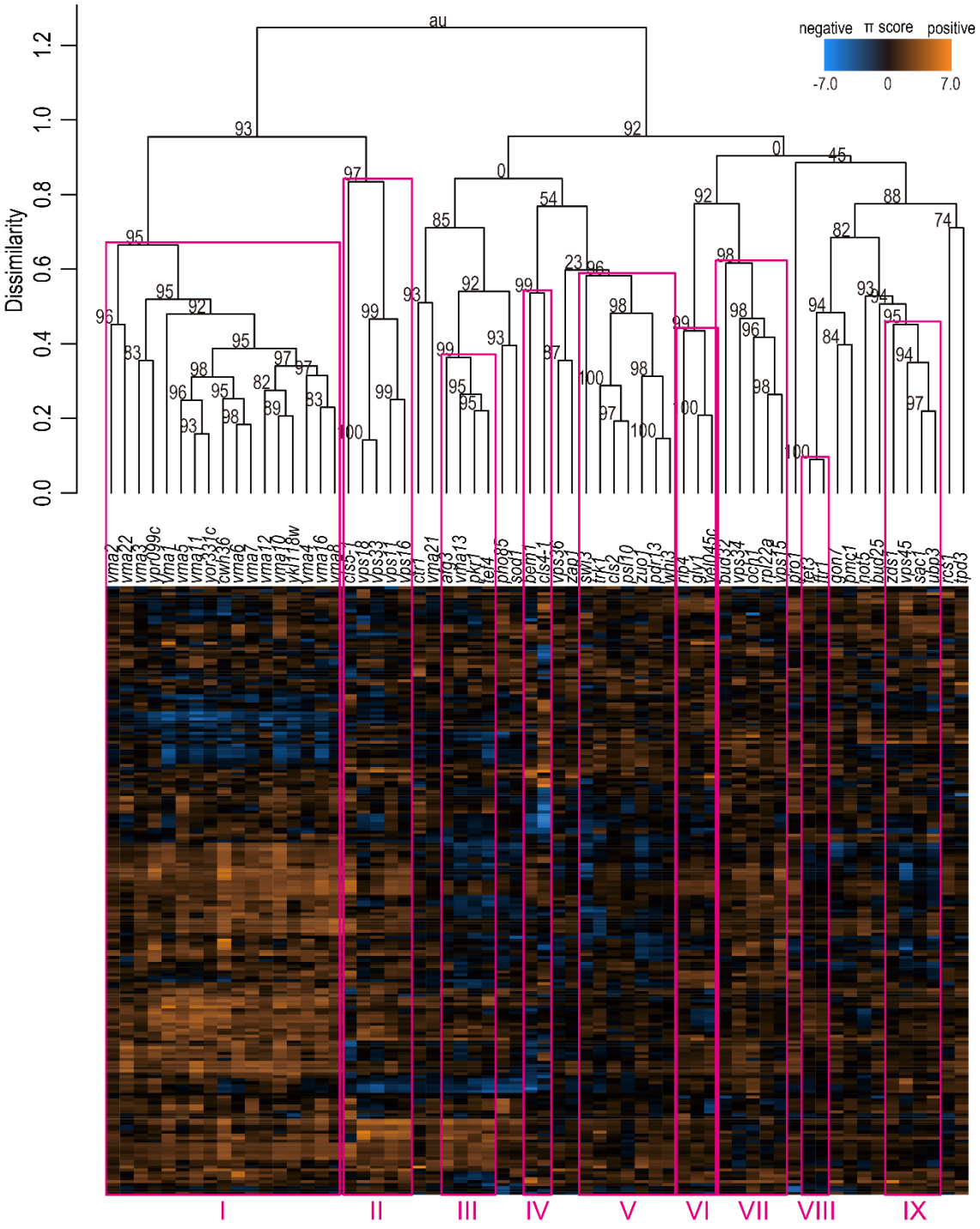

Figure 5. Cluster analysis of the *cls* mutants based on the similarities of the Ca^{2+}-*cls* interaction profiles. The orange and blue boxes indicate π scores that reflect degree of positive and negative Ca^{2+}-*cls* interactions. Dissimilarity indicates 1 - correlation between the vectors of 209 dimensions. The magenta rectangles indicate robustly clustered mutant classes at AU *P* value > 0.95 calculated by the multi-scale bootstrap technique with 3000 iterations (Suzuki and Shimodaira, 2006).

Fig. 6

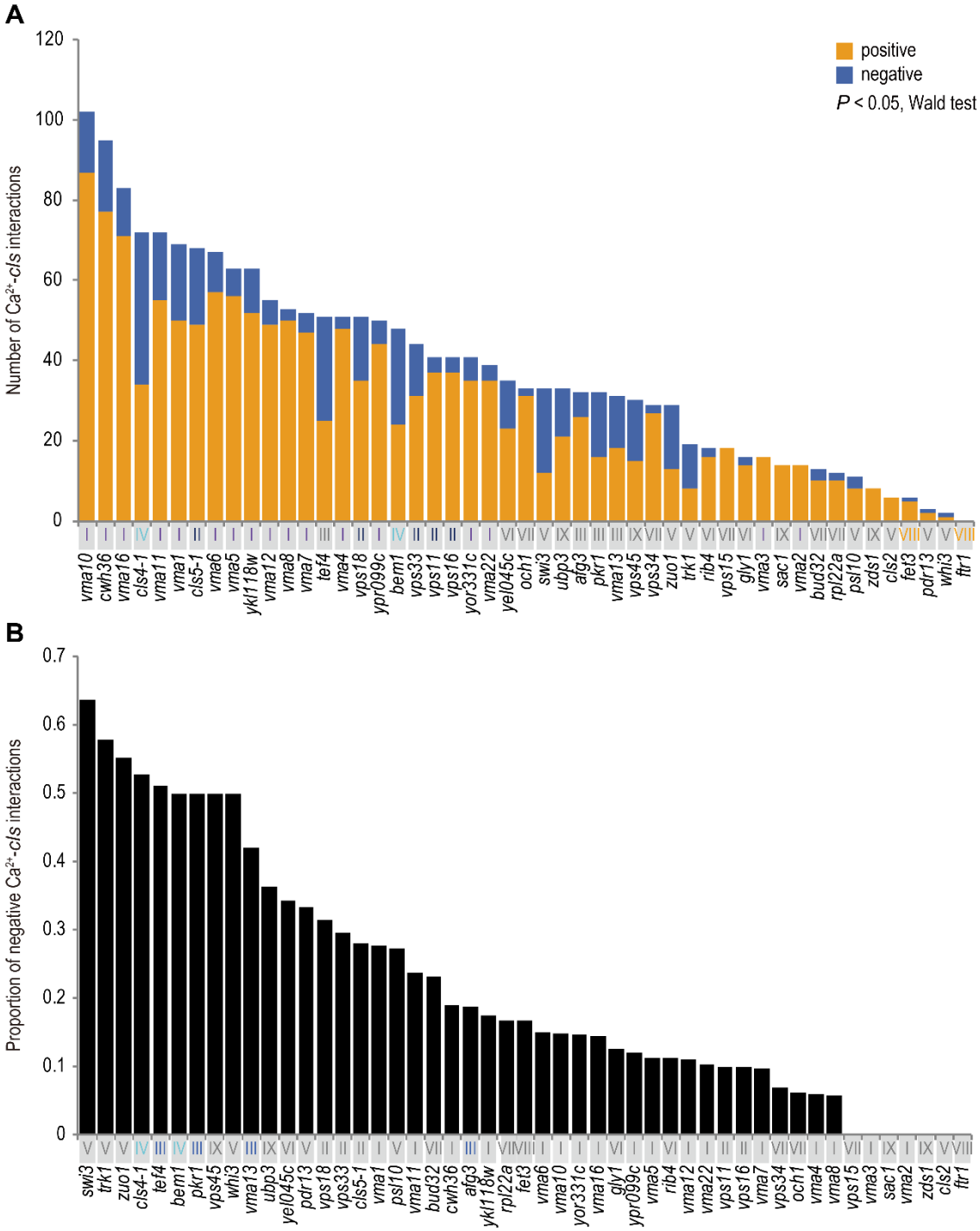

Figure 6. Properties of Ca^{2+}-*cls* interaction profiles in the *cls* mutants. A. Number of significant positive and negative interactions in the 209 parameters among indicated *cls* mutants. The orange and blue bars indicate significant positive and negative Ca^{2+}-*cls* interactions ($P < 0.05$, Wald test). Roman number (I–IX) of each *cls* mutant corresponds to the detected nine classes in Fig. 5. Colors highlighted *cls* mutants showing high (class I, II, and IV) and low (class VIII) number of Ca^{2+}-*cls* interactions, respectively. **B.** The proportion of significant negative Ca^{2+}-*cls* interactions. Colors highlighted *cls* mutants showing high proportion of negative Ca^{2+}-*cls* interactions (class III and IV).

Fig. 7

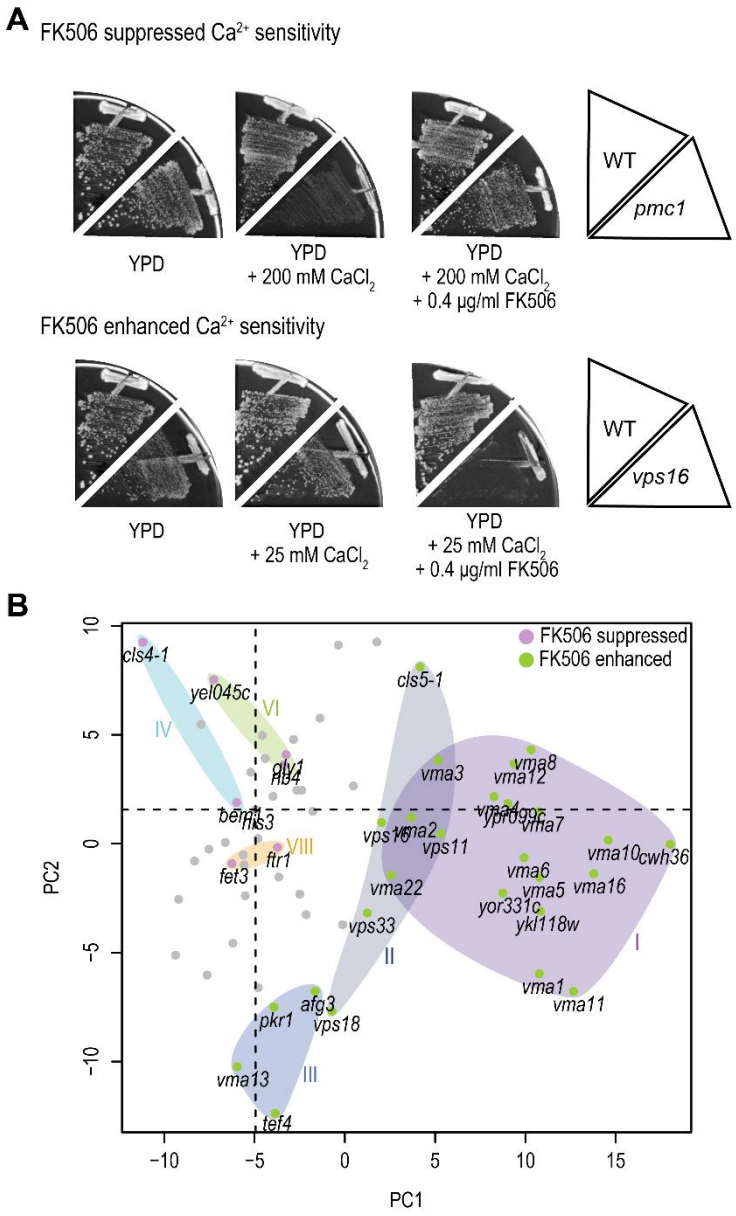

Figure 7. The alleviating and aggravating effects of FK506 on cell growth of the *cls* mutants in the presence of high Ca^{2+}. A. An example of aggravating and alleviating effects on cell growth of *cls* mutants under high Ca^{2+} condition. Growth of *pmc1* mutant cells were tested on YPD supplemented with 200 mM $CaCl_2$ in the absence and presence of 0.4 μg/ml FK506. Growth of *vps16* mutant cells were tested on YPD supplemented with 25 mM $CaCl_2$ in the absence and presence of 0.4 μg/ml FK506. Cells were incubated for 4 days at 30 ºC. Other conditions tested were shown in Fig. S4. **B.** A scatterplot of the PC scores for PC1 and PC2 of the Ca^{2+}-*cls* interaction profiles. Strains are represented by their coordinates along the first two PCs. Roman numbers correspond to the detected classes in Fig, 5. Purple and green circles indicate FK506-suppressed and FK506-enhanced Ca^{2+} sensitivity, respectively. All *cls* mutants classified in class I, II, and III showed FK506-enhanced Ca^{2+} sensitivity whereas all *cls* mutants classified in class IV, VI, and VIII showed FK-506 suppressed Ca^{2+} sensitivity.

Fig. 8

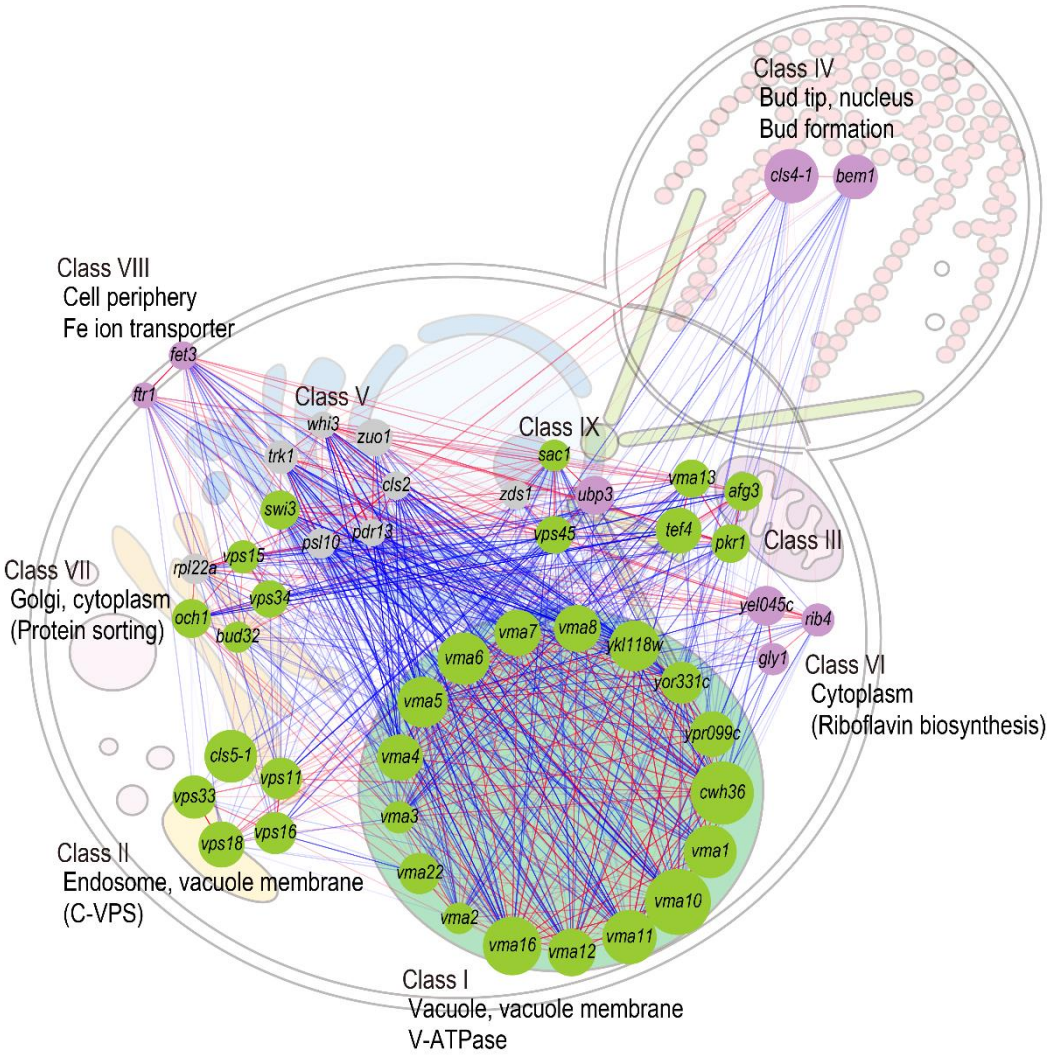

Figure 8. A correlation-based network of *cls* mutants. Similarities of Ca^{2+}-*cls* interaction profiles were measured for all gene pairs by calculating Pearson product-moment correlation coefficients (PCCs) form the Ca^{2+}-*cls* interaction matrix. Gene pairs whose profiles similarity exceed a |PCC| > 0.2 threshold were connected in the network. Edges connect gene pairs that showed positive (red line) or negative (blue line) correlation of Ca^{2+}-*cls* interaction profile. Node size and color represent the number of significant Ca^{2+}-*cls* interactions (Fig. 6 A) and the effects of FK506 on each *cls* mutant (Fig. S4, Table S1), respectively.

Fig. S1

PC	Parameter ID	Description	Loadings	*P* value	Z_{wt}	Morphological feature
PC1	C11-1_C	Mother cell size	-0.82	4.94E-27	-0.26	Mother cell size at G1,
	D135_A	Distance between nuclear brightest point and cell center	-0.81	1.40E-25	-1.93	S/G2, M phase, mother
	C12-1_C	Mother cell outline length	-0.80	7.87E-25	-1.16	cell fitness for ellipse at
	D117_A	Distance between nuclear gravity center and cell center	-0.80	1.37E-24	-2.01	S/G2 and M phase
	C112_C	Distance between middle point of neck and mother center	-0.80	2.62E-24	-1.31	
	D104_A1B	Distance between nuclear gravity center and mother tip	-0.79	2.93E-23	-4.02	
	D129_A1B	Distance between nuclear brightest point and mother tip	-0.76	1.22E-20	-3.90	
	C103_A1B	Long axis length in mother	-0.75	1.42E-19	-2.10	
	C128_C	Distance between middle point of neck and mother hip	-0.73	7.37E-18	-1.29	
	C103_C	Long axis length in mother	-0.73	1.16E-17	-1.64	
	D148_A	Relative distance of nuclear brightest point to cell center	-0.72	5.57E-17	-2.00	
	D142_A1B	Distance between nuclear brightest point and mother hip	-0.71	1.42E-16	-3.74	
	D127_A	Distance between nuclear brightest point and cell tip	-0.70	1.31E-15	-2.55	
	D147_A	Relative distance of nuclear gravity center to cell center	-0.69	3.00E-15	-2.12	
	D102_A	Distance between nuclear gravity center and mother tip	-0.68	1.49E-14	-2.63	
	D118_A1B	Distance between nuclear gravity center and mother center	-0.68	2.32E-14	-4.84	
	D145_A1B	Distance between nuclear outline point D7 and mother hip	-0.66	4.17E-13	-3.51	
	D148_A1B	Relative distance of nuclear brightest point to mother center	-0.65	1.19E-12	-4.86	
	D126_A1B	Distance between nuclear gravity center and mother hip	-0.65	3.94E-12	-3.80	
	D105_A	Ratio of D102 to C103	-0.64	1.04E-11	-2.75	
	D136_A1B	Distance between nuclear brightest point and mother center	-0.64	1.21E-11	-4.21	
	C13_A1B	Mother cell fitness for ellipse	0.63	2.00E-11	-3.20	
	C13_C	Mother cell fitness for ellipse	0.61	5.67E-10	-3.24	
	D117_C	Distance between nuclear gravity center in mother and mother center	-0.58	5.96E-09	-1.91	
	A102_A1B	Bud actin region ratio to total region	-0.58	7.48E-09	-0.39	
	D170_A1B	Angle between C4-1D2-1 and C4-1C1	-0.56	7.17E-08	-4.05	
	D128_C	Distance between nuclear brightest point in mother and mother tip	-0.54	3.92E-07	-2.24	
	A7-1_A1B	Size of actin region in mother	0.52	4.35E-06	0.42	
	D137_C	Distance between nuclear brightest point in bud and bud tip	-0.52	4.41E-06	-1.60	
	C115_A	Whole cell axis ratio	-0.51	8.31E-06	8.50	
	D108_C	Distance between nuclear gravity center in mother and middle point of neck	-0.50	1.33E-05	-0.01	
	C116_A1B	Axis ratio ratio	-0.50	2.53E-05	-0.64	
	A118	actin e ratio to budded cells	0.50	2.69E-05	-0.66	
	A109_A1B	Actin e ratio	0.49	3.66E-05	-0.38	
	D103_C	Distance between nuclear gravity center in mother and mother tip	-0.49	3.75E-05	-2.64	
	A112_A1B	Actin cd ratio	-0.49	5.11E-05	0.71	
	D169_A1B	Angle between C4-1D1-1 and C4-1C1	-0.48	6.28E-05	-4.46	
	C109_C	Neck width	-0.48	9.48E-05	2.58	
	A109	actin e ratio	0.47	1.83E-04	0.73	
	D147_C	Relative distance of nuclear gravity center in mother to mother center	-0.46	5.54E-04	-1.93	
	D147_A1B	Relative distance of nuclear gravity center to mother center	-0.45	1.00E-03	-5.85	
	C110_C	Distance between bud tip and mother long axis extension	-0.43	3.57E-03	-1.64	
	D161_A1B	Angle between D3-1D4-1 and C1-1C1-2 or between D3-3D4-3 and C1-1C1-2	-0.43	3.59E-03	-0.45	
	D150_C	Relative distance of nuclear brightest point in bud to bud center	-0.42	6.65E-03	-1.54	
	D130_C	Distance between nuclear brightest point in mother and middle point of neck	-0.41	8.09E-03	-0.49	

Continued on following page

Fig. S1—Continued

PC	Parameter ID	Description	Loadings	*P* value	Z_{wf}	Morphological feature
PC2	C12-2_A1B	Bud cell outline length	0.82	1.51E-27	-1.52	Ratio of cells with small,
	C123	small bud ratio to budded cells	-0.82	4.54E-27	0.87	midium, and large bud
	C123_A1B	Small bud ratio	-0.82	9.31E-27	0.89	at S/G2 phase
	A107_A1B	Actin c ratio	-0.79	1.34E-23	0.73	
	C117_A1B	Cell outline ratio	0.78	7.61E-23	-0.71	
	A116	actin c ratio to budded cells	-0.78	1.84E-22	0.34	
	C118_A1B	Cell size ratio	0.77	9.17E-22	-0.61	
	C107_A1B	Long axis length in bud	0.77	3.21E-21	-1.89	
	A7-2_A1B	Size of actin region in bud	0.71	4.44E-16	1.47	
	C124_A1B	Medium bud ratio	0.67	1.37E-13	-1.63	
	C121	medium bud ratio	0.65	3.48E-12	0.21	
	C122	large bud ratio	0.62	7.53E-11	1.99	
	D202	nuclear C ratio	0.60	1.50E-09	1.49	
	D213	nuclear C ratio to nuclear AA1BC cells	0.59	3.72E-09	1.20	
	D210	nuclear A ratio to nuclear AA1BC cells	-0.56	5.00E-08	-2.10	
	A108	actin d ratio	0.55	2.47E-07	1.98	
	A109	actin e ratio	0.54	5.87E-07	0.73	
	A108_A1B	Actin d ratio	0.52	3.49E-06	0.51	
	D114_A1B	Ratio of D110 to C128	-0.51	8.69E-06	4.35	
	A110	actin f ratio	0.49	5.89E-05	0.54	
	D152_A1B	Mobility of nucleus in mother	-0.47	2.45E-04	3.40	
	D123_C	Ratio of D121 to C107	-0.47	2.64E-04	-1.61	
	D113_C	Ratio of D109 to C107	0.46	3.05E-04	1.28	
	A109_A1B	Actin e ratio	0.46	3.20E-04	-0.38	
	A112_A1B	Actin cd ratio	-0.46	3.28E-04	0.71	
	D126_A1B	Distance between nuclear gravity center and mother hip	0.45	7.06E-04	-3.80	
	C125	large bud ratio to buded cells	0.45	7.12E-04	0.72	
	D153_C	Mobility of nucleus in bud	0.45	1.06E-03	1.59	
	C124	medium bud ratio to buded cells	0.43	2.98E-03	-1.99	
	D146_C	Distance between nuclear outline point D8 in bud and bud tip	-0.43	3.52E-03	-1.79	
	A118	actin e ratio to budded cells	0.42	4.45E-03	-0.66	
	C120	small bud ratio	-0.42	6.82E-03	2.52	
	A107	actin c ratio	-0.42	7.78E-03	1.80	

Continued on following page

Fig. S1—Continued

PC	Parameter ID	Description	Loadings	*P* value	Z_{wt}	Morphological feature
PC3	D112_C	Ratio of D108 to C128	-0.83	5.88E-29	0.82	Nuclear position and
	D125_C	Distance between nuclear gravity center in mother and mother hip	0.74	4.67E-19	-2.67	mobility in mother cell at
	D108_C	Distance between nuclear gravity center in mother and middle point of neck	-0.74	1.28E-18	-0.01	M phase
	D152_C	Mobility of nucleus in mother	-0.73	3.08E-18	1.88	
	D141_C	Distance between nuclear brightest point in mother and mother hip	0.72	4.64E-17	-2.36	
	D130_C	Distance between nuclear brightest point in mother and middle point of neck	-0.71	1.13E-16	-0.49	
	D106_C	Ratio of D103 to C103	0.68	1.52E-14	-1.98	
	D143_C	Distance between nuclear outline point D6-1 in mother and middle point of neck	-0.65	1.88E-12	0.64	
	D145_C	Distance between nuclear outline point D7 in mother and mother hip	0.63	2.97E-11	-3.54	
	D148_C	Relative distance of nuclear brightest point in mother to mother center	-0.55	1.66E-07	-2.78	
	CCV108_C	Noise of C108 C	0.53	1.37E-06	-2.36	
	D107_A1B	Ratio of D104 to C103	0.52	3.93E-06	-4.35	
	D117_C	Distance between nuclear gravity center in mother and mother center	-0.51	5.33E-06	-1.91	
	D103_C	Distance between nuclear gravity center in mother and mother tip	0.50	1.39E-05	-2.64	
	C120	small bud ratio	-0.50	1.53E-05	2.52	
	A107	actin c ratio	-0.49	4.10E-05	1.80	
	D147_C	Relative distance of nuclear gravity center in mother to mother center	-0.48	8.88E-05	-1.93	
	D114_A1B	Ratio of D110 to C128	-0.47	1.68E-04	4.35	
	D132_A1B	Distance between nuclear brightest point and middle point of neck	-0.47	1.76E-04	2.33	
	D128_C	Distance between nuclear brightest point in mother and mother tip	0.46	3.30E-04	-2.24	
	CCV117_C	Noise of C117 C	0.46	3.55E-04	-0.72	
	A103_C	Relative distance of actin patch center from neck in mother	0.46	3.62E-04	-1.05	
	CCV128_C	Noise of C128 C	0.45	8.81E-04	3.39	
	CCV118_C	Noise of C118 C	0.44	1.41E-03	-0.97	
	D210	nuclear A ratio to nuclear AA1BC cells	0.44	1.78E-03	-2.10	
	D169_C	Angle between C4-1D1-1 and C4-1C1	0.43	2.75E-03	-3.13	
	D147_A1B	Relative distance of nuclear gravity center to mother center	0.43	4.15E-03	-5.85	
PC4	D149_C	Relative distance of nuclear gravity center in bud to bud center	-0.68	2.69E-14	-3.40	Nuclear position in bud
	D119_C	Distance between nuclear gravity center in bud and bud center	-0.61	2.31E-10	-2.99	cell at M phase
	DCV121_C	Noise of D121 C	-0.59	3.20E-09	-1.62	
	DCV123_C	Noise of D123 C	-0.58	1.52E-08	-1.80	
	D150_C	Relative distance of nuclear brightest point in bud to bud center	-0.57	2.04E-08	-1.54	
	D153_C	Mobility of nucleus in bud	-0.54	7.23E-07	1.59	
	DCV139_C	Noise of D139 C	-0.49	3.36E-05	-0.56	
	DCV146_C	Noise of D146 C	-0.49	3.39E-05	0.34	
	D137_C	Distance between nuclear brightest point in bud and bud tip	-0.48	1.17E-04	-1.60	
	D113_C	Ratio of D109 to C107	-0.46	2.97E-04	1.28	
	A108_A1B	Actin d ratio	0.46	3.90E-04	0.51	
	DCV109_C	Noise of D109 C	-0.46	5.31E-04	-2.23	
	D158_C	Angle between D1-1D1-2 and C1-1C1-2	0.45	1.07E-03	-1.95	
	D159_C	Angle between D2-1D2-2 and C1-1C1-2	0.44	1.37E-03	-2.06	
	A117	actin d ratio to budded cells	0.43	2.92E-03	0.94	
	D123_C	Ratio of D121 to C107	0.42	4.95E-03	-1.61	
	D162_C	Angle between D1-1D1-2 and C1C4-1	0.42	5.21E-03	-4.02	
	D170_C	Angle between C4-1D2-1 and C4-1C1	0.42	7.07E-03	-3.62	

Continued on following page

Fig. S1—Continued

PC	Parameter ID	Description	Loadings	*P* value	Z_{wt}	Morphological feature
PC5	DCV126_A1B	Noise of D126 A1B	-0.59	2.31E-09	1.77	Noise of mother and bud
	DCV114_A1B	Noise of D114 A1B	-0.57	1.97E-08	-1.38	cell size at S/G2 phase
	CCV11-1_A1B	Noise of C11-1 A1B	-0.57	2.88E-08	2.48	
	CCV12-1_A1B	Noise of C12-1 A1B	-0.56	1.13E-07	3.53	
	CCV104_A1B	Noise of C104 A1B	-0.55	1.36E-07	-0.85	
	DCV110_A1B	Noise of D110 A1B	-0.55	1.76E-07	-2.00	
	CCV103_A1B	Noise of C103 A1B	-0.53	1.62E-06	4.69	
	CCV104_C	Noise of C104 C	-0.51	1.12E-05	0.45	
	CCV128_A1B	Noise of C128 A1B	-0.50	2.62E-05	2.59	
	CCV101_A1B	Noise of C101 A1B	-0.48	9.35E-05	1.90	
	DCV152_A1B	Noise of D152 A1B	-0.48	1.12E-04	-1.69	
	CCV11-1_C	Noise of C11-1 C	-0.46	3.83E-04	3.70	
	DCV132_A1B	Noise of D132 A1B	-0.45	6.86E-04	-1.79	
	CCV110_A1B	Noise of C110 A1B	-0.45	7.87E-04	1.17	
	CCV105_A1B	Noise of C105 A1B	-0.44	1.23E-03	1.39	
	DCV142_A1B	Noise of D142 A1B	-0.44	1.29E-03	1.59	
	DCV104_A1B	Noise of D104 A1B	-0.44	1.77E-03	1.64	
	CCV106_A1B	Noise of C106 A1B	-0.44	2.00E-03	0.96	
	CCV12-1_C	Noise of C12-1 C	-0.43	3.37E-03	4.78	
	DCV129_A1B	Noise of D129 A1B	-0.41	8.29E-03	1.50	
PC6	ACV8-2_A1B	Noise of A8-2 A1B	-0.54	4.86E-07	0.71	Noise of area of actin
	ACV7-2_A1B	Noise of A7-2 A1B	-0.50	1.74E-05	0.87	region and brightness in
	C109_A1B	Neck width	-0.45	1.02E-03	1.62	bud cell at S/G2 phase
	C124	medium bud ratio to buded cells	0.43	2.82E-03	-1.99	
PC7	CCV128_C	Noise of C128 C	-0.51	7.28E-06	3.39	Noise of mother cell
	D139_C	Distance between nuclear brightest point in bud and bud tip	-0.51	7.40E-06	-1.79	size at M phase
	CCV103_C	Noise of C103 C	-0.50	2.03E-05	5.30	
	DCV148_C	Noise of D148 C	-0.47	2.00E-04	1.82	
	CCV101_C	Noise of C101 C	-0.46	4.57E-04	2.03	
	C125	large bud ratio to buded cells	-0.44	1.16E-03	0.72	
	DCV135_C	Noise of D135 C	-0.43	3.10E-03	3.12	
	CCV12-1_C	Noise of C12-1 C	-0.42	7.07E-03	4.78	
PC8	C105_C	Neck position	0.59	4.67E-09	-0.12	Neck position at M
	D158_C	Angle between D1-1D1-2 and C1-1C1-2	0.52	2.65E-06	-1.95	phase
	D159_C	Angle between D2-1D2-2 and C1-1C1-2	0.52	3.49E-06	-2.06	
	C106_C	Bud direction	0.52	4.80E-06	-1.76	
	CCV117_C	Noise of C117 C	0.51	8.55E-06	-0.72	
	CCV118_C	Noise of C118 C	0.50	1.39E-05	-0.97	
	A110_C	Actin f ratio	-0.49	4.42E-05	0.18	
	A109_C	Actin e ratio	0.46	5.56E-04	-0.24	
	C124_C	Medium bud ratio	0.43	2.78E-03	-1.63	
	C125_C	Large bud ratio	-0.43	2.95E-03	1.58	
PC9	CCV12-1_A1B	Noise of C12-1 A1B	0.55	2.58E-07	3.53	Noise of mother cell size
	CCV128_A1B	Noise of C128 A1B	0.52	4.50E-06	2.59	at S/G2 phase
	CCV11-1_A1B	Noise of C11-1 A1B	0.49	3.06E-05	2.48	
	CCV103_A1B	Noise of C103 A1B	0.47	1.32E-04	4.69	
	CCV104_A1B	Noise of C104 A1B	0.45	1.08E-03	-0.85	
	DCV109_C	Noise of D109 C	0.44	1.27E-03	-2.23	
PC10	C125_A1B	Large bud ratio	0.42	5.31E-03	0.69	Ratio of cells with large bud at S/G2 phase
PC12	DCV141_C	Noise of D141 C	-0.43	2.74E-03	-1.16	Noise of nuclear posiion at M phase
PC14	DCV182_A	Noise of D182 A	-0.42	6.54E-03	0.06	Noise of nuclear axis ratio at G1 phase

Continued on following page

Fig. S1—Continued

PC	Parameter ID	Description	Loadings	*P* value	Z_{wt}	Morphological feature
PC17	ACV8-1_A1B	Noise of A8-1 A1B	-0.47	1.90E-04	-0.67	Noise of area of actin region in mother cell at S/G2 phase
PC18	DCV147_A	Noise of D147 A	0.41	9.09E-03	-0.93	Noise of mother cell size at S/G2 phase
PC19	D166_C	Angle between D1-1D1-2 and C4-1C4-2	-0.46	4.98E-04	-0.98	Relative nuclear position at M phase
	D167_C	Angle between D2-1D2-2 and C4-1C4-2	-0.45	5.68E-04	-0.87	

Figure S1. Parameter descriptions for the principal components representing independent morphological features of Ca^{2+}-*cls* interactions among the *cls* mutants. Positive and negative values of loadings indicate correlations between PC scores and parameter values of the null distribution. Red and green boxes indicate positive and negative values of Z_{wt} scores, respectively, which indicate increases and decreases of parameter values of the wild-type by Ca^{2+} treatment. The *P* value was calculated by *t* test of loadings, where the alternative hypothesis of the *t* test is loadings $\neq 0$ (Ohnuki *et al.*, 2012). First 19 PCs (PC1 to PC19) reached to 70% of the CCR, which explained 70% of variance in the 209 parameters.

Fig. S2

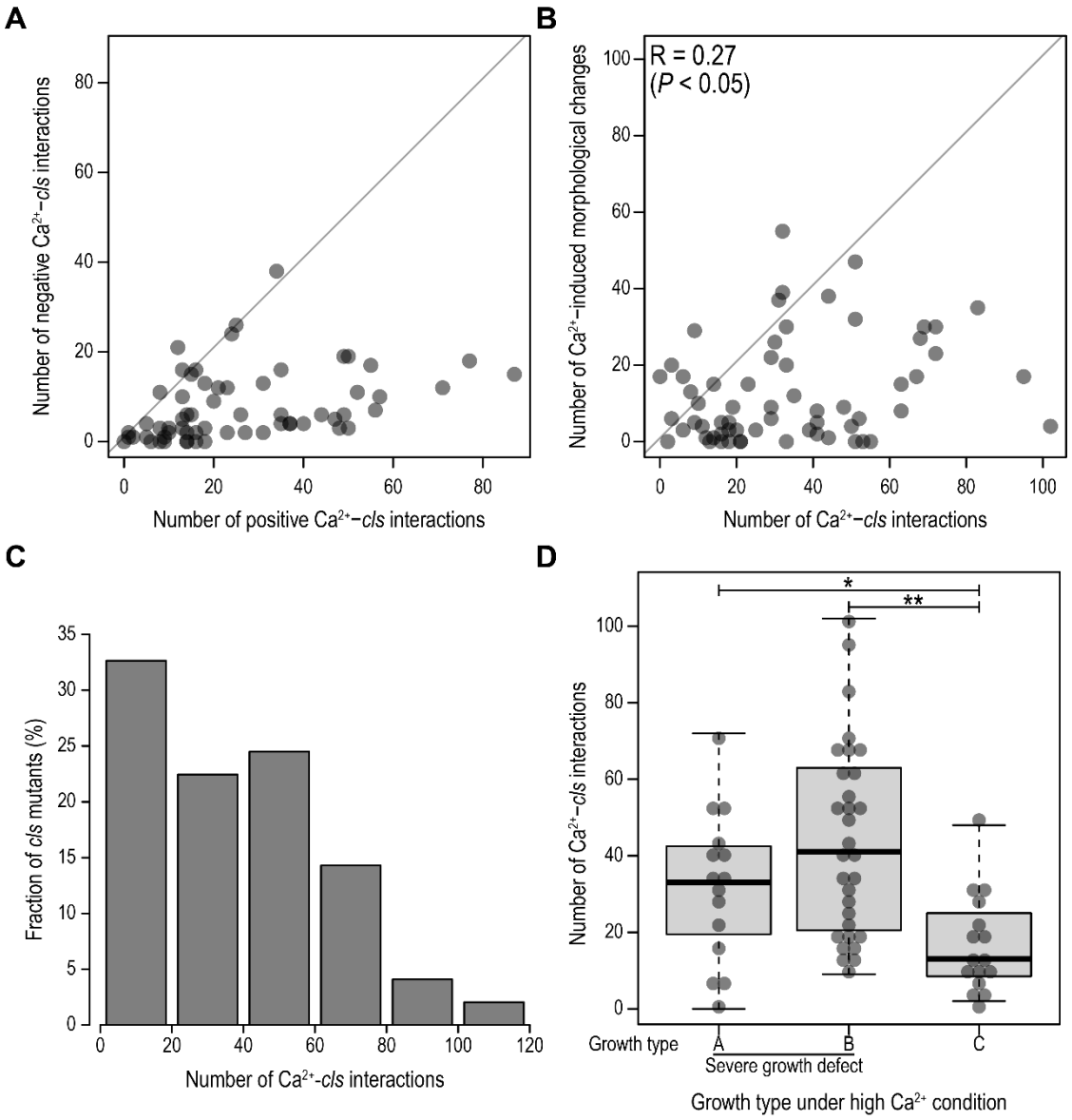

Figure S2. Properties of Ca^{2+}-*cls* interactions among the *cls* mutants. A. Comparison of number of positive Ca^{2+}-*cls* interactions with that of negative ones in *cls* mutants. Gray spots indicate individual *cls* mutants. For each parameter, number of positive and negative Ca^{2+}-*cls* interactions were examined using Wald-test ($P < 0.05$). **B.** Correlation between number of Ca^{2+}-*cls* interactions and that of Ca^{2+}-induced morphological changes in the *cls* mutants. Gray spots indicate individual *cls* mutants. For each parameter, number of significantly changed parameters were determined using *U* test, as previously described (Ohnuki *et al.*, 2007). The R value indicates correlation coefficient. **C.** The distribution of number of Ca^{2+}-*cls* interactions. **D.** Comparison of growth type under high Ca^{2+} condition with number of Ca^{2+}-*cls* interactions in the *cls* mutants. Bars indicate maximum and minimum value of each sample, respectively. Black lines indicate median of each sample. Growth types A, B, and C were determined as described previously (Ohnuki *et al.*, 2007). Growth type A, normal growth in YPD and complete growth defect in Ca^{2+}-rich medium; Growth type B, slow growth in YPD medium and complete growth defect in Ca^{2+}-rich medium; Growth type C, normal growth in YPD and partial growth defect in Ca^{2+}-rich medium. * and ** indicate $P < 0.05$ and < 0.0005 (*U* test), respectively.

Fig. S3

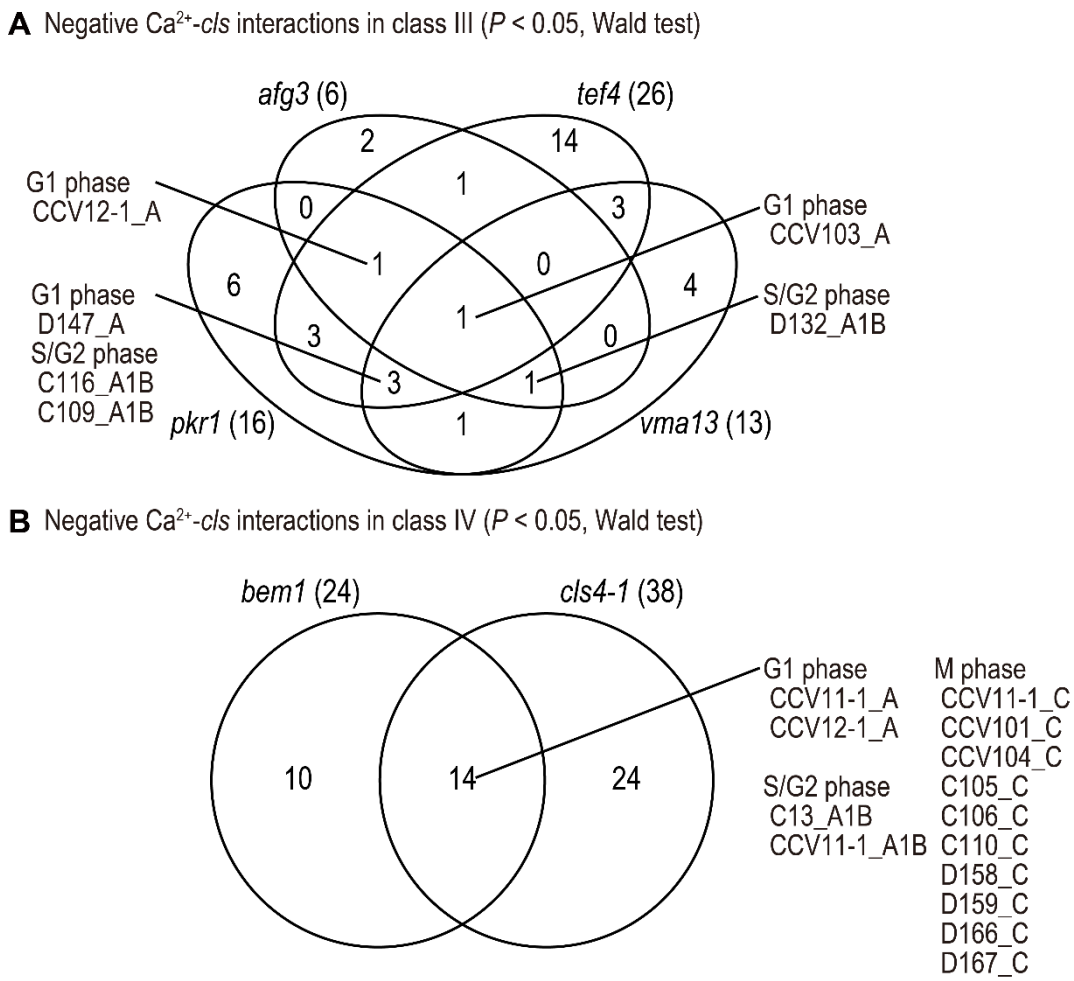

Figure S3. Common negative Ca^{2+}-*cls* interactions in class III and IV *cls* mutants. A. B. Venn diagrams with the number of parameters showing significant negative Ca^{2+}-*cls* interactions were detected in class III and IV *cls* mutants, respectively (Wald-test, $P < 0.05$).

Fig. S4

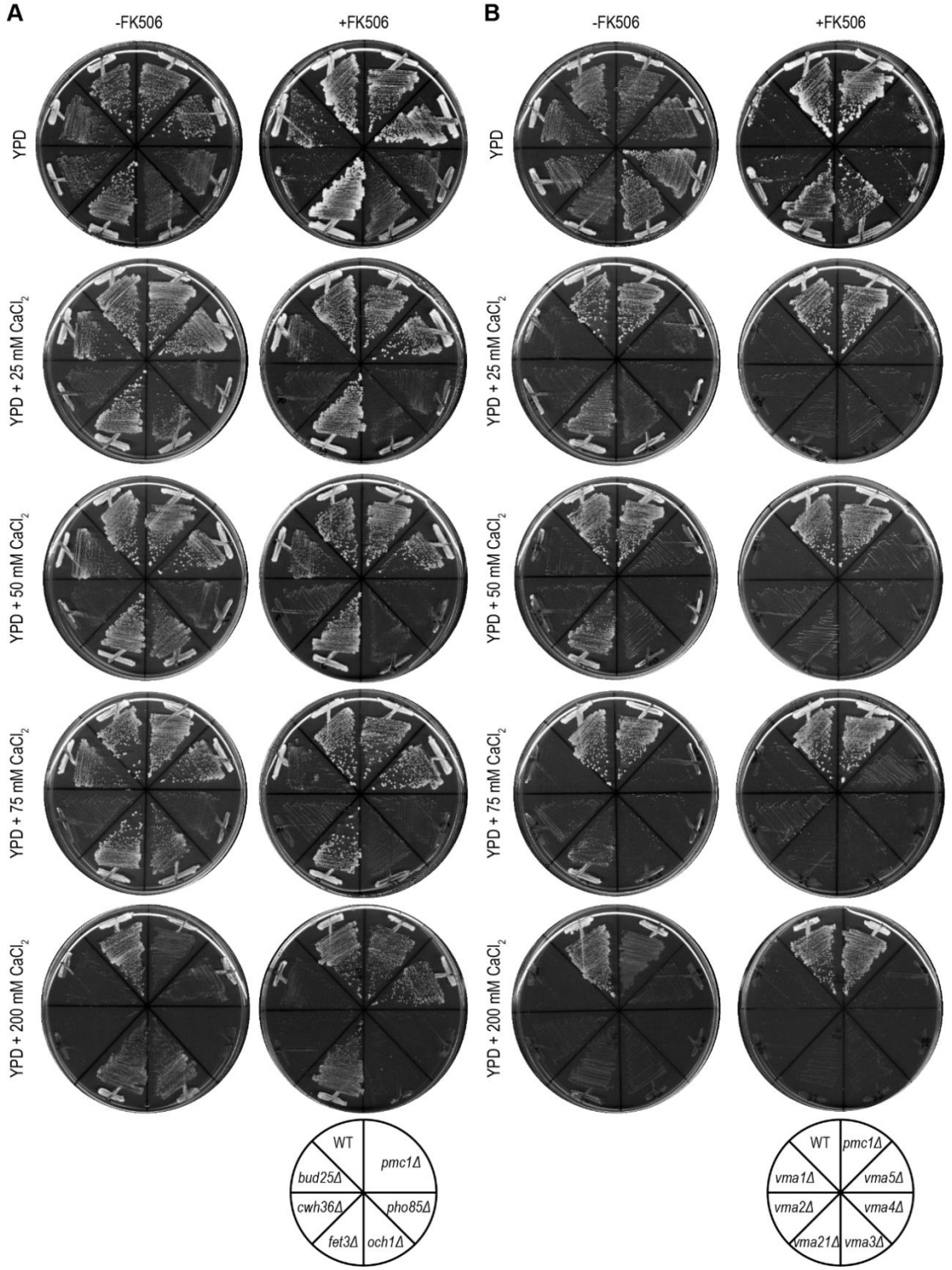

Continued on following page

Fig. S4—Continued

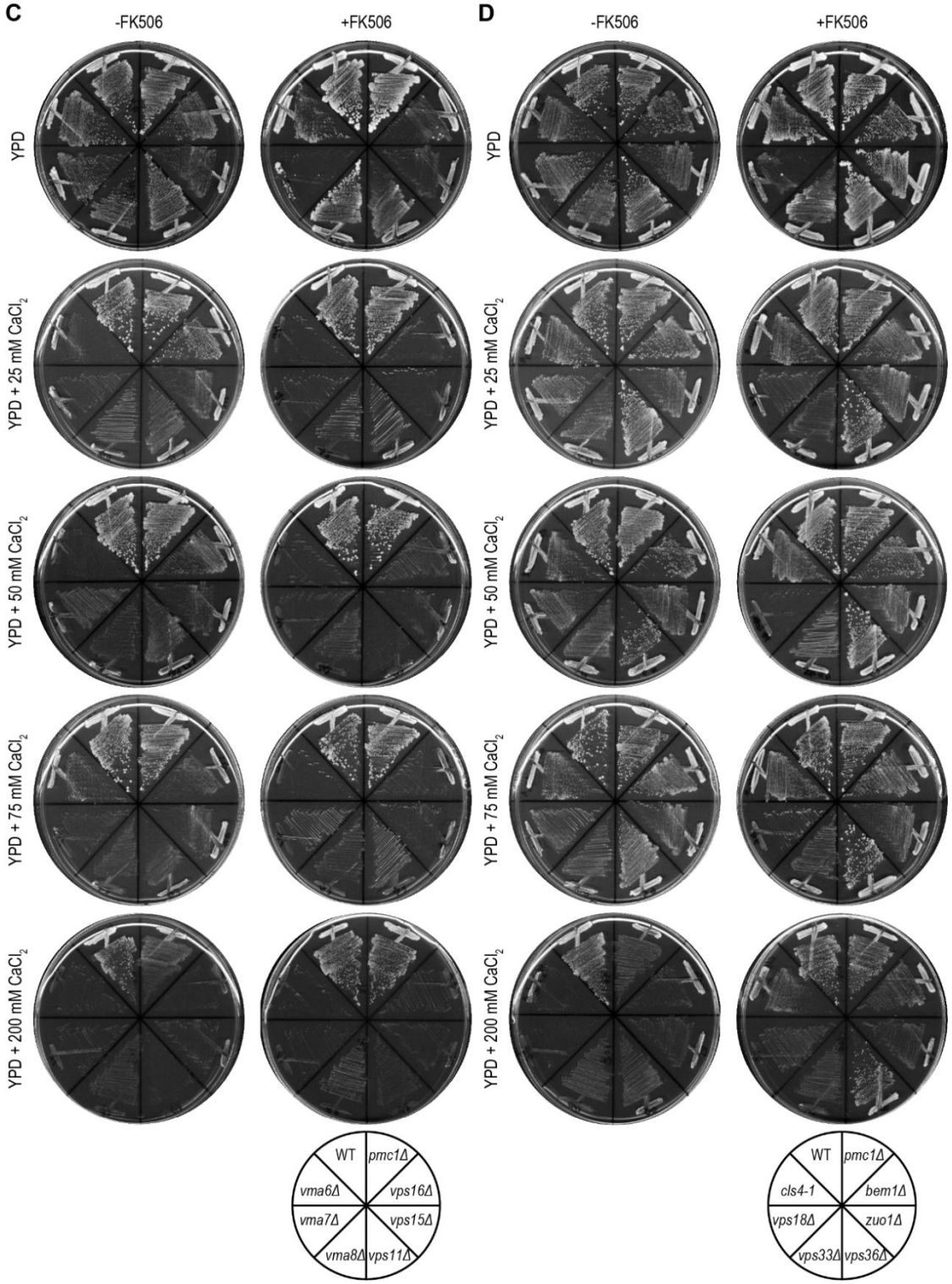

Continued on following page

Fig. S4—Continued

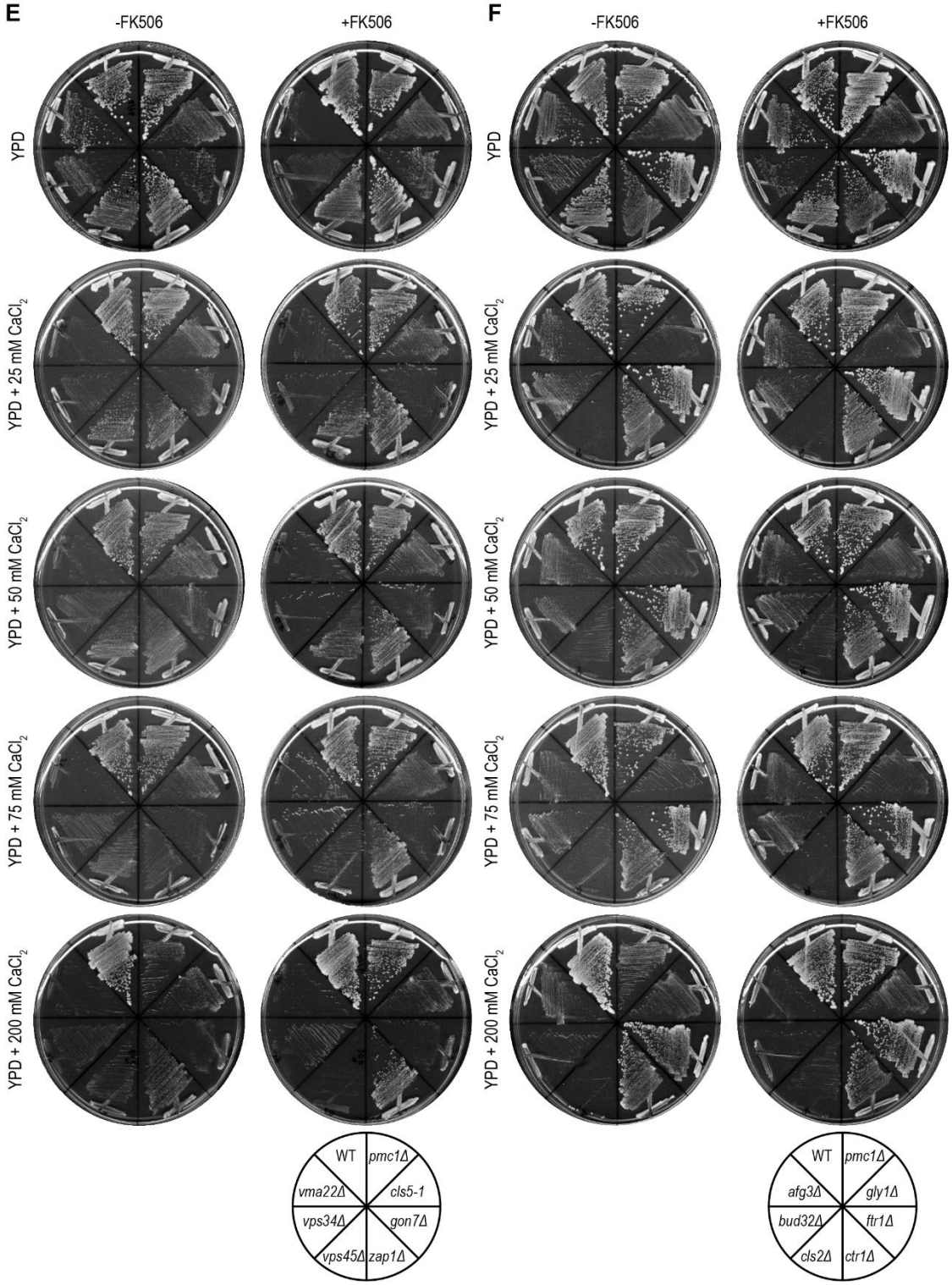

Continued on following page

Fig. S4—Continued

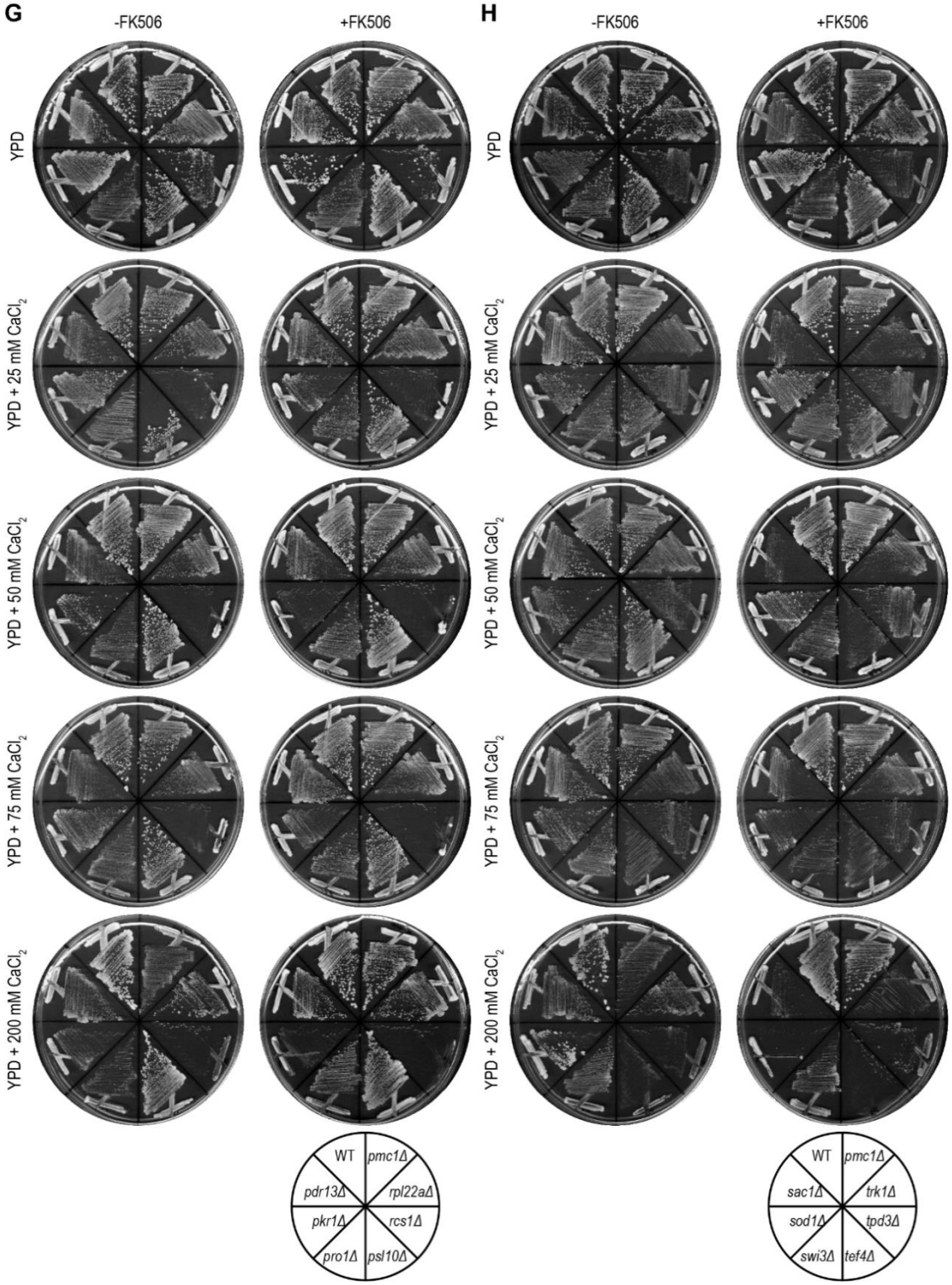

Continued on following page

Fig. S4—Continued

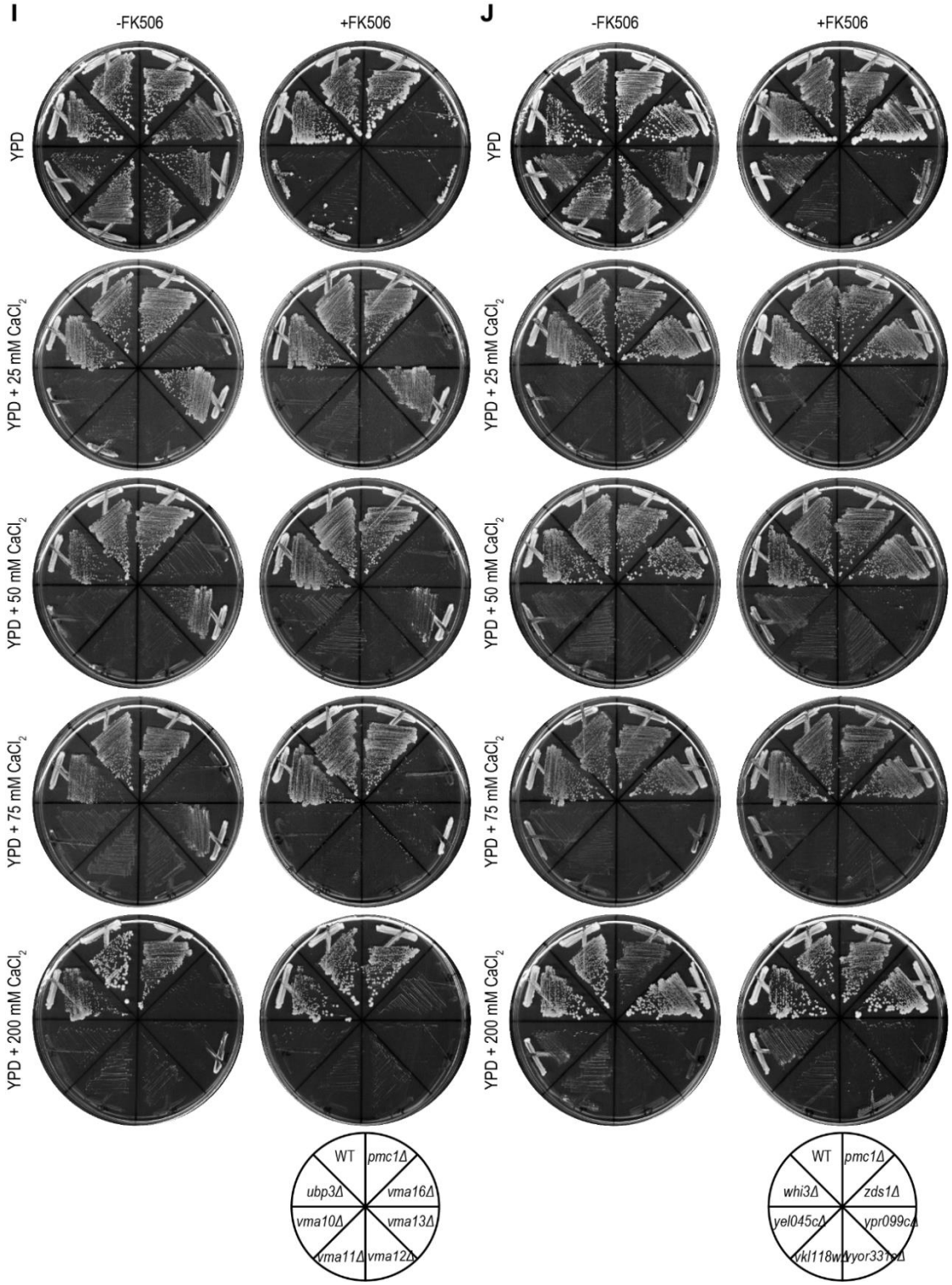

Continued on following page

Fig. S4—Continued

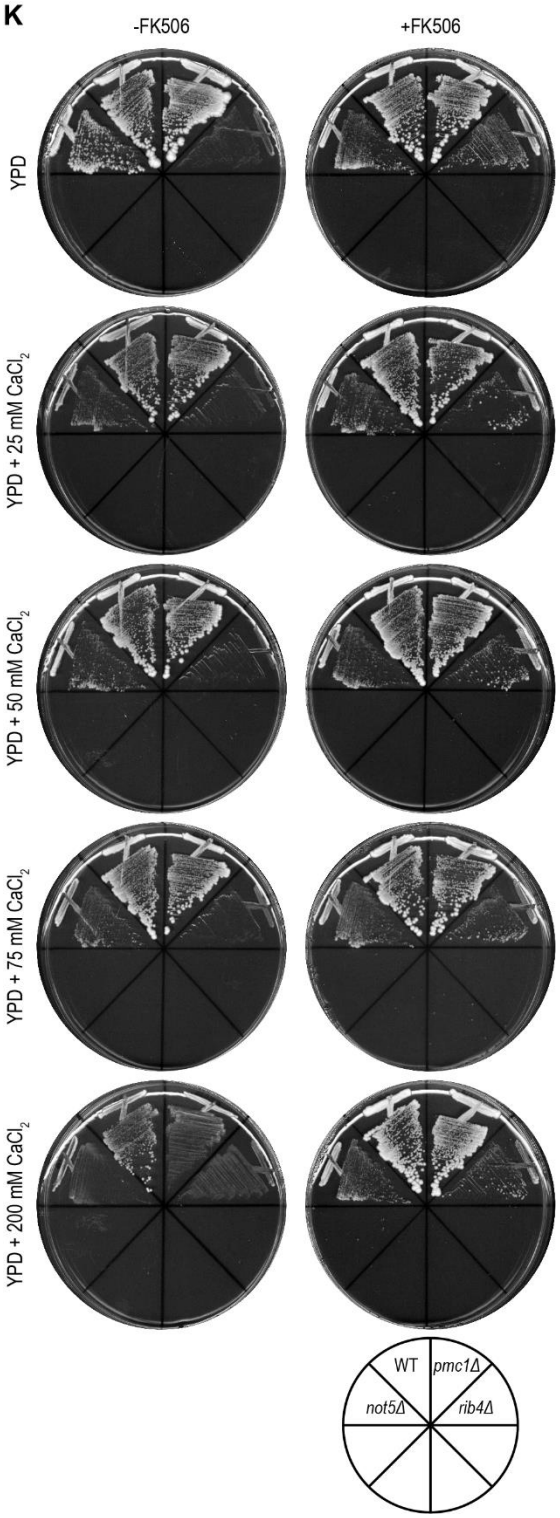

Figure S4. Ca^{2+} sensitivity of the *cls* mutants in the presence of FK506. A-K. Cell growth of the wild-type (*his3Δ*) and indicated *cls* mutant cells were tested on YPD supplemented with 0, 25, 50, 75, and 200 mM $CaCl_2$ in the absence (-FK506) and presence (+FK506) of 0.4 μg/ml FK506, respectively. The cells were incubated for 4 days at 30ºC.

Fig. S5

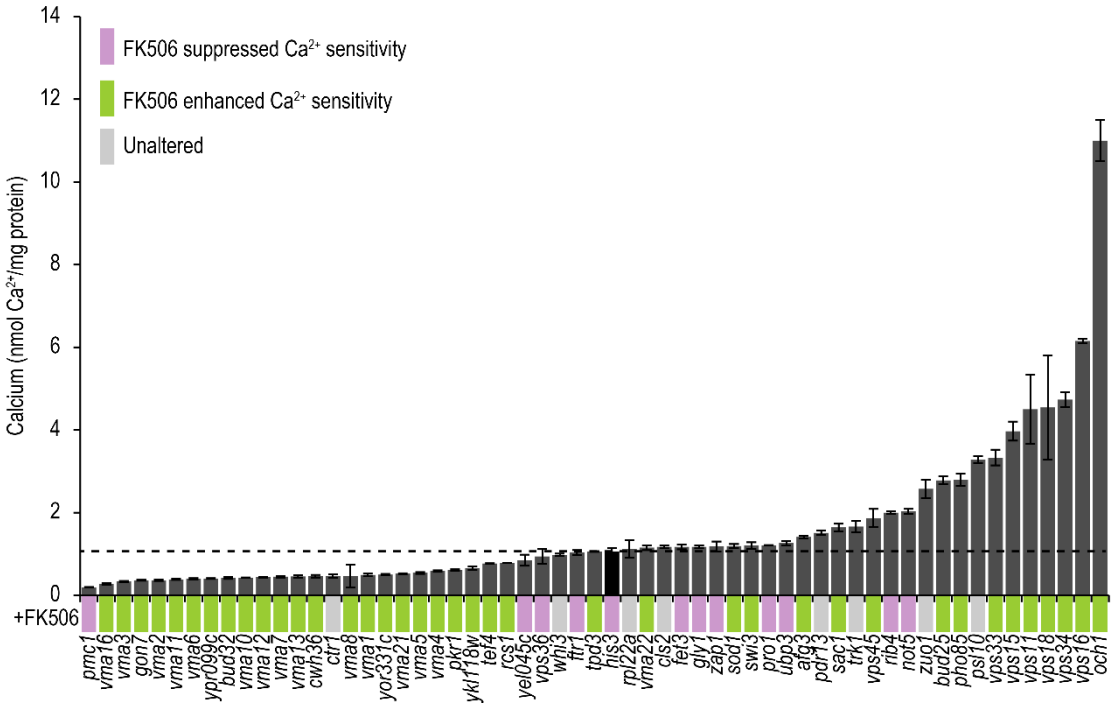

Figure S5. Relationship between intracellular Ca^{2+} content and the effects of FK506 on cell growth in the *cls* mutants. Data of intracellular Ca^{2+} content in the wild-type (black bar) and indicated *cls* mutants (gray bars) cells were obtained from Ohnuki *et al.*, (2007). The dotted line indicates intracellular Ca^{2+} level of the wild-type cells (1.06 ± 0.08 nmole calcium/mg protein). Error bars indicate ±S.D. Purple and green boxes indicate alleviating and aggravating effects of FK506 on cell growth under high Ca^{2+} condition, respectively. Light gray boxes indicates *cls* mutants whose Ca^{2+} sensitivity were unaltered in the presence or absence of 0.4 μg/ml FK506.

Fig. S6

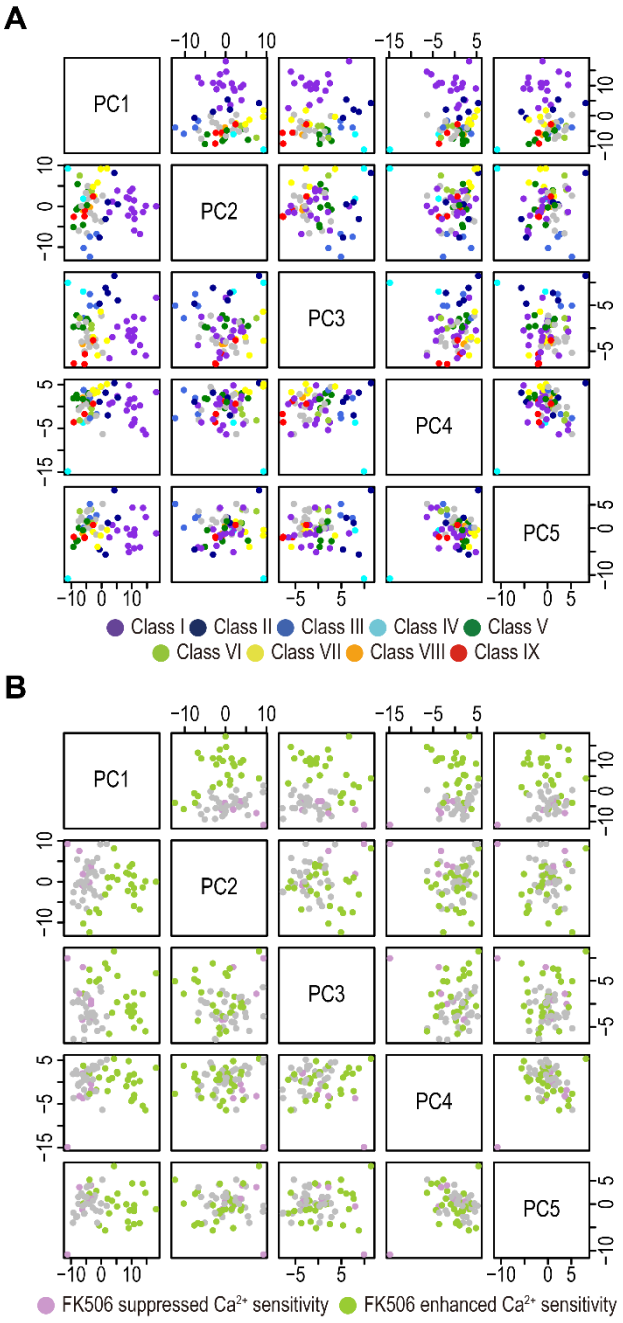

Figure S6. Pair plots of principal component scores of the Ca^{2+}-*cls* interaction profiles. Distribution of principal component scores for PC1 to PC5 of the 62 Ca^{2+}-*cls* interaction profiles. **A.** Colors reflect the nine detected classes in Fig. 5. **B.** Purple and green circles indicate *cls* mutants showing FK506-suppressed or -enhanced Ca^{2+} sensitivity, each of which was classified into ether of the nine classes, and the effects of FK506 were consistent within the class. All *cls* mutants classified in class I, II, and III showed FK506-enhanced Ca^{2+} sensitivity whereas all *cls* mutants classified in class IV, VI, and VIII showed FK-506 suppressed Ca^{2+} sensitivity.

Fig. S7

A

PC1	Propotion of variance	Parameter ID	Description	Loading (2nd PCA)	*P* value	Loading (1st PCA)	Z_{wt}	Morphological feature
PC1a	0.24	D104_A1B	Distance between nuclear gravity center and mother tip	-0.83	6.86E-33	0.69	-4.02	Mother cell size
		D135_A	Distance between nuclear brightest point and cell center	-0.81	3.46E-29	0.81	-1.93	
		D117_A	Distance between nuclear gravity center and cell center	-0.80	9.91E-29	0.80	-2.01	
		D129_A1B	Distance between nuclear brightest point and mother tip	-0.79	9.44E-27	0.64	-3.90	
		C11-1_C	Mother cell size	-0.78	1.07E-25	0.68	-0.26	
		D142_A1B	Distance between nuclear brightest point and mother hip	-0.77	3.84E-25	0.63	-3.74	
		C12-1_C	Mother cell outline length	-0.76	1.72E-24	0.69	-1.16	
		C103_A1B	Long axis length in mother	-0.75	2.12E-23	0.70	-2.10	
		D118_A1B	Distance between nuclear gravity center and mother center	-0.75	2.74E-23	0.80	-4.84	
		D148_A	Relative distance of nuclear brightest point to cell center	-0.73	8.31E-22	0.84	-2.00	
		D126_A1B	Distance between nuclear gravity center and mother hip	-0.73	1.65E-21	0.65	-3.80	
		C128_C	Distance between middle point of neck and mother hip	-0.73	2.69E-21	0.63	-1.29	
		D147_A	Relative distance of nuclear gravity center to cell center	-0.72	1.60E-20	0.78	-2.12	
PC1b	0.10	A107_A1B	Actin c ratio	0.83	1.65E-32	0.69	0.73	Cells with actin loclization
		A116	actin c ratio to budded cells	0.81	5.21E-29	0.62	0.34	around the tip of the bud
		C117_A1B	Cell outline ratio	-0.77	1.34E-25	-0.64	-0.71	
		C118_A1B	Cell size ratio	-0.77	5.04E-25	-0.64	-0.61	
PC1c	0.08	D125_C	Distance between nuclear gravity center in mother and mother hip	0.75	6.43E-23	0.75	-2.67	Nuclear position
		D141_C	Distance between nuclear brightest point in mother and mother hip	0.74	3.91E-22	0.76	-2.36	
PC1d	0.07	A117	actin d ratio to budded cells	0.80	5.63E-28	0.75	0.94	Cells with actin spreading
		A108_A1B	Actin d ratio	0.78	3.26E-26	0.78	0.51	over the entire bud
PC1e	0.07	CCV12-1_C	Noise of C12-1 C	0.73	1.07E-21	0.73	4.78	Noise of cell size
		CCV11-1_C	Noise of C11-1 C	0.72	4.96E-21	0.68	3.70	

PC2	Propotion of variance	Parameter ID	Description	Loading (2nd PCA)	*P* value	Loading (1st PCA)	Z_{wt}	Morphological feature
PC2a	0.35	D114_A1B	Ratio of D110 to C128	-0.90	1.02E-44	0.63	4.35	Nuclear position
		D107_A1B	Ratio of D104 to C103	0.89	3.58E-42	0.70	-4.35	
		D132_A1B	Distance between nuclear brightest point and middle point of neck	-0.86	4.23E-37	0.66	2.33	
PC2b	0.21	C122	large bud ratio	-0.88	1.69E-40	-0.61	1.99	Large bud ratio
		C125_A1B	Large bud ratio	-0.76	1.18E-24	-0.61	0.69	
PC2c	0.16	C114_A1B	Bud axis ratio	-0.78	6.07E-26	0.66	-4.36	Roundness of the bud

B

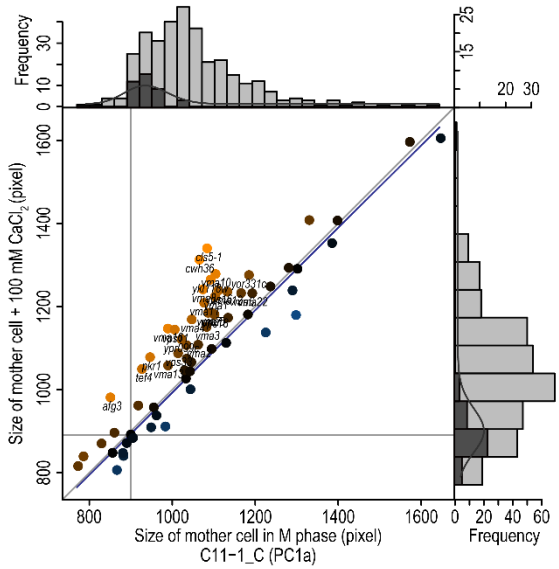

C

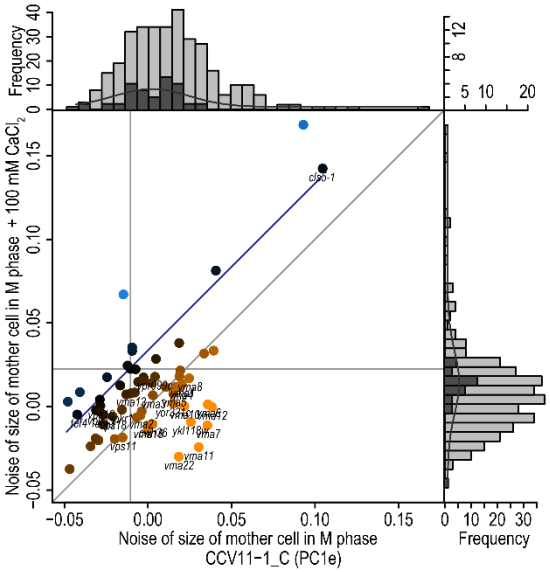

Continued on following page

Fig. S7—Continued

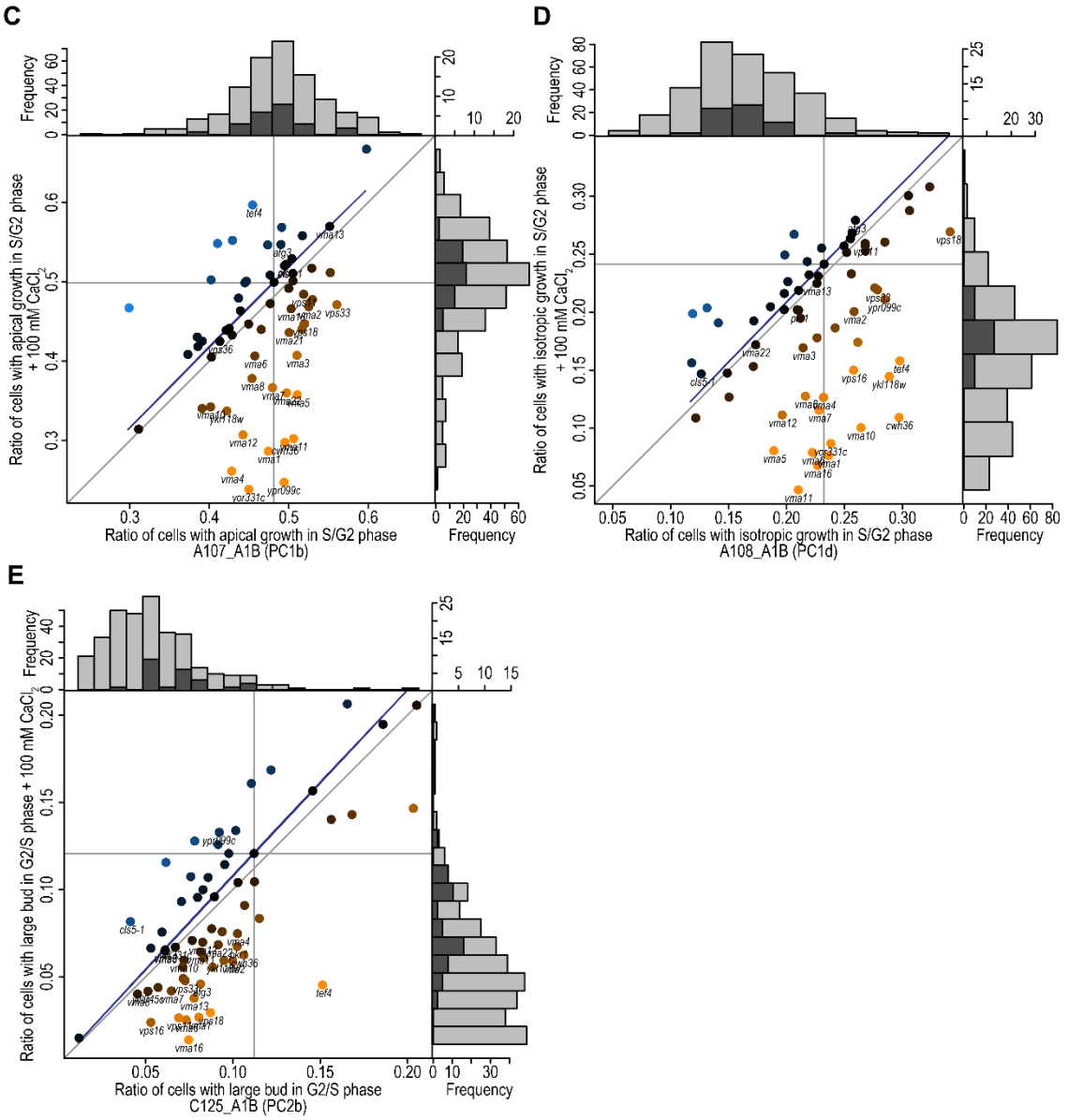

Figure S7. Representative morphological features that correlated with the first and second principal components of the Ca^{2+}-*cls* interaction profiles. A. Parameter descriptions for the PCs representing independent morphological features that highly correlated with PC1 and PC2, respectively. Red and green indicate positive and negative values of Z_{wt} scores, respectively, which indicate increases and decreases of parameter values of the wild-type by Ca^{2+} treatment. Orange bars highlight parameters represented in Fig. S7 B to E. **B–E.** Representative parameters that highly correlated with PC1a (**B**), PC1e (**C**), PC1b (**D**), and PC1d (**E**). Class I, II, and III *cls* mutants were displayed in each graph. In each parameter, parameter values of wild-type cells and the 62 *cls* mutants in the absence (x axis) or presence (y axis) of 100 mM $CaCl_2$ were plotted. Orange or blue circle indicate positive or negative Ca^{2+}-*cls* interaction of corresponding *cls* mutant, respectively. Vertical and horizontal light gray lines indicate parameter value of the wild-type cell in the absence or presence of 100 mM $CaCl_2$. A navy curve traces typical parameter value of each *cls* mutant expected from Ca^{2+}-induced parameter change of the wild-type. Dark and light gray histograms indicate distribution of the wild-type and the *cls* mutants in the absence (upper) or presence (light) of 100 mM $CaCl_2$. Dark gray curve on the histograms traces probability densities of the wild-type cells in each condition.

Fig. S8

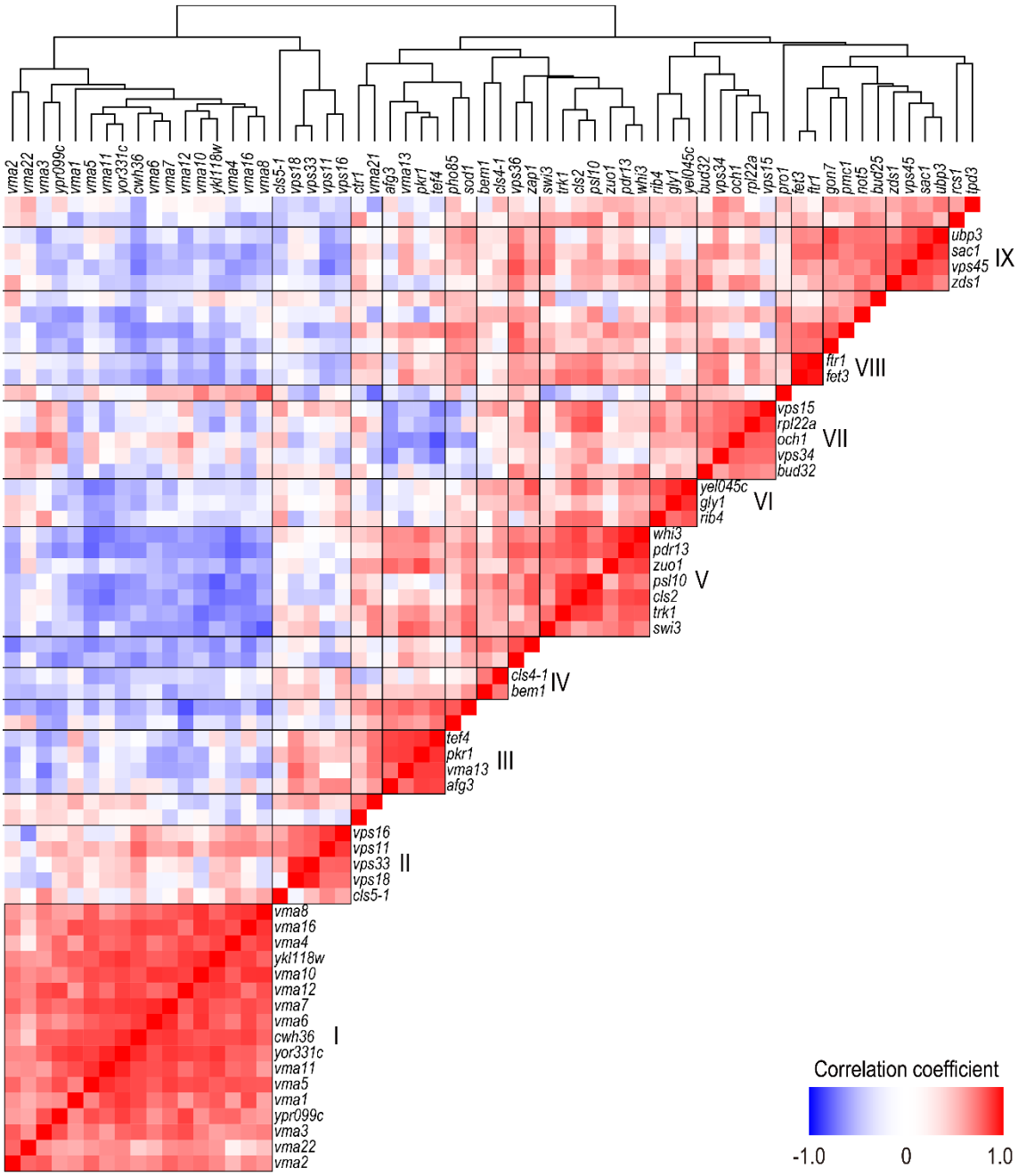

Figure S8. A correlation matrix of the Ca^{2+}-*cls* interaction profiles. Similarities of the Ca^{2+}-*cls* interaction profiles were measured for all gene pairs by calculating Pearson correlation coefficients (PCCs) form the Ca^{2+}-*cls* interaction matrix. Red and blue boxes indicate positive or negative correlations of corresponding gene pairs. Black boxes and roman numbers (I–IX) correspond to the detected nine classes in Fig. 5.

Chapter II

Profilin is required for Ca^{2+} homeostasis and Ca^{2+} modulated bud formation in yeast

Introduction

Among available *cls* mutants, the *cls5* mutant attracted my attention because it is specifically sensitive to Ca^{2+}, has elevated Ca^{2+} content (Ohya *et al.*, 1986b), and shows altered cell morphology in the presence of high Ca^{2+}. Previous genetic analyses demonstrated that the *CLS5* is identical to the profilin-encoding-gene *PFY1* (Takita, 1997). Profilin is a highly conserved, small (15 kDa) soluble protein, and known to play important roles in actin organization in all eukaryotic cells (Haarer *et al.*, 1990). In the budding yeast *S. cerevisiae*, profilin is involved in various cellular functions such as bud formation, cytokinesis, spore germination, and intracellular transport (Haarer *et al.*, 1990, 1996; Marcoux *et al.*, 1998) via binding to several ligands including actin (Haarer and Brown, 1990), phosphoinositides (Ostrander *et al.*, 1995), and polyproline (Imamura *et al.*, 1997). However, how profilin is involved in Ca^{2+}-regulatory mechanisms remained to be clarified. The *CLS5* gene showed the 7^{th} most Ca^{2+}-*cls* interactions (Fig. 6 A) and classified into class II (Fig. 5) in the previous chapter, implying that yeast profilin plays important roles in cell proliferation under high Ca^{2+} condition. Although all of class II *cls* mutants showed elevated intracellular Ca^{2+} content, however, it remains unknown whether there is causal relationship between impairment of Ca^{2+} homeostasis and altered cell morphology of

cls5 mutant cells under high Ca^{2+} condition. These observations prompted me to investigate the mechanism of Ca^{2+} sensitivity induced by the *cls5* mutation.

In this chapter I first identified the gene product that physically interacted with Pfy1p using a protein interaction database (*Saccharomyces* Genome Database). Second, I measured intracellular Ca^{2+} content of *cls5* and other Ca^{2+}-sensitive mutants whose responsible genes encode proteins that physically interact with Pfy1p. Third, I examined Ca^{2+}-*cls* interaction profiles of the same Ca^{2+}-sensitive mutants. Through the above analyses, surprisingly, yeast profilin was shown to function in two independent functions in response to exposure in high concentration of Ca^{2+}. One is, through intracellular Ca^{2+} content measurement, to maintain Ca^{2+} homeostasis of the cell, which function cooperatively with Bem1p, Bni1p/Bnr1p, Rho1p, and Cla4p. The other is, through morphological analysis, the function in Ca^{2+}-modulated bud formation in coordination with Bem1p and Cdc24p.

Results

Characteristic Ca^{2+}-related phenotypes of the *cls5* mutant

I first examined the effect of profilin function on intracellular Ca^{2+} pools. The total Ca^{2+} pool was dramatically increased to a 5.8-fold higher level than that in wild-type cells in *pfy1Δ* cells, while that in *cls5-1* cells increased 5.4-fold (Fig. 9), in agreement with previous results (Takita, 1997). Both exchangeable and non-exchangeable pools were higher in *pfy1Δ* and *cls5-1* cells than in wild-type cells, indicating that the loss of profilin function causes an overall elevation

of intracellular Ca^{2+}pools. Additionally, I found that *cls5-1* cells changed cell morphology in the presence of high extracellular Ca^{2+}. Although previous studies reported that *pfy1* mutant cells have altered cell morphology even under normal conditions, in the presence of high concentrations of Ca^{2+}, *cls5-1* cells appeared to be rounder and larger (Fig. S9). To describe morphological Ca^{2+}-response altered by the *cls5* mutation, I quantified the cellular morphology of *cls5-1* cells (YOC989) grown under two culture conditions (YPD medium supplemented with or without 100 mM $CaCl_2$). At least 200 cells were analyzed per culture to quantify 501 morphological parameters. In 88 parameters, Ca^{2+}-*cls* interactions were significantly detected ($P < 0.05$, Wald test). Additionally, to describe morphological features of Ca^{2+}-*cls* interactions observed in *cls5-1* cells, I applied PCA to 88 detected parameters as described previously (Ohnuki *et al.*, 2012). The 88 parameters were explained by 9 PCs at 70% of the CCR. Parameters significantly correlated with each PC ($P < 1 \times 10^{-5}$, *t* test) were listed in Fig. S10. Based on Fig. S10, I illustrated the Ca^{2+}-dependent morphological changes of *cls5-1* cells (Fig. 10). Under 100 mM $CaCl_2$, *cls5-1* cells significantly increased in mother cell size at G1, S/G2 and M phase of the cell cycle than expected from the morphological changes of the wild-type cell. I found that *cls5-1* cells significantly increased in nuclear size at S/G2 phase than expected under the high Ca^{2+} condition. Correspondingly, the ratio of G1 cells and M cells in the population significantly increased and decreased, respectively (Fig. 10). The *cls5-1* cells also significantly increased in the actin region, phenotypic noise in actin patches, suggesting that actin patches were delocalized

by Ca^{2+} treatment. These results indicated that *cls5-1* cells showed altered morphological Ca^{2+}-response at various cellular stages in the presence of high concentrations of Ca^{2+}.

Several mutants of proteins that physically interact with profilin show Ca^{2+} sensitivity

Profilin is a small soluble protein that binds to various ligands. If interactions with those proteins are important for Ca^{2+} tolerance, a mutation or disruption of those genes will cause Ca^{2+} sensitivity. According to the *Saccharomyces* Genome Database, I investigated Ca^{2+}-sensitivity of all mutants of profilin-physically-interacting proteins except for the *nab2* mutant. Mutants analyzed for Ca^{2+} sensitivity are described in Table S2.

I found that the *bni1Δ* mutant showed no visible colony at a dilution of 10^2 cells in the presence of 300 mM $CaCl_2$ (Fig. 11) and exhibited a Ca^{2+}-sensitive phenotype. I also analyzed the Ca^{2+} sensitivity of the *bni1 bnr1* double mutant. As the complete *bni1Δ bnr1Δ* double mutant leads to a synthetic lethal phenotype (Kamei *et al.*, 1998), I used a viable temperature-sensitive *bni1 bnr1* mutant in which *BNI1* and *BNR1* were partially disrupted (Imamura *et al.*, 1997). The *bni1 bnr1* cells showed greater sensitivity than *bni1Δ* cells (Fig. 11). I also examined whether Bni1p–Rho1p binding is required for Ca^{2+} tolerance. Rho1-2p was shown to not bind to Bni1p using the two-hybrid system (Qadota *et al.*, unpublished data) and the *rho1-2* mutant showed Ca^{2+}-sensitivity just like the *bni1Δ* mutant (Fig. 11). These results suggested that Bni1p/Bnr1p and Rho1p function is important for Ca^{2+} tolerance.

I found that disruption of Bem1p exhibited Ca^{2+} sensitivity in the presence of 300 mM $CaCl_2$ (Fig. 11). Additionally, Cdc24p binds directly to Bem1p (Bose *et al.*, 2001), and the mutant

allele of a Ca^{2+}-sensitive mutant (*cls4-1*) is located in the *CDC24* gene (Ohya *et al.*, 1986a). I also found that disruption of Cla4p, which also binds directly to Bem1p (Bose *et al.*, 2001), showed Ca^{2+} sensitivity (Fig. 11). Moreover, mutants of these proteins (Bni1p, Bem1p, Rho1p, Cdc24p, Cla4p) were specifically sensitive to Ca^{2+} and not to other cations (Mg^{2+}, Mn^{2+}, and Zn^{2+}) or osmotic pressure, just like *cls5-1* (data not shown). These results suggested that as with profilin, the profilin-physically-interacting proteins are involved in intracellular Ca^{2+}-related pathways.

As profilin plays an important role in actin organization, I expected an actin–profilin interaction to be required for Ca^{2+} tolerance. Since the actin-encoding gene (*ACT1*) is essential for cell growth, I examined the Ca^{2+} sensitivities of specific actin mutants that disrupt actin–profilin interactions (Amberg *et al.*, 1995). Two alleles, *act1-111* and *act1-129*, with lowered binding activity to profilin were still able to grow on YPD supplemented with 300 mM $CaCl_2$ (Fig. 12). Additionally, wild-type cells treated with the actin polymerization inhibitor Latrunculin-A also did not show Ca^{2+} sensitivity (Fig. S11). These results suggest that an actin–profilin interaction is not important for Ca^{2+} tolerance.

Profilin may regulate Ca^{2+} influx via actin-mediated endocytosis because profilin is somehow involved in endocytosis (Robertson *et al.*, 2009). To test whether endocytosis is required for Ca^{2+} homeostasis, I examined the Ca^{2+} sensitivity of 34 endocytic mutants (Table S3). No mutants showed Ca^{2+} sensitivity, suggesting that the endocytosis is not directly related to Ca^{2+} homeostasis.

Bni1p/Bnr1p, Bem1p, Rho1p, and Cla4p are involved in maintaining Ca^{2+} homeostasis

To examine whether profilin-physically-interacting proteins are involved in the maintenance of Ca^{2+} homeostasis, I quantified intracellular Ca^{2+} pools in *bni1Δ*, *bem1Δ*, *rho1-2*, *cls4-1*, and *cla4Δ* cells. Remarkably, the total Ca^{2+} pool in *bni1Δ*, *bem1Δ*, *rho1-2*, and *cla4Δ* mutant cells was higher than that in wild-type cells (increased to 1.7-fold, 3.1-fold, 4.5-fold, and 2.9-fold, respectively) as in *cls5-1* cells (Fig. 9). Both exchangeable and non-exchangeable pools were higher in *bni1Δ*, *bem1Δ*, *rho1-2*, and *cla4Δ* mutant cells than in wild-type cells, indicating that the loss of Bni1p, Bem1p, Rho1p, and Cla4p function also leads to an overall elevation of intracellular Ca^{2+}pools. The total Ca^{2+} pool in the *bni1 bnr1* cells was also increased 4.2-fold compared to the wild type (data not shown). Conversely, the total Ca^{2+} pool in *cls4-1* cells was comparable to that in wild-type cells (1.1-fold). These results indicate that the loss of profilin, Bni1p/Bnr1p, Bem1p, Rho1p, and Cla4p function leads to elevated intracellular Ca^{2+}, resulting in the impairment of Ca^{2+} homeostasis.

Ca^{2+}-*cls* interaction profile in *cls5-1* cells is similar to that of *cls4-1* and *bem1Δ* cells, rather than other mutants

To explore which profilin-physically-interacting proteins are required for cell morphogenesis under high concentrations of Ca^{2+}, I quantified cell morphology in the mutants of profilin-physically-interacting proteins (*bni1Δ*, *bem1Δ*, *rho1-2*, *cls4-1*, and *cla4Δ*) between two culture conditions (YPD medium supplemented with or without 100 mM $CaCl_2$). Typical images after staining the cell wall, actin, and nuclear DNA are shown in Fig. S12. Although *bni1Δ*, *rho1-2*, *bem1Δ*, and *cla4Δ* cells failed to grow in the presence of 300 mM, slight morphological changes

occurred even in the presence of 100 mM $CaCl_2$ (Fig. S9). I applied hierarchical cluster analysis based on Pearson product-moment correlation to the Ca^{2+}-*cls* interaction profiles of *cls5-1* (YOC989) and profilin-physically-interacting Ca^{2+}-sensitive mutants (Fig. 13 A). The Ca^{2+}-*cls* interaction profiles in *cls5-1*, *cls4-1*, and *bem1Δ* cells showed similar color patterns, suggesting that *cls5-1*, *cls4-1*, and *bem1Δ* cells shared similar morphological Ca^{2+}-responses distinct from the other mutants. To verify the statistical significance, I applied the multiscale bootstrap technique (Suzuki and Shimodaira, 2006). *cls5-1*, *cls4-1*, and *bem1Δ* mutants were robustly clustered at *P* values > 0.95 (Fig. 13 A, magenta rectangle), indicating that loss of profilin, Bem1p, and Cdc24p function led to similar Ca^{2+}-*cls* interactions in the presence of high Ca^{2+}. I further investigated the characteristic Ca^{2+}-*cls* interactions among *cls5-1*, *cls4-1*, and *bem1Δ* by applying principal component analysis to the Ca^{2+}-*cls* interaction profiles. I found that interaction profiles of *cls5-1*, *cls4-1*, and *bem1Δ* mutants were distinguishable from others in the PC1 (Fig. 13 B). The *cls5-1*, *cls4-1*, and *bem1Δ* showed decreased PC1 scores (Fig. 13 B). Subsequently, seven representative morphological features accompanied with the PC1 (PC1a–g) were identified (Fig. S13). Of note, PC1a included the whole cell size of G1 cells, in which parameter values in *cls5-1*, *cls4-1*, and *bem1Δ* mutant cells were significantly increased (Fig. 14 A), indicating that one of main Ca^{2+}-dependent morphological change among the three mutants was an increase in G1 cell size. In addition, PC1b included the ratio of unbudded cells (C119) as well as the total length of the actin patch link in G1 cells (A120_A) (Fig. S13). Over 90% of *cls4-1* cells were unbudded in the presence of high concentrations of Ca^{2+}, and about 80% of *cls5-1* and *bem1Δ*

mutant cells ceased to bud after Ca^{2+} treatment (Fig. 14 B). These results suggest that *cls5-1*, *cls4-1*, and *bem1Δ* mutants were unable to form buds in the presence of high concentrations of Ca^{2+}. Likewise, actin patches in the three mutants were delocalized in the presence of high concentrations of Ca^{2+} (A120_A; Fig. 14 C). Taken together, these Ca^{2+}-*cls* interactions suggested that the *cls5-1*, *cls4-1*, and *bem1Δ* mutants were not able to establish adequate cell polarity, resulting in defects in bud formation under high extracellular Ca^{2+}.

To test the possibility that profilin regulates localization of Cdc24p, I observed GFP-fused Cdc24p in *cls5-1* cells. GFP-fused Cdc24p was dramatically delocalized in unbudded cells of the *cls5-1* mutant cultivated in YPD. This result implied that profilin function decreased in *cls5-1* even under the normal condition. I also found that polarized localization of Cdc24p in unbudded cells notably decreased in *cls5-1* after treatment with 100 mM $CaCl_2$ (Fig. S14), suggesting that profilin regulates localization of Cdc24p in a Ca^{2+}-dependent manner.

Discussion

In this chapter, I aimed to reveal how *cls5-1* mutation (Ohya *et al.*, 1986b), which is mapped in the open reading frame of the profiling-encoding gene *PFY1* (Takita, 1997), induce Ca^{2+}-sensitive phenotype. Since physically interacting proteins often share common functions, I extended research to analysis of profilin-physically-interacting proteins. Genetic studies revealed that profilin, Bem1p, Bni1p/Bnr1p, Rho1p, and Cla4p function in the maintenance of Ca^{2+} homeostasis. I also found that profilin, Bem1p, and Cdc24p play roles in Ca^{2+}-modulated bud

formation. Thus, profilin functions in both the maintenance of Ca^{2+} homeostasis and Ca^{2+}-modulated bud formation in an independent manner with overlapping but distinct members of interacting proteins (Fig. 15). Profilin and Bem1p were required for both Ca^{2+} homeostasis and Ca^{2+}-modulated bud formation, suggesting that the profilin–Bem1p interaction plays a role in both Ca^{2+} regulatory mechanisms.

How profilin regulates intracellular Ca^{2+} homeostasis

My results indicated that impairment of profilin results in the elevation of intracellular Ca^{2+} levels. In *cls5-1*, Ca^{2+} accumulated both in exchangeable and non-exchangeable pools. Because most of the non-exchangeable pools reside in the vacuole, and the exchangeable pools are located in other organelles, I proposed that excess Ca^{2+} accumulates not in specific organelles but throughout *cls5-1* cells. My implication is that profilin may regulate Ca^{2+} influx in the plasma membrane.

One possibility was that profilin might regulate Ca^{2+} influx via actin-mediated endocytosis, which is highly organized in yeast (Robertson *et al.*, 2009). However, no endocytic mutants showed Ca^{2+} sensitivity, suggesting that endocytosis was not required for Ca^{2+} homeostasis. Consistent with this observation, yeast profilin is not required for generation of Myo5p-induced actin foci *in vitro* (Idrissi *et al.*, 2002). They also showed that profilin is not essential for endocytic uptake *in vivo*. These facts support my argument; however, the possibility still remains that profilin downregulates actin-mediated endocytosis in the presence of high Ca^{2+}, although it is not required for endocytosis under normal conditions.

Another possibility is that profilin may regulate Ca^{2+} channels in the plasma membrane to maintain intracellular Ca^{2+} homeostasis. Under growth conditions, the majority of profilin localizes to the plasma membrane through interaction with phospholipid PIP_2, which is exclusively localized to the plasma membrane (Patton and Lester, 1992; Ostrander *et al.*, 1995). Although no report has demonstrated direct linkage between profilin and Ca^{2+} channels in the plasma membrane, investigating the physical interaction between them may be warranted.

Actin and Ca^{2+} tolerance

Whether actin organization plays a role in Ca^{2+} tolerance is a point of interest. Profilin was originally identified as an actin-binding protein required for actin organization and cell polarity. In this study, I found that actin patches in G1 cells were significantly delocalized in the *cls5-1* mutant in the presence of high concentrations of Ca^{2+}, supporting the possibility that actin delocalization may lead to Ca^{2+}-sensitive phenotypes. My result that *act1-111* and *act1-129* with lower binding affinity to profilin are not sensitive to high concentrations of Ca^{2+} contradicts this idea. However, note that the binding affinity is estimated only based on two-hybrid data. Thus, presently, I cannot conclude whether actin organization itself is important for Ca^{2+} tolerance. I also found that *act1-132* with normal binding affinity to profilin showed Ca^{2+} sensitivity in the presence of 300 mM $CaCl_2$. The morphology of *act1-132* did not change after treatment with 100 mM $CaCl_2$ (data not shown), suggesting that some functions of actin other than morphogenesis may be required for Ca^{2+} tolerance. Further study is required to reveal actin functions in Ca^{2+}-related pathways.

Possible mechanism of Ca^{2+}-induced morphological changes in *cls5-1*, *cls4-1*, and *bem1Δ* cells

My quantitative morphological analysis revealed that the *cls5-1*, *cls4-1*, and *bem1Δ* mutant cells had larger G1 cells and increased ratios of G1 cells in the presence of Ca^{2+}. One possible explanation for the Ca^{2+}-induced morphological changes in these mutant cells is that Cdc24p was not able to localize to the proper nascent bud site in the presence of high Ca^{2+}. By using temperature-sensitive *cdc24* mutants, a previous study showed that the Bem1p–Cdc24p interaction is required for the polarized localization of Cdc24p (Fujimura-Kamada *et al.*, 2012). Another group reported that the physical interaction between Cdc24p and Bem1p is inhibited by 2 mM $CaCl_2$ *in vitro* (Zheng *et al.*, 1995). It was of interest that in the *cls4-1* mutant the 1615th amino acid residue, glycine (Gly) of Cdc24p, is changed to serine (Ser) (Miyamoto *et al.*, 1991). The domain around the Gly residue is the PH domain, which serves as a membrane targeting signal (Toenjes *et al.*, 1999; Lemmon, 2008), and a putative Ca^{2+}-binding site (residues 649–658) exist in this domain (Miyamoto *et al.*, 1991). Additionally, another putative Ca^{2+}-binding site (residues 820–831) (Miyamoto *et al.*, 1987) exists in the PB1 domain of Cdc24p, which is required for binding to Bem1p. Considering these findings as a whole, I speculate that intracellular Ca^{2+} regulates two functions of Cdc24p, membrane localization and interaction with Bem1p, by binding directly to the Cdc24p molecule. Therefore, I reasoned that profilin may be involved in the proper localization of Cdc24p, particularly at the G1 phase in two ways, by maintaining intracellular Ca^{2+} concentrations and interacting with Cdc24p via Bem1p. To test the

hypothesis, I observed the localization of Cdc24p in *cls5-1* cells at the G1 stage. I found that polarized localization of Cdc24p in unbudded cells decreased in *cls5-1* after treatment with 100 mM $CaCl_2$, supporting my notion. Further study is required to elucidate the detailed mechanisms of profilin in the maintenance of Ca^{2+} homeostasis and Ca^{2+}-modulated bud formation.

Tables

Table S2. Ca^{2+} sensitivity of the wild type and mutants of profilin-physically-binding proteins.

Wild-type	YPD	YPD + 100 mM $CaCl_2$	YPD + 300 mM $CaCl_2$		Source
YPH499	++	++	++		1
his3Δ	++	++	++		2
OHNY1	++	++	++		3
Mutant of profilin-binding proteins					
Mutant	YPD	YPD + 100 mM $CaCl_2$	YPD + 300 mM $CaCl_2$	Experimental evidence	Source
act1-101	++	++	±	Two-hybrid, Co-IP, Reconstituted complex	4
act1-111	++	++	++	Two-hybrid, Co-IP, Reconstituted complex	4
act1-113	++	++	++	Two-hybrid, Co-IP, Reconstituted complex	4
act1-120	++	++	++	Two-hybrid, Co-IP, Reconstituted complex	4
act1-125	++	++	++	Two-hybrid, Co-IP, Reconstituted complex	4
act1-129	++	++	++	Two-hybrid, Co-IP, Reconstituted complex	4
act1-132	++	++	–	Two-hybrid, Co-IP, Reconstituted complex	4
bem1Δ	++	++	–	Co-fractionation	2
bni1Δ	++	++	±	Two-hybrid	2
bni1Δ bnr1Δ	++	+	–	Two-hybrid	5
bnr1Δ	++	++	++	Two-hybrid	2
slf1Δ	++	++	++	Co-IP	2
sro9Δ	++	++	++	Co-IP	2
srv2Δ	++	++	++	Two-hybrid, Co-IP	2
Mutant of Bni1p- and Bem1p-binding proteins					
Mutant	YPD	YPD + 100 mM $CaCl_2$	YPD + 300 mM $CaCl_2$	Experimental evidence	Source
afi1Δ	++	++	++	Two-hybrid	2
aim4Δ	++	++	++	Co-IP	2
arp2-14	++	++	++	Co-IP	6
axl2Δ	++	++	++	Co-IP	2
bck1Δ	++	++	++	Protein-peptide	2
boi1Δ	++	++	++	Two-hybrid, Co-IP, Protein-peptide	2
boi2Δ	++	++	++	Two-hybrid, Co-IP, Protein-peptide	2

continued on following page

Table S2—continued

Mutant	YPD	YPD + 100 mM $CaCl_2$	YPD + 300 mM $CaCl_2$	Experimental evidence	Source
bud6Δ	++	++	++	Two-hybrid	2
caf130Δ	++	++	++	Two-hybrid	2
cdc14-8	++	++	++	Co-IP	6
cdc20-1	++	++	±	Reconstituted complex	6
cdc20-3	++	++	++	Reconstituted complex	6
cdc28-1	++	++	++	Biochemical activity	6
cdc28-13	++	++	++	Biochemical activity	6
cdc28-14	++	++	++	Biochemical activity	6
cdc28-4	++	++	++	Biochemical activity	6
cdc28-td	++	++	++	Biochemical activity	6
cdc42-1	++	++	++	Two-hybrid, Co-IP, Reconstituted complex	6
cdc48-1	++	++	++	Co-IP	6
cdc48-2	++	++	++	Co-IP	6
cdc48-3	++	++	++	Co-IP	6
cdc48-4601	++	++	++	Co-IP	6
cdc48-9	++	++	++	Co-IP	6
cla4Δ	++	++	–	Two-hybrid, Co-IP, Protein-peptide	2
cls4-1	++	–	–	Two-hybrid, Co-IP, Reconstituted complex	7
cdc24-1	++	++	++	Two-hybrid, Co-IP, Reconstituted complex	6
cof1-5	++	++	++	Co-fractionation	6
cof1-8	++	++	++	Co-fractionation	6
cyc8Δ	++	++	±	Two-hybrid	2
dss1Δ	++	++	++	Two-hybrid	2
dyn1Δ	++	++	++	Two-hybrid	2
est2Δ	±	±	±	Two-hybrid	2
exo70-29/37	++	++	++	Co-purification	6
exo70-38	++	++	++	Co-purification	6
exo84-102	++	++	++	Co-purification	6
fal1-1	++	++	++	Co-IP	6
far1Δ	++	++	++	Two-hybrid, Co-IP, Reconstituted complex	2
fpk1Δ	++	++	++	Two-hybrid	2
fus1Δ	++	++	++	Two-hybrid	2
fus3Δ	++	++	++	Co-IP, Biochemical activity	2
hof1Δ	++	++	++	Two-hybrid	2
hsp104Δ	++	++	++	Co-localization	2

continued on following page

Table S2—continued

Mutant	YPD	YPD + 100 mM $CaCl_2$	YPD + 300 mM $CaCl_2$	Experimental evidence	Source
kel2Δ	++	++	++	PCA	2
ksp1Δ	++	++	++	Biochemical activity	2
las17-1	++	++	++	Co-IP, Co-fractionation	6
las17-13	++	++	++	Co-IP, Co-fractionation	6
las17-14	++	++	++	Co-IP, Co-fractionation	6
ldb16Δ	++	++	++	Two-hybrid	2
ldb18Δ	++	++	++	Two-hybrid	2
met31Δ	++	++	++	Two-hybrid	2
mps1-1	++	++	++	Two-hybrid, Co-IP	6
mps1-3796	++	++	++	Two-hybrid, Co-IP	6
mps1-417	++	++	++	Two-hybrid, Co-IP	6
mps1-6	++	++	++	Two-hybrid, Co-IP	6
mrps35Δ	++	++	++	Co-IP	2
msb1Δ	++	++	++	Two-hybrid	2
msb3Δ	++	++	++	Two-hybrid, Reconstituted complex	2
msb4Δ	++	++	++	Two-hybrid, Reconstituted complex	2
mth1Δ	++	++	++	Two-hybrid	2
myo3Δ	++	++	++	Co-IP	2
myo5Δ	++	++	++	Two-hybrid	2
nfu1Δ	++	++	++	Two-hybrid	2
num1Δ	++	++	++	Co-IP	2
nyv1Δ	++	++	++	Co-fractionation	2
pbs2Δ	++	++	–	Protein-peptide	2
pdr3Δ	++	++	++	Two-hybrid	2
pho8Δ	++	++	++	Co-fractionation	2
prk1Δ	++	++	++	Biochemical activity	2
rga2Δ	++	++	++	Co-IP	2
rho1-2	++	++	±	Two-hybrid, Co-fractionation	8
rho1-3	++	++	±	Two-hybrid, Co-fractionation	8
rho1-4	++	++	±	Two-hybrid, Co-fractionation	8
rho1-5	++	++	±	Two-hybrid, Co-fractionation	8
rho3Ser228	++	++	++	Two-hybrid	6
rkr1Δ	++	++	++	Two-hybrid	2
rsr1Δ	++	++	++	Reconstituted complex	2
sec10-2	++	++	++	Co-purification, Reconstituted complex	6

continued on following page

Table S2—continued

Mutant	YPD	YPD + 100 mM $CaCl_2$	YPD + 300 mM $CaCl_2$	Experimental evidence	Source
sec15-1	++	++	++	Two-hybrid, Co-IP, Reconstituted complex	6
sec17-1	++	++	++	Co-fractionation	6
sec18-1	++	++	++	Co-fractionation	6
sec3-2	++	++	++	Co-purification	6
sec5-24	++	++	++	Co-purification, Reconstituted complex, PCA	6
sec6-4	++	++	++	Co-purification	6
sec8-6	++	++	++	Co-IP, Co-pUrification	6
sec8-9	++	++	++	Co-IP, Co-pUrification	6
sfk1Δ	++	++	++	PCA	2
sgm1Δ	++	++	++	Two-hybrid	2
skm1Δ	++	++	++	Protein-peptide	2
snc1Δ	++	++	++	Co-IP	2
snc2Δ	++	++	++	Co-IP	2
spa2Δ	++	++	++	Two-hybrid, Reconstituted complex	2
spt15-I143N	++	++	++	Co-IP	6
spt15-P65S	++	++	++	Co-IP	6
ssn8Δ	++	++	++	Two-hybrid	2
sso1Δ	++	++	++	Co-IP	2
sso2Δ	++	++	++	Co-IP	2
std1Δ	++	++	++	Two-hybrid	2
ste11Δ	++	++	++	Co-IP	2
ste20Δ	++	++	++	Two-hybrid, Co-IP, Reconstituted complex	2
ste5Δ	++	++	++	Two-hybrid, Co-IP	2
ste7Δ	++	++	++	Co-IP	2
swe1Δ	++	++	++	Two-hybrid	2
tcb3Δ	++	++	++	Co-IP	2
urn1Δ	++	++	++	Two-hybrid	2
vac8Δ	++	++	++	Co-fractionation	2
vam3Δ	++	++	++	Co-fractionation	2
vam6Δ	++	++	±	Co-fractionation	2
vam7Δ	++	++	±	Co-fractionation	2
vba5Δ	++	++	++	Two-hybrid	2
vps16Δ	++	–	–	Co-fractionation	2
vps1Δ	++	++	++	Co-fractionation	2
vps33Δ	++	–	–	Co-fractionation	2

continued on following page

Table S2—continued

Mutant	YPD	YPD + 100 mM $CaCl_2$	YPD + 300 mM $CaCl_2$	Experimental evidence	Source
vti1-1	++	++	++	Co-fractionation	6
vti1-11	++	++	++	Co-fractionation	6
ydr306cΔ	++	++	++	Two-hybrid	2
yel043wΔ	++	++	++	Two-hybrid	2
ykt6Δ	++	++	++	Co-fractionation	2
ynr071cΔ	++	++	++	Two-hybrid	2
ypr1Δ	++	++	++	Two-hybrid	2
ypt7Δ	++	++	+	Co-fractionation	2
zds2Δ	++	++	++	Co-IP	2

Cells were incubated at 25ºC for 4 days. ++, normal growth; +, slow growth; ±, very slow growth; –, no growth. Physical interaction data were obtained from the Saccharomyces Genome Database (http://www.yeastgenome.org/) on 2012/6/16. Co-IP: co-immunoprecipitation, PCA: protein fragment complementation assay (PCA is "principal components analysis" in Statistical analysis and rest of text). 1. Sikorski and Hieter (1989); 2. EUROSCARF; 3. Nonaka et al. (1995); 4. Wertman et al. (1992); 5. Imamura et al. (1997); 6. Li et al. (2011); 7. Ohya et al. (1986a); 8. Qadota et al. (1996).

Table S3. Ca^{2+} sensitivity of the wild type and mutants of actin-mediated endocytic proteins.

Strain	YPD	YPD + 100 mM $CaCl_2$	YPD + 300 mM $CaCl_2$	Source
Wild-type	++	++	++	1
Endocytic coat module				
chc1Δ	++	++	++	1
clc1Δ	++	++	++	1
ent1Δ	++	++	++	1
ent2Δ	++	++	++	1
ede1Δ	++	++	++	1
yap1801Δ	++	++	++	1
yap1802Δ	++	++	++	1
sla1Δ	++	++	++	1
pan1-4	++	++	++	2
end3Δ	++	++	++	1
Actin nucleation and polymerization				
arp2-14	++	++	++	2
las17-1	++	++	++	2
las17-13	++	++	++	2
las17-14	++	++	++	2
myo3Δ	++	++	++	1
myo5Δ	++	++	++	1
bbc1Δ	++	++	++	1
sla1Δ	++	++	++	1
vrp1Δ	++	++	++	1
bzz1Δ	++	++	++	1
ysc84Δ	++	++	++	1
F-actin regulation				
cap1Δ	++	++	++	1
cap2Δ	++	++	++	1
sac6Δ	++	++	++	1
scp1Δ	++	++	++	1
cof1-5	++	++	++	2
cof1-8	++	++	++	2
Other				
abp1Δ	++	++	++	1
rvs161Δ	++	++	++	1

continued on following page

Table S3—continued

Strain	YPD	YPD + 100 mM $CaCl_2$	YPD + 300 mM $CaCl_2$	Source
rvs167Δ	++	++	++	1
vps1Δ	++	++	++	1
arf3Δ	++	++	++	1
ark1Δ	++	++	++	1
prk1Δ	++	++	++	1

Cells were incubated at 25ºC for 4 days. BY4741 *his3Δ* was used as the wild type. ++, normal growth; +, slow growth; ±, very slow growth; –; no growth. 1. EUROSCARF; 2. Li et al. (2011).

Figures

Fig. 9

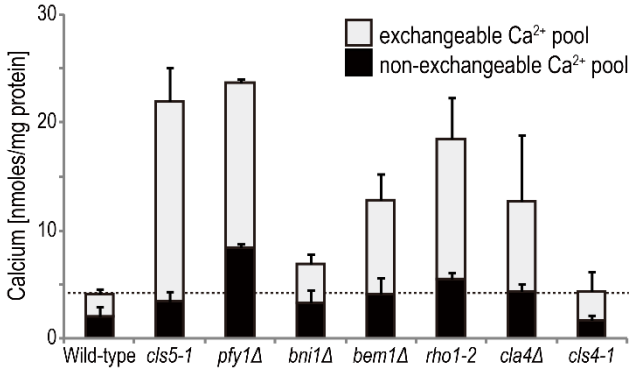

Figure 9. Intracellular Ca^{2+} pools in the wild type and several Ca^{2+}-sensitive mutants. Black and gray bars indicate exchangeable and non-exchangeable Ca^{2+} pools, respectively. Intracellular exchangeable and non-exchangeable Ca^{2+} pools were measured in the wild type (YPH499), *cls5-1* (YOC989), *pfy1Δ* (YOC992), *bni1Δ* (YOC4940), *bem1Δ* (YOC4939), *rho1-2* (YOC752), *cla4Δ* (YOC4941), and *cls4-1* (YOC138-1C) as described by Cunningham and Fink (1994) with some modifications. The average value of three independent experiments is shown (n = 3). Error bars indicate ±S.D.

Fig. 10

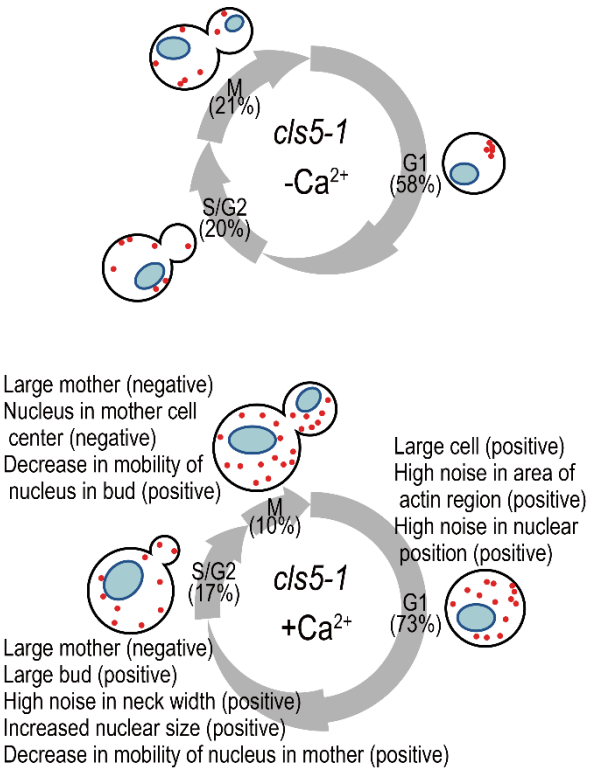

Figure 10. Illustration of Ca^{2+}-induced morphological changes by extracellular Ca^{2+} in *cls5-1* mutant cells. The *cls5-1*-Ca^{2+} and *cls5-1*+Ca^{2+} designations indicate low and high concentrations of Ca^{2+}, respectively, in the medium. The blue and red parts in the yeast cells indicate the nucleus and actin, respectively.

Fig. 11

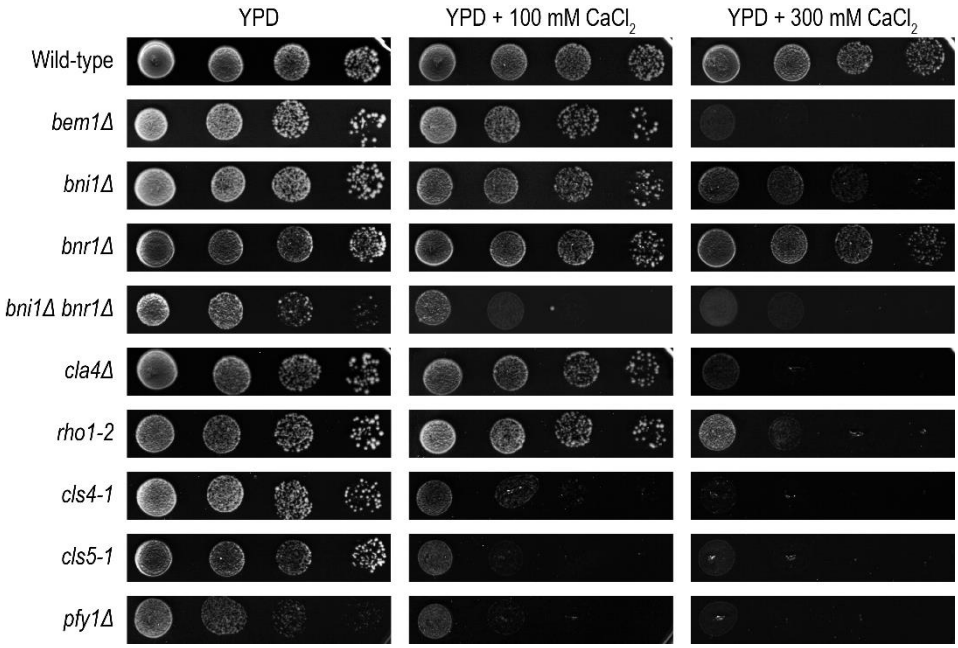

Figure 11. Ca^{2+} sensitivity of several mutants of proteins that physically bind to profilin. Serial tenfold dilutions of log-phase cultures of the wild type and Ca^{2+}-sensitive mutants were spotted onto YPD plates, YPD plates supplemented with 100 mM $CaCl_2$, or YPD plates supplemented with 300 mM $CaCl_2$. Ten microliters of a 1×10^7 cells/ml culture were spotted on the left end. The cells were incubated at 30ºC for 3 days.

Fig. 12

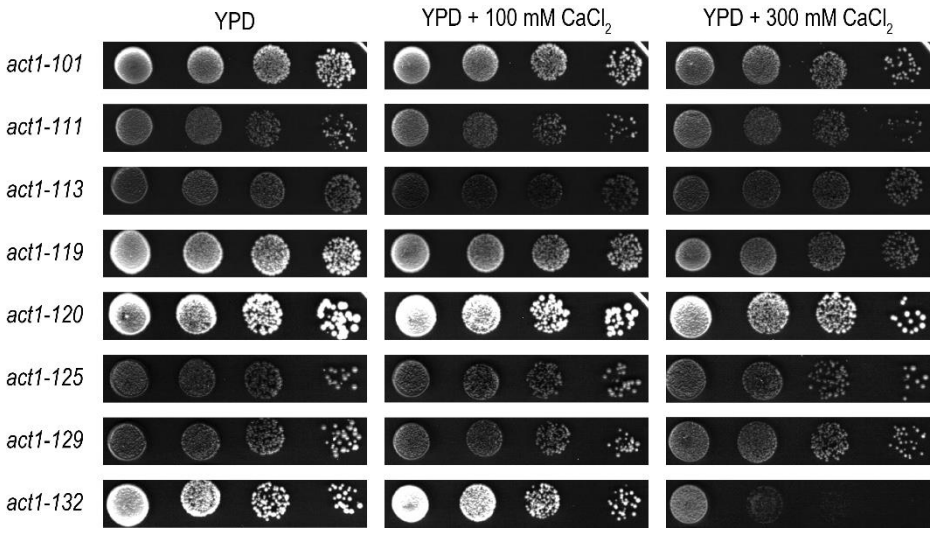

Figure 12. Ca^{2+} sensitivity of *act1* mutants. Serial tenfold dilutions of log-phase cultures of several *act1* mutants were spotted onto YPD plates, YPD plates supplemented with 100 mM $CaCl_2$, or YPD plates supplemented with 300 mM $CaCl_2$. Ten microliters of a 1×10^7 cells/ml culture were spotted on the left end. The cells were incubated at 23ºC for 5 days.

Fig. 13

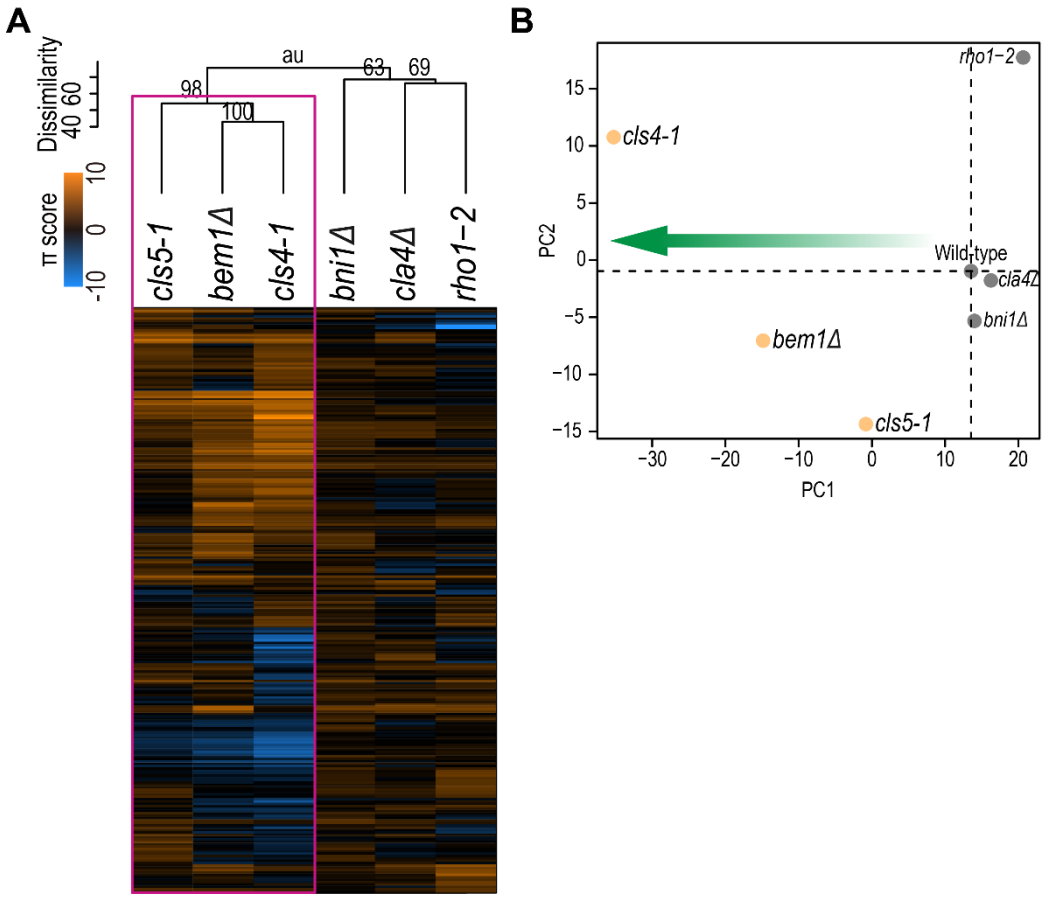

Figure 13. Morphological analysis of the Ca^{2+}-sensitive mutants based on similarities of Ca^{2+}-*cls* interaction profiles. A. The orange and blue boxes indicate π scores that reflect degree of Ca^{2+}-*cls* interaction. Positive and negative values of π score are depicted in orange and blue, respectively. Dissimilarity indicates a positive angle (0º to 180º) (Ohnuki *et al.*, 2007) between the vectors of 247 dimensions. Black values indicate AU *P* value calculated from the multiple bootstrap technique in the dendrogram (Suzuki and Shimodaira, 2006). The magenta rectangle indicates robustly clustered mutants at AU $P > 0.95$ calculated by the multi-scale bootstrap technique with 3000 iterations. Clusters were assessed using the R package pvclust tool. **B.** Distribution of PC scores for PC1 and PC2. Strains are represented by their coordinates along the first two principal components. Green arrows indicates a decrease in PC1 score, which is characteristic of the *cls5-1*, *cls4-1*, and *bem1Δ* mutant cells.

Fig. 14

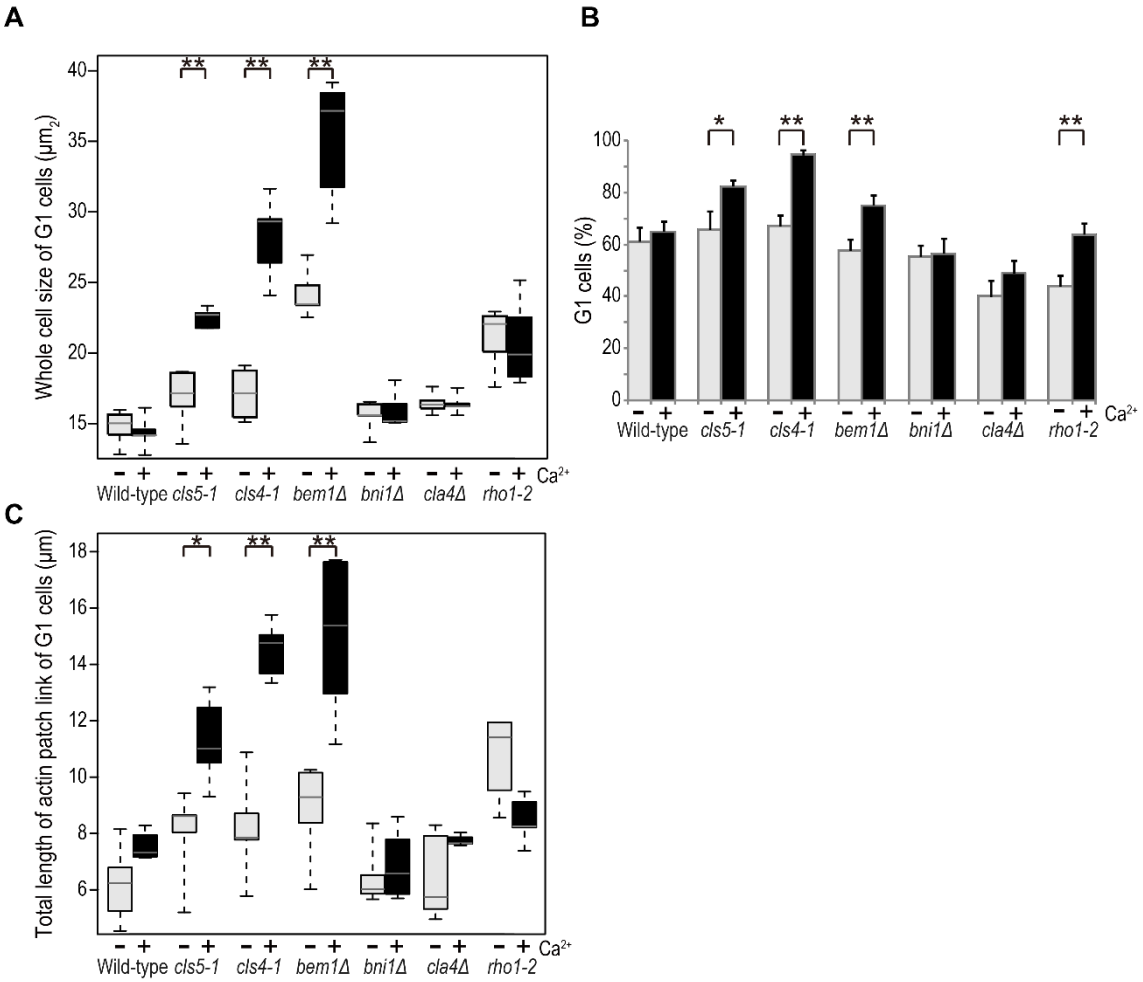

Figure 14. Distribution of parameter values representing morphological similarity among *cls5-1*, *cls4-1*, and *bem1Δ* mutant cells. A. Whole cell sizes of G1 cells of the wild type and indicated mutants in YPD supplemented with (black box) or without (light gray box) 100 mM $CaCl_2$ were from CalMorph parameter value C11-1A. C11-1A is one of the representative parameters of PC1a. Bars indicate maximum and minimum value of each sample, respectively. Gray lines indicate median of each sample. **B.** The ratios of G1 cells of the wild type and indicated mutants in YPD supplemented with or without 100 mM $CaCl_2$ were from CalMorph parameter value C119. C119 is one of the representative parameters of PC1b. Average value of five independent experiments is shown (n = 5). Bars indicate ±S.D. **C.** Total lengths of actin patch links of G1 cells in each strain in YPD supplemented with or without 100 mM $CaCl_2$ from CalMorph parameter value A120_A. A120_A is one of the representative parameters of PC1b. * and ** indicate $P <$ 0.05 and < 0.01 (U test), respectively.

Fig. 15

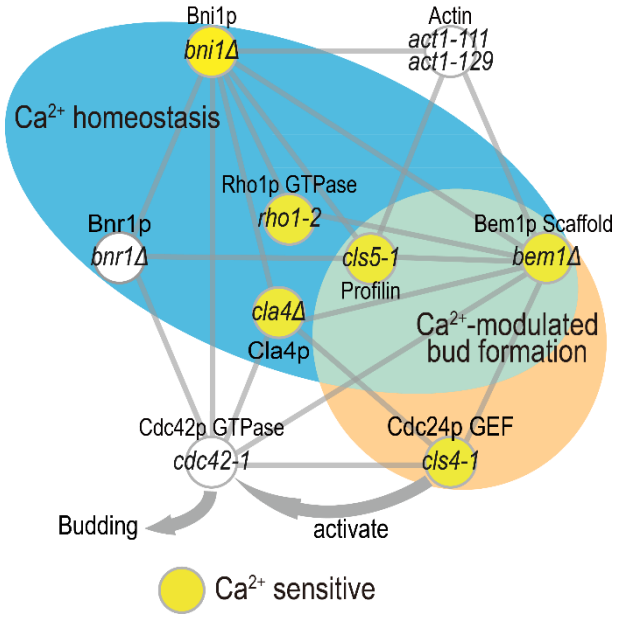

Figure 15. A model of the functional network of profilin in the maintenance of Ca^{2+} homeostasis and Ca^{2+}-modulated bud formation. Proteins included in the cyan circle (profilin, Bni1p/Bnr1p, Bem1p, Rho1p, and Cla4p) are required for maintaining Ca^{2+} homeostasis. Proteins included in the orange circle (profilin, Bem1p, and Cdc24p) are required for Ca^{2+}-modulated bud formation. Yellow circles indicate Ca^{2+}-sensitivity of the corresponding mutant. Gray lines indicate physical interaction between proteins. Physical interaction networks between proteins were illustrated by GENEMANIA (http://www.genemania.org/).

Fig. S9

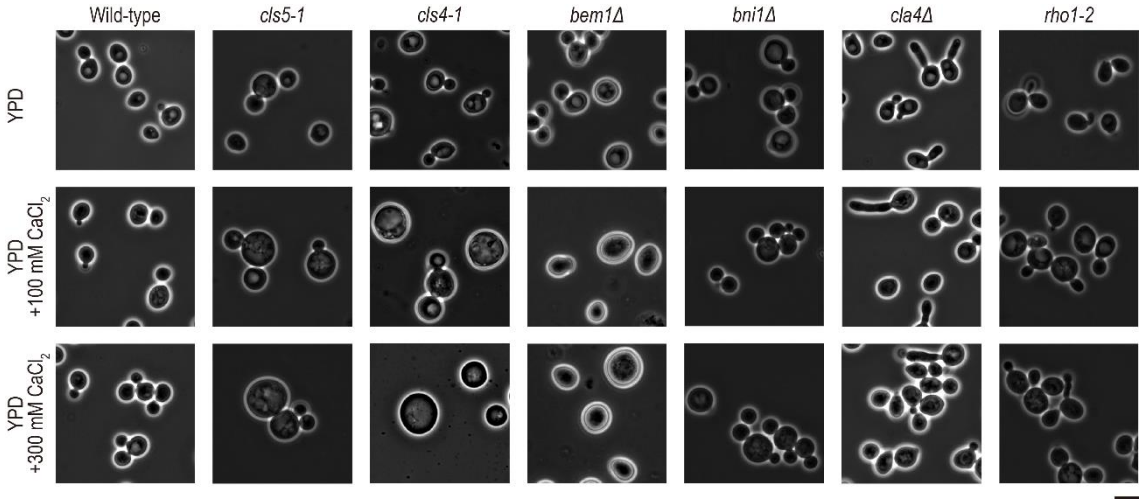

Figure S9. Phase-contrast images of the wild type, *cls5-1*, *cls4-1*, *bem1Δ*, *bni1Δ*, *cla4Δ*, and *rho1-2* cells. Wild-type (YPH499), *cls5-1* (YOC989), *bni1Δ* (YOC4940), *bem1Δ* (YOC4939), *rho1-2* (YOC752), *cla4Δ* (YOC4941), and *cls4-1* (YOC138-1C) cells were incubated for 5 h in YPD media supplemented with 0, 100, or 300 mM $CaCl_2$. Bar, 5 µm.

Fig. S10

PC	Parameter ID	Description	Loadings	*P* value	$\pi_{cls5\text{-}1}$	Z_{wt}	Morphological feature
PC1	C101_A1B	Whole cell size	-0.93	9.47E-51	3.43	-0.04	Mother cell size at G1,
	C11-1_A1B	Mother cell size	-0.92	2.22E-46	-2.92	0.08	S/G2, and M phase
	C12-1_A1B	Mother cell outline length	-0.91	1.32E-43	2.81	-0.10	
	C128_A1B	Distance between middle point of neck and mother hip	-0.90	4.58E-42	-2.61	0.42	
	C104_A1B	Short axis length in mother	-0.89	7.49E-41	-2.55	0.43	
	C103_A1B	Long axis length in mother	-0.89	5.86E-40	3.25	-0.28	
	C11-1_C	Mother cell size	-0.88	3.76E-38	-2.41	1.04	
	C104_C	Short axis length in mother	-0.88	6.83E-38	-2.15	1.00	
	C102_A1B	Whole cell outline length	-0.87	2.50E-36	3.92	-0.51	
	C101_C	Whole cell size	-0.86	3.63E-33	-2.21	0.54	
	C12-1_C	Mother cell outline length	-0.85	8.59E-33	-2.65	0.75	
	D142_A1B	Distance between nuclear brightest point and mother hip	-0.84	1.74E-31	5.31	-2.25	
	C112_A1B	Distance between middle point of neck and mother center	-0.83	8.80E-30	-2.71	0.00	
	D129_A1B	Distance between nuclear brightest point and mother tip	-0.83	1.61E-29	6.34	-3.07	
	C103_C	Long axis length in mother	-0.82	3.20E-28	-2.62	0.97	
	C128_C	Distance between middle point of neck and mother hip	-0.82	1.61E-27	-2.99	0.79	
	D104_A1B	Distance between nuclear gravity center and mother tip	-0.82	2.09E-27	5.08	-1.97	
	C112_C	Distance between middle point of neck and mother center	-0.75	2.45E-20	-3.07	0.05	
	D136_A1B	Distance between nuclear brightest point and mother center	-0.74	9.25E-20	4.87	-3.78	
	D126_A1B	Distance between nuclear gravity center and mother hip	-0.74	1.44E-19	3.97	-0.99	
	D127_A	Distance between nuclear brightest point and cell tip	-0.73	7.99E-19	4.28	-2.05	
	D102_A	Distance between nuclear gravity center and mother tip	-0.70	1.48E-16	4.92	-1.95	
	C104_A	Short axis length in whole cell	-0.70	2.44E-16	-3.12	0.54	
	C113_A1B	Distance between bud tip and mother long axis through middle point of neck	-0.69	9.79E-16	2.43	-1.36	
	C11-1_A	Whole cell size	-0.68	5.22E-15	4.17	-0.47	
	D118_A1B	Distance between nuclear gravity center and mother center	-0.67	3.78E-14	3.00	-1.83	
	D135_A	Distance between nuclear brightest point and cell center	-0.67	4.44E-14	3.07	-2.28	
	C12-1_A	Whole cell outline length	-0.66	9.19E-14	4.29	-0.79	
	D117_A	Distance between nuclear gravity center and cell center	-0.63	5.53E-12	3.11	-1.23	
	D148_A1B	Relative distance of nuclear brightest point to mother center	-0.62	1.69E-11	3.40	-3.86	
	C103_A	Long axis length in whole cell	-0.61	1.22E-10	4.97	-1.73	
	C109_A1B	Neck width	-0.57	6.14E-09	2.66	-0.15	
	D145_A1B	Distance between nuclear outline point D7 and mother hip	-0.57	7.73E-09	3.77	-1.35	
	C108_A1B	Short axis length in bud	-0.55	5.68E-08	3.05	-0.18	
	D170_A1B	Angle between C4-1D2-1 and C4-1C1	-0.55	6.74E-08	3.47	-3.57	
	C11-2_A1B	Bud cell size	-0.52	7.64E-07	2.09	-0.45	
	D128_C	Distance between nuclear brightest point in mother and mother tip	-0.49	5.42E-06	2.88	-0.79	
PC2	D175_A1B	Maximal distance between nuclear gravity center and nuclear outline	0.84	7.35E-31	2.34	-0.96	Nuclear size at S/G2
	D178_A1B	Nuclear long axis length	0.84	1.55E-30	2.35	-0.89	phase, ratio of cells in
	D190_A1B	Distance between nuclear gravity center and brightest point	0.81	1.40E-26	2.66	-1.99	which the nucleus is
	D212	nuclear B ratio to nuclear AA1BC cells	0.77	1.52E-22	2.34	-2.36	dividing at the neck
	D14-3_A1B	Nuclear size	0.77	1.57E-22	2.09	-0.59	
	D201	nuclear B ratio	0.77	2.32E-22	2.16	-2.36	
	D208	nuclear B ratio to budded cells	0.76	2.21E-21	2.25	-1.86	
	D215	nuclear B ratio to nuclear A1BC cells	0.76	2.30E-21	2.61	-1.85	
	D145_A1B	Distance between nuclear outline point D7 and mother hip	-0.56	2.08E-08	3.77	-1.35	
	D174_C	Maximal distance between nuclear gravity center and nuclear outline in bud	0.52	4.55E-07	2.07	-2.33	
	D169_C	Angle between C4-1D1-1 and C4-1C1	-0.51	1.34E-06	2.01	-1.61	
	D177_C	Nuclear long axis length in bud	0.50	4.79E-06	2.10	-2.14	

Continued on following page

Fig. S10—Continued

PC	Parameter ID	Description	Loadings	*P* value	$\pi_{cls5\text{-}1}$	Z_{wt}	Morphological feature
PC3	D125_C	Distance between nuclear gravity center in mother and mother hip	0.68	5.86E-15	-2.08	0.27	Nuclear position at S/G2
	D107_A1B	Ratio of D104 to C103	0.62	3.63E-11	2.45	-2.93	and M phase
	D141_C	Distance between nuclear brightest point in mother and mother hip	0.60	1.62E-10	2.46	-0.25	
	D152_A1B	Mobility of nucleus in mother	-0.55	3.97E-08	2.68	2.52	
	C103_A	Long axis length in whole cell	-0.52	8.99E-07	4.97	-1.73	
	C12-1_A	Whole cell outline length	-0.49	9.26E-06	4.29	-0.79	
PC4	D152_A1B	Mobility of nucleus in mother	0.59	7.95E-10	2.68	2.52	Nuclear mobility
	D103_C	Distance between nuclear gravity center in mother and mother tip	0.56	1.54E-08	2.65	-0.23	
	D153_C	Mobility of nucleus in bud	-0.55	6.00E-08	2.30	1.46	
	D128_C	Distance between nuclear brightest point in mother and mother tip	0.54	1.53E-07	2.88	-0.79	
	D141_C	Distance between nuclear brightest point in mother and mother hip	0.50	5.34E-06	2.46	-0.25	
	D107_A1B	Ratio of D104 to C103	-0.49	8.41E-06	2.45	-2.93	
PC5	C11-2_A1B	Bud cell size	-0.52	5.96E-07	2.09	-0.45	Bud cell size at S/G2
	C110_A1B	Distance between bud tip and mother long axis extension	-0.52	7.93E-07	2.91	-2.11	phase
	C12-2_A1B	Bud cell outline length	-0.52	9.03E-07	2.23	-0.81	
	D15-1_A	Nuclear brightness	0.50	2.65E-06	2.35	-1.17	
PC6	D209	nuclear C ratio to budded cells	0.61	6.98E-11	-2.10	-1.73	ratio of cells with one
	D15-3_A1B	Nuclear brightness	0.57	6.24E-09	2.24	-0.43	nucleus in the mother and
	D15-1_A	Nuclear brightness	0.54	9.72E-08	2.35	-1.17	bud
	D206	nuclear A ratio to no bud cells	0.51	1.09E-06	-3.00	-0.25	
PC7	CCV116_A1B	Noise of C116 A1B	0.56	2.11E-08	2.23	-1.31	Noise of neck width at
	CCV109_A1B	Noise of C109 A1B	0.53	4.21E-07	2.52	-1.76	S/G2 phase
PC8	ACV121_A	Noise of A121 A	0.58	1.86E-09	2.20	-2.05	Noise of distance between
	ACV122_A1B	Noise of A122 A1B	0.52	4.41E-07	2.03	-0.47	actin patches
PC9	A104_A1B	Relative distance of actin patch center from neck in bud	0.53	3.40E-07	2.23	-1.69	Actin region in bud at
	ACV120_A	Noise of A120 A	-0.50	5.24E-06	2.09	-1.48	S/G2 phase

Figure S10. Parameter descriptions for the principal components representing independent morphological features of Ca^{2+}-*cls* interactions in *cls5-1* mutant. Loadings indicate correlations between PC scores and parameter values of the null distribution. The *P* value was calculated by *t* test of loadings, where the alternative hypothesis of the *t* test is loadings ≠ 0 (Ohnuki et al. 2012). Yellow and blue boxes indicate positive and negative π scores, respectively, which indicate degree of Ca^{2+}-*cls* interaction in each parameter. Red and green indicate positive and negative values of Z_{wt} scores, respectively, which indicate increases and decreases of parameter values by Ca^{2+} treatment.

Fig. S11

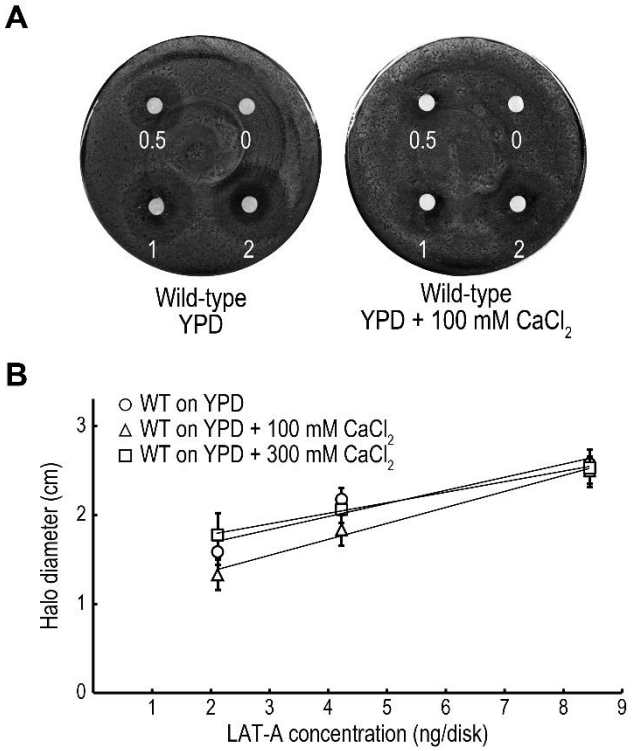

Figure S11. Ca^{2+} sensitivity of the wild-type cells in the presence of latrunculin-A. Halo assay was used to assess the Ca^{2+} sensitivity of the wild-type (YPH499) cells in the presence of latrunculin-A. The halo assay was performed as described by Ayscough et al. (1997). **A.** Representative examples of the halo assay. Ten microliters of 0.5 mM, 1 mM, and 2 mM latrunculin-A were spotted in each plate, respectively. The plates were incubated for 3 days at 25ºC. **B.** The relationship between the halo size and latrunculin-A dose. The average value of three independent experiments is shown (n = 3). Bars indicate ± SD.

Fig. S12

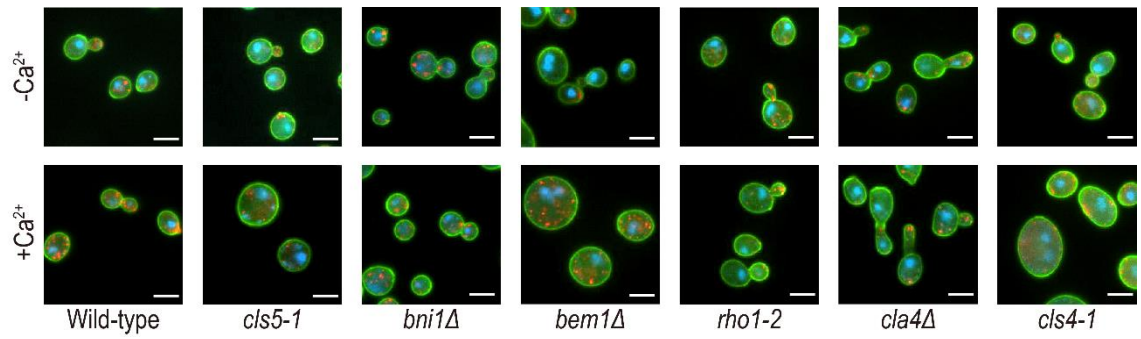

Figure S12. Triple staining images of several Ca^{2+}-sensitive mutants and the wild type in the presence of 100 mM $CaCl_2$. $-Ca^{2+}$ and $+Ca^{2+}$ indicate treatment with YPD supplemented without or with 100 mM $CaCl_2$, respectively. Wild-type (YPH499), *cls5-1* (YOC989), *bni1Δ* (YOC4940), *bem1Δ* (YOC4939), *rho1-2* (YOC752), *cla4Δ* (YOC4941), and *cls4-1* (YOC138-1C) cells were fixed and stained with FITC-ConA (cell wall), rhodamine–phalloidin (actin), and DAPI (nucleus) for image analysis with CalMorph. CalMorph automatically characterizes yeast cells using 501 parameters (Ohya *et al.*, 2005) Bars, 5 μm.

Fig. S13

PC1	Proportion of variance	parameter ID	Description	Loadings (2nd PCA)	*P* value	Loadings (1st PCA)	Z_{wi}	Morphological feature
PC1a	0.22	C101_C	Whole cell size	-0.95	2.94E-58	1.00	0.54	Whole cell size at G1,
		C11-1_C	Mother cell size	-0.94	1.58E-53	0.99	1.04	S/G2, and M phase
		C104_C	Short axis length in mother	-0.93	3.99E-51	0.98	1.00	
		C102_C	Whole cell outline length	-0.92	5.45E-48	-0.99	-0.08	
		C11-1_A1B	Mother cell size	-0.91	1.95E-45	0.96	0.08	
		C12-1_C	Mother cell outline length	-0.91	4.70E-45	0.98	0.75	
		C12-1_A1B	Mother cell outline length	-0.91	6.82E-44	-0.95	-0.10	
		C128_A1B	Distance between middle point of neck and mother hip	-0.90	1.21E-41	0.90	0.42	
		D185_C	Relative distance of two nuclear gravity centers to middle point of neck	-0.89	1.42E-40	-0.98	-0.05	
		C103_A1B	Long axis length in mother	-0.89	1.02E-39	-0.97	-0.28	
		C104_A1B	Short axis length in mother	-0.89	1.66E-39	0.97	0.43	
		D186_C	Relative distance of two nuclear brightest points to middle point of neck	-0.89	7.42E-39	0.99	0.37	
		C103_C	Long axis length in mother	-0.89	8.99E-39	0.98	0.97	
		C128_C	Distance between middle point of neck and mother hip	-0.88	1.83E-37	0.98	0.79	
		C101_A1B	Whole cell size	-0.87	3.53E-36	-0.96	-0.04	
		C112_A1B	Distance between middle point of neck and mother center	-0.85	1.03E-32	0.79	0.00	
		C112_C	Distance between middle point of neck and mother center	-0.84	4.98E-30	0.96	0.05	
		C11-2_C	Bud cell size	-0.83	6.45E-29	-0.94	-0.45	
		C107_C	Long axis length in bud	-0.81	5.16E-27	-0.88	-1.12	
		C113_C	Distance between bud tip and mother long axis through middle point of neck	-0.80	9.79E-26	-0.92	-0.54	
		C12-2_C	Bud cell outline length	-0.80	9.07E-25	-0.93	-1.02	
		C102_A1B	Whole cell outline length	-0.79	4.89E-24	-0.90	-0.51	
		D129_A1B	Distance between nuclear brightest point and mother tip	-0.74	2.30E-19	-0.72	-3.07	
		C108_C	Short axis length in bud	-0.73	3.74E-18	0.92	0.46	
		D134_C	Distance between two nuclear brightest points	-0.69	1.26E-15	-0.80	0.00	
		D104_A1B	Distance between nuclear gravity center and mother tip	-0.69	1.42E-15	-0.73	-1.97	
		C104_A	Short axis length in whole cell	-0.68	1.14E-14	0.98	0.54	
		D127_A	Distance between nuclear brightest point and cell tip	-0.66	1.80E-13	-0.90	-2.05	
		D116_C	Distance between two nuclear gravity centers	-0.66	2.26E-13	0.92	0.29	
		C11-1_A	Whole cell size	-0.66	2.73E-13	-0.97	-0.47	
		D102_A	Distance between nuclear gravity center and mother tip	-0.64	2.73E-12	-0.88	-1.95	
		C12-1_A	Whole cell outline length	-0.64	4.15E-12	-0.97	-0.79	
		C109_C	Neck width	-0.62	4.74E-11	0.89	0.89	
		D131_C	Distance between nuclear brightest point in bud and middle point of neck	-0.61	1.25E-10	-0.73	-0.45	
		D130_C	Distance between nuclear brightest point in mother and middle point of neck	-0.61	2.20E-10	-0.90	-0.16	
		C103_A	Long axis length in whole cell	-0.58	4.16E-09	-0.96	-1.73	
		C115_C	Mother axis ratio	-0.58	5.32E-09	-0.87	0.74	
		DCV14-1_A	Noise of D14-1 A	0.57	1.35E-08	-0.84	0.86	
		C13_A1B	Mother cell fitness for ellipse	0.56	1.83E-08	0.90	-2.23	
PC1b	0.11	A120_A1B	Total length of actin patch link	0.86	4.36E-33	0.83	1.72	Actin localization, ratio of
		A121_A1B	Maximal distance between patches	0.85	6.81E-32	0.81	1.46	no bud cells
		A120_A	Total length of actin patch link	0.82	7.27E-28	0.89	2.08	
		A121_A	Maximal distance between patches	0.81	2.67E-26	0.89	1.53	
		A120_C	Total length of actin patch link	0.80	2.08E-25	0.84	2.06	
		A122_A	Number of bright actin patches	0.80	3.60E-25	0.81	2.37	
		A122_A1B	Number of bright actin patches	0.80	8.40E-25	0.78	2.32	
		A121_C	Maximal distance between patches	0.78	3.46E-23	0.79	1.64	
		A8-1_A	Actin region brightness	0.76	1.89E-21	0.88	3.97	
		A8-1_A1B	Total brightness of actin region in mother	0.72	2.04E-17	0.87	2.67	
		A8-1_C	Total brightness of actin region in mother	0.69	3.23E-15	0.80	2.06	
		D199	nuclear A ratio	-0.68	5.42E-15	0.75	2.34	
		D210	nuclear A ratio to nuclear AA1BC cells	-0.66	1.14E-13	0.83	2.93	
		A108	actin d ratio	0.66	1.59E-13	0.88	-1.53	
		C119	no bud ratio	-0.66	2.33E-13	0.76	3.03	

Continued on following page

Fig. S13—Continued

PC1	Proportion of variance	parameter ID	Description	Loadings (2nd PCA)	*P* value	Loadings (1st PCA)	Z_{wt}	Morphological feature
PC1c	0.09	D143_A1B	Distance between nuclear outline point D6-1 and middle point of neck	0.65	6.86E-13	0.73	1.84	Nuclear brightness of
		C123	small bud ratio to budded cells	0.63	1.34E-11	0.80	1.11	cells at G1, S/G2, M
		D15-1_C	Nuclear brightness in mother	-0.61	1.31E-10	0.82	0.21	phase
		D15-1_A	Nuclear brightness	-0.61	1.76E-10	-0.96	-1.17	
		D15-3_C	Nuclear brightness in whole cell	-0.60	6.10E-10	-0.85	-0.56	
		C123_A1B	Small bud ratio	0.58	4.50E-09	0.92	0.76	
		D15-3_A1B	Nuclear brightness	-0.58	5.12E-09	-0.91	-0.43	
		D15-2_C	Nuclear brightness in bud	-0.57	1.23E-08	-0.90	-1.55	
PC1d	0.06	D14-3_A1B	Nuclear size	0.67	2.93E-14	-0.93	-0.59	Nucler size of cells at
		D181_A1B	Nuclear short axis length	0.66	2.34E-13	-0.97	-0.05	S/G2 and M phase
		D175_A1B	Maximal distance between nuclear gravity center and nuclear outline	0.63	1.15E-11	-0.94	-0.96	
		D178_A1B	Nuclear long axis length	0.63	2.03E-11	-0.94	-0.89	
		D177_C	Nuclear long axis length in bud	0.57	1.44E-08	-0.92	-2.14	
		D174_C	Maximal distance between nuclear gravity center and nuclear outline in bud	0.55	8.47E-08	-0.88	-2.33	
PC1e	0.05	C124	medium bud ratio to buded cells	-0.59	1.41E-09	-0.96	0.67	Ratio of cells with midium bud to budded cells
PC1f	0.04	CCV11-1_A1B	Noise of C11-1 A1B	-0.66	2.11E-13	-0.90	0.17	Noise of cell size at S/G2
		CCV12-1_A1B	Noise of C12-1 A1B	-0.66	2.59E-13	-0.88	0.26	phase
		CCV103_A1B	Noise of C103 A1B	-0.62	5.73E-11	-0.85	1.62	
		CCV128_A1B	Noise of C128 A1B	-0.58	2.38E-09	-0.93	0.70	
PC1g	0.04	D125_C	Distance between nuclear gravity center in mother and mother hip	0.65	8.75E-13	0.91	0.27	Nuclear position in cells at
		D103_C	Distance between nuclear gravity center in mother and mother tip	0.63	1.23E-11	-0.86	-0.23	M phase of the cell cycle
		D141_C	Distance between nuclear brightest point in mother and mother hip	0.62	2.49E-11	-0.80	-0.25	

Figure S13 Parameter descriptions for the principal components representing common morphological features in *cls5-1*, *cls4-1*, and *bem1Δ* mutant cells. Red and green indicate positive and negative values of Z_{wt} scores, respectively, which indicate increases and decreases of parameter values by Ca^{2+} treatment. First seven principal components (PC1a to PC1g) reached to 60% of the CCR, which explained 60% of variance in the PC1.

Fig. S14

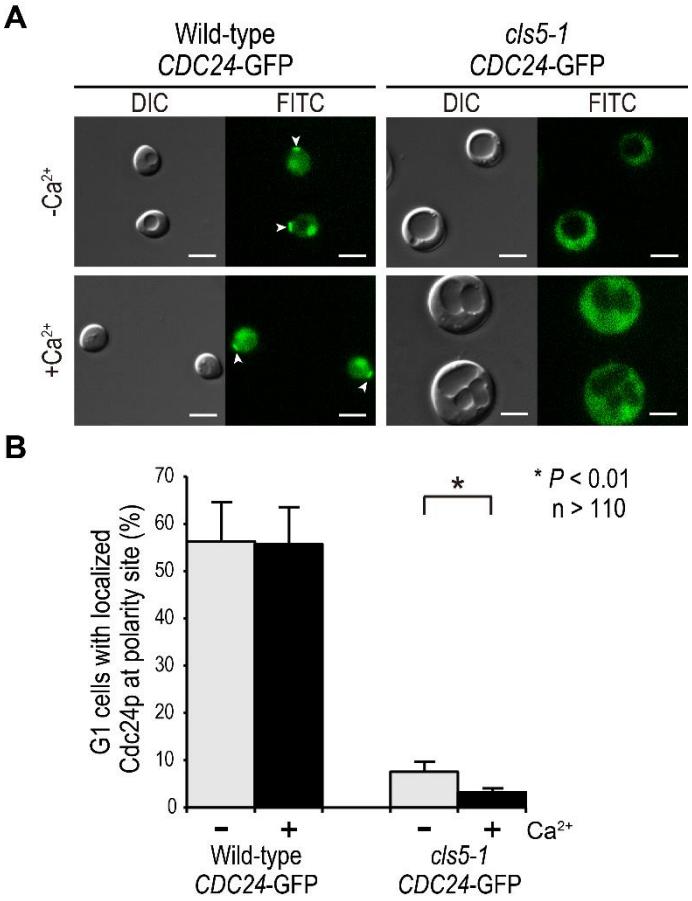

Figure S14. Polarized localization of Cdc24p in G1 cells of wild-type and *cls5-1* in the presence of 100 mM $CaCl_2$. A. $-Ca^{2+}$ and $+Ca^{2+}$ indicate treatment with YPD supplemented without or with 100 mM $CaCl_2$, respectively. The wild-type (YOC5009) and *cls5-1* (YOC5010) cells during log-phase were harvested and directly observed without fixation. The arrowhead indicates Cdc24p-GFP localization at polarity site. Bar, 5 μm. **B.** Cdc24p-GFP localized G1 cells were counted in the wild-type and *cls5-1*, and average ratio of five independent experiments was shown (n = 5). Error bars indicate ±S.D. * indicate $P < 0.01$ (U test).

Materials and methods

Strains

Yeast strains used in chpter I are listed in Table S4. All strains in the chapter I are isogenic derivatives of BY4741 (*MAT***a**; *his3*; *leu2*; *met15*; *ura3*) (EUROSCARF: http://www.uni-frankfurt.de/fb15/mikro/euroscarf/2000). Two mutants, *cls4-1* and *cls5-1* were constructed from YOC138-C (*MAT***a** *ade1 cls4-1*) (Ohya *et al.*, 1986a) and YOC989 (*MATα leu2 lys2 trp1 ura3 cls5-1*) (Yoshida *et al.*, 2013). Briefly, a kanamycin-resistant cassette amplified by the plasmid pFA6a-GFP(S65T)-kanMX6 (Longtine *et al.*, 1998) targeted to the 3' UTR region of the *CLS4* and *CLS5* genes and placed ~250 bp downstream of the stop codon. Then, the *cls4-1* and *cls5-1* locus linked to the kanamycin-resistant cassette were amplified by polymerase chain reaction (PCR). The amplified fragments were used to transform BY4741 and geneticin-resistant transformants were selected. Replacement of the wild-type *CLS4* and *CLS5* gene were confirmed by PCR and sequencing.

Yeast strains used in chapter II are listed in Table S5. YOC4940, YOC4941, and YOC5008 were constructed by gene replacement to disrupt the *BNI1*, *CLA4*, and *BNR1* genes in a YPH499 background. To construct YOC5009 and YOC5010 by gene replacement, I used a strain with GFP-tagged CDC24p that was purchased from Invitrogen Corporation (Carlsbad, CA, USA). All replacements were confirmed by PCR. Because I could not construct the *bem1* deletion strain in the YPH499 background, I alternatively constructed it in the BY4741 background (EUROSCARF).

Media and chemicals

The medium for growing *S. cerevisiae* was YPD medium that contained 1% (wt/vol) Bacto yeast extract (BD Biosciences), 2% (wt/vol) polypeptone (WAKO), and 2% (wt/vol) dextrose. YPD pH 5.5 medium was YPD medium that was buffered to pH 5.5 with 50 mM succinate-NaOH. For examination of Ca^{2+} sensitivity, YPD medium supplemented with 100 mM $CaCl_2$ was used as a Ca^{2+}-rich medium. YPG medium (1% Bacto yeast extract, 2% polypeptone, 2% [vol/vol] glycerol) was used for examination of the Pet- phenotype. To assess sensitivities to other divalent cations, YPD medium supplemented with 100 mM $MgCl_2$, 3 mM $ZnCl_2$, and 3 mM $MnCl_2$ was used. Solid media were prepared by adding 2% (wt/vol) agar to the above media. YPD medium supplemented with 0.4 μg/ml FK506 (Cayman chemical, MI, USA) and 0, 25, 50, 75, and 200 mM $CaCl_2$ were used to examine effects of FK506 on cell growth under high Ca^{2+} condition.

Measurements of exchangeable and non-exchangeable Ca^{2+} pools

Intracellular calcium content was measured as described previously (Cunningham and Fink, 1994) with some modifications. Yeast cells growing exponentially (1×10^7 to 1.5×10^7 cells/ml) in YPD (pH 5.5) medium were collected, resuspended in YPD (pH 5.5) medium containing $^{45}CaCl_2$ (> 10 Ci/g; PerkinElmer, Waltham, MA, USA), and incubated at 30ºC for 6.5 h. To determine the protein concentration, each strain was incubated without $^{45}CaCl_2$ under the same conditions as the $^{45}CaCl_2$-treated cells. Cultures were collected and suspended in 0.2 ml of 10% trichloroacetic acid. The protein content was measured using a bicinchoninic acid protein

assay kit (Pierce, Rockford, IL, USA).

Fluorescence staining and microscopy

Ca^{2+} treatment of yeast cells was performed as described previously (Ohnuki *et al.*, 2007). Cells (8×10^6 cells) at log phase in YPD medium were collected, washed once in YPD medium with or without 100 mM $CaCl_2$, and resuspended in 4 ml of the respective medium to a final concentration of 2×10^6 cells/ml. The cells were incubated for 5 hours at 30 ˚C, washed once with YPD medium, and fixed in YPD medium supplemented with 3.7% formaldehyde and resuspended in PBS [0.1 M potassium phosphate buffer (pH 6.5)]. Triple staining of the yeast cells and image analysis with CalMorph Ver. 1.0 were performed as described previously (Ohya *et al.*, 2005). Cells were stained for three components: fluorescence isothiocyanate concanavalin A (FITC-Con A) (Sigma Aldrich, St.Louis, MO, USA), rhodamine-phalloidin (Invitrogen, Carlsbad, CA, USA) and 4',6-diamidino-2-phenylindole (DAPI) (Sigma Aldrich) to stain mannnoprotein, actin and nucleus, respectively. Triple staining cells were observed and images were captured using AxioImager M1 a 100× EC-Plan NEO objective lens (Carl Zeiss) equipped with a CoolSNAP HQ cooled-CCD camera (Roper Scientific) and Axio Vision software (Carl Zeiss).

Statistical model to assess Ca^{2+}-*cls* interaction

All statistical analyses were performed using R software (http://www.r-project.org).

To statistically assess Ca^{2+}-*cls* interaction for morphological phenotype, the generalized linear model (GLM), an extension of the normal linear model was used, which applied not only a

Gaussian but also other probability distributions (Nelder and Wedderburn, 1972). The models of the probability distributions for the 501 were determined to accommodate the statistical model used in the GLM as described previously (Yang *et al.*, 2014) with some modifications. Of the 501 parameters calculated by CalMorph, 220 parameters were coefficients of variation (CV) of their related mean parameters. These CV parameters sometimes varied concomitantly with the mean parameter values, and this dependence could be uncoupled by a nonlinear Lowess regression method (Levy and Siegal, 2008). To obtain estimates of cell-to-cell variability that was independent of mean parameter values, the Lowess regression of the CV values by the mean values was performed using the lowess() function of R with a smooth span of 0.4, as described previously (Yvert *et al.*, 2013). The 220 CV parameters were assumed to be Gaussian-distributed after the normalization. A further 183 parameters, representing the mean cell morphologies with positive continuous values, were assumed to be gamma-distributed, as described previously (Yang *et al.*, 2014). Another 37 parameters, representing the mean cell morphologies with continuous values ranging from zero to one, were assumed to be beta- or zero-inflated beta-distributed. The remaining 61 parameters, representing the ratio of cells in specimen, were assumed to be binomial- or beta-binomial-distributed with or without over dispersion, respectively.

I used an analysis of covariance (ANCOVA) model which is a blend of analysis of variance (ANOVA) and regression in the multiple liner model for the assessment of Ca^{2+} treatment and mutation effects on the cells with the parameters of Gaussian, gamma, beta, zero-

inflated beta, binomial and beta-binomial in a manner of the GLM. The statistical model was defined by

$$\eta(y_i) = \beta_0 + \beta_1 x_i + \beta_2 d_i + \beta_3 x_i . d_i + \beta_4 e_i + \varepsilon_i$$

$$d_i = \begin{cases} 0 & \text{did not harbor mutation} \\ 1 & \text{harbored mutation} \end{cases}$$

$$e_i = \begin{cases} 0 & \text{without confounding factor} \\ 1 & \text{with confounding factor} \end{cases}$$

where η is the link function, y_i is a response variable (parameter values), β_0 is the intercept, β_1 is a fixed effect of Ca^{2+} treatment, x_i is a concentration of Ca^{2+} treatment as an explanatory variable for y_i, β_2 is a fixed effect of *cls* mutation, d_i is an indicator of the mutation as an explanatory variable, β_3 is a fixed effect of Ca^{2+}-*cls* interaction of which the explanatory variable $x_i . d_i$ of the interaction term was defined as a product of x_i and d_i in the linear model, β_4 is a fixed effect of the confounding factor, e_i is an indicator of the confounding factor as an explanatory variable, and ε_i is the error, respectively. The best model was selected from the combination of the probability distributions and the linear models (e.g. zero-inflated beta vs beta, binomial vs beta-binomial, with or without cofounding factor) for each parameter based on Akaike Information Criterion (AIC) (Akaike, 1998). Likelihood ratio test for the interaction term was performed to detect parameters that showed Ca^{2+}-*cls* interactions among sets of *cls* mutants in chapter I and II, respectively. The models of the probability distributions, corresponding link functions, and descriptions for the 209 (chapter I) and 247 (chapter II) parameters are listed in Table S6 and S7, respectively. The *Z* value calculated by Wald test for β_1 of the maximum likelihood estimation in each parameter was used as degree of Ca^{2+}-induced

morphological change of the wild-type (*his3Δ* or YPH499) in this study (termed Z_{wt} in text and figures). The Z value calculated by Wald test for β_3 of the maximum likelihood estimation in each of *cls* mutant was used as degree of Ca^{2+}-*cls* interaction in this study (termed Z_{int}). The π-score as a phenotypic interaction score was calculated by following equation:

$$\pi = \begin{cases} Z_{int} & if\ (\beta_1 > 0\ and\ \beta_3 > 0)\ or\ (\beta_1 < 0\ and\ \beta_3 < 0) \\ -Z_{int} & else\ if\ (\beta_1 > 0\ and\ \beta_3 < 0)\ or\ (\beta_1 < 0\ and\ \beta_3 > 0) \end{cases}$$

Principal component analysis and hierarchical cluster analysis

Principal components analysis (PCA) and hierarchical cluster analysis (HCA) were applied to the π-score.

To describe the independent morphological features of the 209 parameters showing Ca^{2+}-*cls* interactions detected in 62 *cls* mutants at $P < 0.05$ (Likelihood ratio test), PCA was performed as described previously (Ohnuki *et al.*, 2012) with some modifications. The 209 Z values calculated from the parameter values of the 122 replicated wild-type data set (null-distributed data) were subjected to PCA based on the correlation matrix. First 19 PCs reached to 70% of the CCR. I selected parameters significantly correlated with each PC ($P < 0.01$ after Bonferroni correction), and listed in Fig. S1.

To identify independent morphological features influenced by the addition of FK506, a two-step PCA was performed as described previously (Ohnuki *et al.*, 2012). In the first PCA, 62 Ca^{2+}-*cls* interaction profiles, each of which consisted of 209 dimensional π-score, were subjected to PCA after standardization. The alleviating and aggravating effects of FK506 on cell growth under high Ca^{2+} condition were particularly reflected in the first and second principle components

(Fig. S6, B). Of the 209 parameters, 67 and 7 parameters were significantly correlated with PC1 and PC2 at more than 0.60 of the absolute value of loadings which is equivalent to the correlation coefficient between the PC score and the π-score ($P < 5 \times 10^{-7}$ after Bonferroni correction, *t* test). In the second PCA, the 67 and the 7 parameter values for PC1 and PC2, respectively, of the 122 replicated wild-type data set (null-distributed data) were subjected to PCA. I selected parameters having more than 0.70 of absolute value of the loadings for each PC, and the parameters correlated to first five PCs (PC1a-e) and first three PCs (PC2a-c) were listed in Fig. S7 A.

To describe the independent morphological features of the 88 parameters showing Ca^{2+}-*cls* interactions in *cls5-1* (YOC989) at $P < 0.05$ (Likelihood ratio test), PCA was performed as described previously (Ohnuki *et al.*, 2012) with some modifications. The 88 *Z* values calculated from the parameter values of the 122 replicated wild-type data set (null-distributed data) were subjected to PCA. First nine PCs reached to 70% of the CCR. I selected parameters significantly correlated with each PC ($P < 1 \times 10^{-6}$ after Bonferroni correction, *t* test), and listed in Fig. S10.

To identify independent morphological features characteristic of *cls5-1*, *cls4-1*, and *bem1Δ* mutant cells, a two-step PCA was performed as described previously (Ohnuki *et al.*, 2012). In the first PCA, Ca^{2+}-*cls* interaction profiles of *cls5-1* and mutants of profilin-physically-interacting protein (*cls4-1*, *bem1Δ*, *bni1Δ*, *cla4Δ*, and *rho1-2*), each of which consisted of 247 dimensional π-score, were subjected to PCA after standardization. Characteristic Ca^{2+}-*cls* interactions of the three mutant cells were reflected in the first principle components (Fig. 13 B). Of the 247 parameters, 135 parameters were correlated with PC1 more than 0.70 of the absolute

value of loadings. In the second PCA, the 135 parameter values of the 122 replicated wild-type data set (null-distributed data) were subjected to PCA. First seven PCs reached to 60% of CCR (PC1a-g). I selected parameters significantly correlated with the PC1 ($P < 1 \times 10^{-6}$ after Bonferroni correction, *t* test), and listed in Fig. S13.

HCA for 62 *cls* mutants (Fig. 5) was performed as described previously (Ohnuki *et al.*, 2007) with some modifications. To exclude correlation within the 209 morphological parameters, we used principal component scores of the Ca^{2+}-*cls* interaction profiles. The 209 parameters were explained by 16 PCs at 80 % of the CCR, and HCA based on the dissimilarity defined by 1 minus R (Pearson product-moment correlation coefficient) was applied to the 16 PC scores of the 62 *cls* mutants. Clusters were assessed using the R package pvclust tool at AU *P* value > 0.95 (Suzuki and Shimodaira, 2006). The following options in pvclust were used: method.hclust = "average", nboot = 3000, and r = seq(0.5, 1.4, by = 0.1).

HCA for *cls5-1* and several mutants of profilin-physically-interacting protein (Fig. 13 A) was performed as described previously (Ohnuki *et al.*, 2007), based on the dissimilarity which is a form of angle defined by

$$S(\vec{a}, \vec{b}) = \cos^{-1}\left(\frac{\vec{a} \cdot \vec{b}}{|\vec{a}||\vec{b}|}\right) \times \frac{360}{2\pi}$$

where the Ca^{2+}-*cls* interaction vector $\vec{a}$ and $\vec{b}$ equal to an ordered set of π-scores for any two *cls* mutants. Clusters were assessed as described above.

Tables

Table S4 Strains used in chapter I.

Strain	Genotype	Source
his3Δ	*MAT***a**; *his3*; *leu2*; *met15*; *ura3*; *his3::Kan^R*	1
afg3Δ	*MAT***a**; *his3*; *leu2*; *met15*; *ura3*; *afg3:: Kan^R*	1
bem1Δ	*MAT***a**; *his3*; *leu2*; *met15*; *ura3*; *bem1:: Kan^R*	1
bud25Δ	*MAT***a**; *his3*; *leu2*; *met15*; *ura3*; *bud25:: Kan^R*	1
bud32Δ	*MAT***a**; *his3*; *leu2*; *met15*; *ura3*; *bud32:: Kan^R*	1
cls2Δ	*MAT***a**; *his3*; *leu2*; *met15*; *ura3*; *cls2:: Kan^R*	1
cls4-1	*MAT***a**; *his3*; *leu2*; *met15*; *ura3*; *cls4-1: Kan^R*	This study
cls5-1	*MAT***a**; *his3*; *leu2*; *met15*; *ura3*; *cls5-1: Kan^R*	This study
ctr1Δ	*MAT***a**; *his3*; *leu2*; *met15*; *ura3*; *ctr1:: Kan^R*	1
cwh36Δ	*MAT***a**; *his3*; *leu2*; *met15*; *ura3*; *cwh36:: Kan^R*	1
fet3Δ	*MAT***a**; *his3*; *leu2*; *met15*; *ura3*; *fet3:: Kan^R*	1
ftr1Δ	*MAT***a**; *his3*; *leu2*; *met15*; *ura3*; *ftr1:: Kan^R*	1
gly1Δ	*MAT***a**; *his3*; *leu2*; *met15*; *ura3*; *gly1:: Kan^R*	1
gon7Δ	*MAT***a**; *his3*; *leu2*; *met15*; *ura3*; *gon7:: Kan^R*	1
not5Δ	*MAT***a**; *his3*; *leu2*; *met15*; *ura3*; *not5:: Kan^R*	1
och1Δ	*MAT***a**; *his3*; *leu2*; *met15*; *ura3*; *och1:: Kan^R*	1
pdr13Δ	*MAT***a**; *his3*; *leu2*; *met15*; *ura3*; *pdr13:: Kan^R*	1
pho85Δ	*MAT***a**; *his3*; *leu2*; *met15*; *ura3*; *pho85:: Kan^R*	1
pkr1Δ	*MAT***a**; *his3*; *leu2*; *met15*; *ura3*; *pkr1:: Kan^R*	1
pmc1Δ	*MAT***a**; *his3*; *leu2*; *met15*; *ura3*; *pmc1:: Kan^R*	1
pro1Δ	*MAT***a**; *his3*; *leu2*; *met15*; *ura3*; *pro1:: Kan^R*	1
psl10Δ	*MAT***a**; *his3*; *leu2*; *met15*; *ura3*; *psl10:: Kan^R*	1
rcs1Δ	*MAT***a**; *his3*; *leu2*; *met15*; *ura3*; *rcs1:: Kan^R*	1
rib4Δ	*MAT***a**; *his3*; *leu2*; *met15*; *ura3*; *rib4:: Kan^R*	1
rpl22aΔ	*MAT***a**; *his3*; *leu2*; *met15*; *ura3*; *rpl22a:: Kan^R*	1
sac1Δ	*MAT***a**; *his3*; *leu2*; *met15*; *ura3*; *sac1:: Kan^R*	1
sod1Δ	*MAT***a**; *his3*; *leu2*; *met15*; *ura3*; *sod1:: Kan^R*	1
swi3Δ	*MAT***a**; *his3*; *leu2*; *met15*; *ura3*; *swi3:: Kan^R*	1
tef4Δ	*MAT***a**; *his3*; *leu2*; *met15*; *ura3*; *tef4:: Kan^R*	1
tpd3Δ	*MAT***a**; *his3*; *leu2*; *met15*; *ura3*; *tpd3:: Kan^R*	1
trk1Δ	*MAT***a**; *his3*; *leu2*; *met15*; *ura3*; *trk1:: Kan^R*	1
ubp3Δ	*MAT***a**; *his3*; *leu2*; *met15*; *ura3*; *ubp3:: Kan^R*	1
vma1Δ	*MAT***a**; *his3*; *leu2*; *met15*; *ura3*; *vma1:: Kan^R*	1
vma10Δ	*MAT***a**; *his3*; *leu2*; *met15*; *ura3*; *vma10:: Kan^R*	1
vma11Δ	*MAT***a**; *his3*; *leu2*; *met15*; *ura3*; *vma11:: Kan^R*	1

continued on following page

Table S4—continued

Strain	Genotype	Source
vma12Δ	*MAT***a**; *his3*; *leu2*; *met15*; *ura3*; *vma12:: Kan^R*	1
vma13Δ	*MAT***a**; *his3*; *leu2*; *met15*; *ura3*; *vma13:: Kan^R*	1
vma16Δ	*MAT***a**; *his3*; *leu2*; *met15*; *ura3*; *vma16:: Kan^R*	1
vma2Δ	*MAT***a**; *his3*; *leu2*; *met15*; *ura3*; *vma2:: Kan^R*	1
vma21Δ	*MAT***a**; *his3*; *leu2*; *met15*; *ura3*; *vma21:: Kan^R*	1
vma22Δ	*MAT***a**; *his3*; *leu2*; *met15*; *ura3*; *vma22:: Kan^R*	1
vma3Δ	*MAT***a**; *his3*; *leu2*; *met15*; *ura3*; *vma3:: Kan^R*	1
vma4Δ	*MAT***a**; *his3*; *leu2*; *met15*; *ura3*; *vma4:: Kan^R*	1
vma5Δ	*MAT***a**; *his3*; *leu2*; *met15*; *ura3*; *vma5:: Kan^R*	1
vma6Δ	*MAT***a**; *his3*; *leu2*; *met15*; *ura3*; *vma6:: Kan^R*	1
vma7Δ	*MAT***a**; *his3*; *leu2*; *met15*; *ura3*; *vma7:: Kan^R*	1
vma8Δ	*MAT***a**; *his3*; *leu2*; *met15*; *ura3*; *vma8:: Kan^R*	1
vps11Δ	*MAT***a**; *his3*; *leu2*; *met15*; *ura3*; *vps11:: Kan^R*	1
vps15Δ	*MAT***a**; *his3*; *leu2*; *met15*; *ura3*; *vps15:: Kan^R*	1
vps16Δ	*MAT***a**; *his3*; *leu2*; *met15*; *ura3*; *vps16:: Kan^R*	1
vps18Δ	*MAT***a**; *his3*; *leu2*; *met15*; *ura3*; *vps18:: Kan^R*	1
vps33Δ	*MAT***a**; *his3*; *leu2*; *met15*; *ura3*; *vps33:: Kan^R*	1
vps34Δ	*MAT***a**; *his3*; *leu2*; *met15*; *ura3*; *vps34:: Kan^R*	1
vps36Δ	*MAT***a**; *his3*; *leu2*; *met15*; *ura3*; *vps36:: Kan^R*	1
vps45Δ	*MAT***a**; *his3*; *leu2*; *met15*; *ura3*; *vps45:: Kan^R*	1
whi3Δ	*MAT***a**; *his3*; *leu2*; *met15*; *ura3*; *whi3:: Kan^R*	1
yel045cΔ	*MAT***a**; *his3*; *leu2*; *met15*; *ura3*; *yel045c:: Kan^R*	1
ykl118wΔ	*MAT***a**; *his3*; *leu2*; *met15*; *ura3*; *ykl118w:: Kan^R*	1
yor331cΔ	*MAT***a**; *his3*; *leu2*; *met15*; *ura3*; *yor331c:: Kan^R*	1
ypr099cΔ	*MAT***a**; *his3*; *leu2*; *met15*; *ura3*; *ypr099c:: Kan^R*	1
zap1Δ	*MAT***a**; *his3*; *leu2*; *met15*; *ura3*; *zap1:: Kan^R*	1
zds1Δ	*MAT***a**; *his3*; *leu2*; *met15*; *ura3*; *zds1:: Kan^R*	1
zuo1Δ	*MAT***a**; *his3*; *leu2*; *met15*; *ura3*; *zuo1:: Kan^R*	1

1. EUROSCARF. All strains are isogenic to BY4741.

Table S5 Strains used in chapter II.

Strain	Genotype	Source or reference
YPH499	*MAT***a** *ade2 his3 leu2 lys2 trp1 ura3*	1
YOC989	*MATα leu2 lys2 trp1 ura3 cls5-1*	2
YOC992	*MAT***a** *ade2 his3 leu2 lys2 trp1 ura3 pfy1::ADE2*	2
YOC4940	*MAT***a** *ade2 his3 leu2 lys2 trp1 ura3 bni1:: Kan^R*	This study
YOC5008	*MAT***a** *ade2 his3 leu2 lys2 trp1 ura3 bnr1:: Kan^R*	This study
YOC634	*MAT***a** *ade2 his3 leu2 lys2 trp1 ura3 bni1Δ (1228-1414)::HIS3 bnr1Δ (685-707)::TRP1*	3
YOC4939	*MAT***a** *his3 leu2 met15 ura3 bem1:: Kan^R*	4
YOC752	*MATα ade2 his3 lys2 leu2 trp1 ura3 ade3::rho1-2:LEU2 rho1::HIS3*	5
YOC4941	*MAT***a** *ade2 his3 leu2 lys2 trp1 ura3 cla4:: Kan^R*	This study
YOC138-1C	*MAT***a** *ade1 cls4-1*	6
YOC1417	*act1Δ1::LEU2 act1-101:HIS3*	7
YOC1419	*act1Δ1::LEU2 act1-111:HIS3*	7
YOC1420	*act1Δ1::LEU2 act1-113:HIS3*	7
YOC1421	*act1Δ1::LEU2 act1-119:HIS3*	7
YOC1422	*act1Δ1::LEU2 act1-120:HIS3*	7
YOC1424	*act1Δ1::LEU2 act1-125:HIS3*	7
YOC1425	*act1Δ1::LEU2 act1-129:HIS3*	7
YOC1426	*act1Δ1::LEU2 act1-132:HIS3*	7
YOC5009	*MAT***a** *ade2 his3 leu2 lys2 trp1 ura3 CDC24-GFP:HIS3MX6*	This study
YOC5010	*MAT***a** *his3 leu2 lys2 trp1 ura3 cls5-1 CDC24-GFP:HIS3MX6*	This study

1. Sikorski and Hieter (1989); 2. Takita, (1997); 3. Imamura *et al.*, (1997); 4. EUROSCARF; 5. Qadota *et al.*, (1996); 6. Ohya *et al.*, (1986a); 7. Wertman *et al.*, (1992)

Table S6 The models of the probability distributions and descriptions of the 209 parameters.

Parameter ID	Description	Distribution	Link function	Confounding factor
C13_A	Whole cell fitness for ellipse	Gamma	log[a]	Yes
D102_A	Distance between nuclear gravity center and mother tip	Gamma	log[a]	Yes
D117_A	Distance between nuclear gravity center and cell center	Gamma	log[a]	No
D127_A	Distance between nuclear brightest point and cell tip	Gamma	log[a]	Yes
D135_A	Distance between nuclear brightest point and cell center	Gamma	log[a]	No
D154_A	Angle between C1D1-1 and C1C1-2	Gamma	log[a]	Yes
D155_A	Angle between C1D2-1 and C1C1-2	Gamma	log[a]	Yes
C12-2_A1B	Bud cell outline length	Gamma	log[a]	No
C13_A1B	Mother cell fitness for ellipse	Gamma	log[a]	Yes
C103_A1B	Long axis length in mother	Gamma	log[a]	Yes
C107_A1B	Long axis length in bud	Gamma	log[a]	No
C109_A1B	Neck width	Gamma	log[a]	Yes
C114_A1B	Bud axis ratio	Gamma	log[a]	Yes
C116_A1B	Axis ratio ratio	Gamma	log[a]	Yes
A7-1_A1B	Size of actin region in mother	Gamma	log[a]	No
A7-2_A1B	Size of actin region in bud	Gamma	log[a]	Yes
D104_A1B	Distance between nuclear gravity center and mother tip	Gamma	log[a]	No
D118_A1B	Distance between nuclear gravity center and mother center	Gamma	log[a]	No
D126_A1B	Distance between nuclear gravity center and mother hip	Gamma	log[a]	No
D129_A1B	Distance between nuclear brightest point and mother tip	Gamma	log[a]	No
D132_A1B	Distance between nuclear brightest point and middle point of neck	Gamma	log[a]	Yes
D136_A1B	Distance between nuclear brightest point and mother center	Gamma	log[a]	No
D142_A1B	Distance between nuclear brightest point and mother hip	Gamma	log[a]	No
D145_A1B	Distance between nuclear outline point D7 and mother hip	Gamma	log[a]	No
D152_A1B	Mobility of nucleus in mother	Gamma	log[a]	Yes
D154_A1B	Angle between C1D1-1 and C1C1-2	Gamma	log[a]	Yes
D155_A1B	Angle between C1D2-1 and C1C1-2	Gamma	log[a]	Yes
D161_A1B	Angle between D3-1D4-1 and C1-1C1-2 or between D3-3D4-3 and C1-1C1-2	Gamma	log[a]	Yes
D165_A1B	Angle between D3-1D4-1 and C1C4-1 or between D3-3D4-3 and C1C4-1	Gamma	log[a]	No
D169_A1B	Angle between C4-1D1-1 and C4-1C1	Gamma	log[a]	No
D170_A1B	Angle between C4-1D2-1 and C4-1C1	Gamma	log[a]	Yes
C11-1_C	Mother cell size	Gamma	log[a]	Yes
C12-1_C	Mother cell outline length	Gamma	log[a]	Yes
C13_C	Mother cell fitness for ellipse	Gamma	log[a]	No
C103_C	Long axis length in mother	Gamma	log[a]	No
C105_C	Neck position	Gamma	log[a]	No
C106_C	Bud direction	Gamma	log[a]	No
C109_C	Neck width	Gamma	log[a]	No
C110_C	Distance between bud tip and mother long axis extension	Gamma	log[a]	Yes
C112_C	Distance between middle point of neck and mother center	Gamma	log[a]	Yes
C114_C	Bud axis ratio	Gamma	log[a]	No
C116_C	Axis ratio ratio	Gamma	log[a]	No
C128_C	Distance between middle point of neck and mother hip	Gamma	log[a]	No

continued on following page

Table S6—continued

Parameter ID	Description	Distribution	Link function	Confounding factor
D103_C	Distance between nuclear gravity center in mother and mother tip	Gamma	log[a]	No
D108_C	Distance between nuclear gravity center in mother and middle point of neck	Gamma	log[a]	Yes
D117_C	Distance between nuclear gravity center in mother and mother center	Gamma	log[a]	No
D119_C	Distance between nuclear gravity center in bud and bud center	Gamma	log[a]	No
D121_C	Distance between nuclear gravity center in bud and bud tip	Gamma	log[a]	Yes
D125_C	Distance between nuclear gravity center in mother and mother hip	Gamma	log[a]	No
D128_C	Distance between nuclear brightest point in mother and mother tip	Gamma	log[a]	No
D130_C	Distance between nuclear brightest point in mother and middle point of neck	Gamma	log[a]	Yes
D137_C	Distance between nuclear brightest point in bud and bud tip	Gamma	log[a]	No
D139_C	Distance between nuclear brightest point in bud and bud tip	Gamma	log[a]	Yes
D141_C	Distance between nuclear brightest point in mother and mother hip	Gamma	log[a]	No
D143_C	Distance between nuclear outline point D6-1 in mother and middle point of neck	Gamma	log[a]	No
D145_C	Distance between nuclear outline point D7 in mother and mother hip	Gamma	log[a]	No
D146_C	Distance between nuclear outline point D8 in bud and bud tip	Gamma	log[a]	No
D151_C	Ratio of distance between each nucleus and middle point of neck	Gamma	log[a]	No
D152_C	Mobility of nucleus in mother	Gamma	log[a]	No
D153_C	Mobility of nucleus in bud	Gamma	log[a]	No
D158_C	Angle between D1-1D1-2 and C1-1C1-2	Gamma	log[a]	No
D159_C	Angle between D2-1D2-2 and C1-1C1-2	Gamma	log[a]	No
D162_C	Angle between D1-1D1-2 and C1C4-1	Gamma	log[a]	No
D163_C	Angle between D2-1D2-2 and C1C4-1	Gamma	log[a]	No
D166_C	Angle between D1-1D1-2 and C4-1C4-2	Gamma	log[a]	Yes
D167_C	Angle between D2-1D2-2 and C4-1C4-2	Gamma	log[a]	Yes
D169_C	Angle between C4-1D1-1 and C4-1C1	Gamma	log[a]	No
D170_C	Angle between C4-1D2-1 and C4-1C1	Gamma	log[a]	Yes
A102_A1B	Bud actin region ratio to total region	Beta	logit[b]	No
A102_C	Bud actin region ratio to total region	Beta	logit[b]	No
A103_A1B	Relative distance of actin patch center from neck in mother	Beta	logit[b]	Yes
A103_C	Relative distance of actin patch center from neck in mother	Beta	logit[b]	No
A104_C	Relative distance of actin patch center from neck in bud	Zero-inflated beta	logit[b]	No
A9_C	Proportion of actin region at neck	Beta	logit[b]	No
C117_A1B	Cell outline ratio	Beta	logit[b]	Yes
C117_C	Cell outline ratio	Beta	logit[b]	Yes
C118_A1B	Cell size ratio	Beta	logit[b]	Yes
C118_C	Cell size ratio	Beta	logit[b]	Yes
D105_A	Ratio of D102 to C103	Beta	logit[b]	Yes
D106_C	Ratio of D103 to C103	Beta	logit[b]	No
D107_A1B	Ratio of D104 to C103	Beta	logit[b]	Yes
D112_C	Ratio of D108 to C128	Beta	logit[b]	Yes
D113_C	Ratio of D109 to C107	Beta	logit[b]	No
D114_A1B	Ratio of D110 to C128	Beta	logit[b]	Yes

continued on following page

Table S6—continued

Parameter ID	Description	Distribution	Link function	Confounding factor
D123_C	Ratio of D121 to C107	Beta	logit[b]	No
D147_A	Relative distance of nuclear gravity center to cell center	Beta	logit[b]	No
D147_A1B	Relative distance of nuclear gravity center to mother center	Beta	logit[b]	Yes
D147_C	Relative distance of nuclear gravity center in mother to mother center	Beta	logit[b]	No
D148_A	Relative distance of nuclear brightest point to cell center	Beta	logit[b]	No
D148_A1B	Relative distance of nuclear brightest point to mother center	Beta	logit[b]	Yes
D148_C	Relative distance of nuclear brightest point in mother to mother center	Beta	logit[b]	No
D149_C	Relative distance of nuclear gravity center in bud to bud center	Beta	logit[b]	Yes
D150_C	Relative distance of nuclear brightest point in bud to bud center	Beta	logit[b]	Yes
C115_A	Whole cell axis ratio	Beta	1/logit[c]	No
CCV11-1_A	Noise of C11-1 A	Gaussian	identity[d]	No
CCV12-1_A	Noise of C12-1 A	Gaussian	identity[d]	No
CCV13_A	Noise of C13 A	Gaussian	identity[d]	No
CCV103_A	Noise of C103 A	Gaussian	identity[d]	Yes
CCV104_A	Noise of C104 A	Gaussian	identity[d]	No
DCV102_A	Noise of D102 A	Gaussian	identity[d]	Yes
DCV117_A	Noise of D117 A	Gaussian	identity[d]	Yes
DCV127_A	Noise of D127 A	Gaussian	identity[d]	Yes
DCV135_A	Noise of D135 A	Gaussian	identity[d]	No
DCV147_A	Noise of D147 A	Gaussian	identity[d]	Yes
DCV148_A	Noise of D148 A	Gaussian	identity[d]	No
DCV182_A	Noise of D182 A	Gaussian	identity[d]	No
DCV188_A	Noise of D188 A	Gaussian	identity[d]	No
CCV11-1_A1B	Noise of C11-1 A1B	Gaussian	identity[d]	No
CCV12-1_A1B	Noise of C12-1 A1B	Gaussian	identity[d]	No
CCV13_A1B	Noise of C13 A1B	Gaussian	identity[d]	Yes
CCV101_A1B	Noise of C101 A1B	Gaussian	identity[d]	No
CCV102_A1B	Noise of C102 A1B	Gaussian	identity[d]	No
CCV103_A1B	Noise of C103 A1B	Gaussian	identity[d]	No
CCV104_A1B	Noise of C104 A1B	Gaussian	identity[d]	No
CCV105_A1B	Noise of C105 A1B	Gaussian	identity[d]	No
CCV106_A1B	Noise of C106 A1B	Gaussian	identity[d]	No
CCV110_A1B	Noise of C110 A1B	Gaussian	identity[d]	No
CCV112_A1B	Noise of C112 A1B	Gaussian	identity[d]	No
CCV114_A1B	Noise of C114 A1B	Gaussian	identity[d]	No
CCV116_A1B	Noise of C116 A1B	Gaussian	identity[d]	No
CCV126_A1B	Noise of C126 A1B	Gaussian	identity[d]	No
CCV128_A1B	Noise of C128 A1B	Gaussian	identity[d]	No
ACV7-2_A1B	Noise of A7-2 A1B	Gaussian	identity[d]	No
ACV8-1_A1B	Noise of A8-1 A1B	Gaussian	identity[d]	No
ACV8-2_A1B	Noise of A8-2 A1B	Gaussian	identity[d]	No
ACV101_A1B	Noise of A101 A1B	Gaussian	identity[d]	Yes

continued on following page

Table S6—continued

Parameter ID	Description	Distribution	Link function	Confounding factor
ACV102_A1B	Noise of A102 A1B	Gaussian	identity[d]	No
ACV122_A1B	Noise of A122 A1B	Gaussian	identity[d]	No
ACV123_A1B	Noise of A123 A1B	Gaussian	identity[d]	Yes
DCV104_A1B	Noise of D104 A1B	Gaussian	identity[d]	No
DCV107_A1B	Noise of D107 A1B	Gaussian	identity[d]	Yes
DCV110_A1B	Noise of D110 A1B	Gaussian	identity[d]	No
DCV114_A1B	Noise of D114 A1B	Gaussian	identity[d]	No
DCV126_A1B	Noise of D126 A1B	Gaussian	identity[d]	Yes
DCV129_A1B	Noise of D129 A1B	Gaussian	identity[d]	No
DCV132_A1B	Noise of D132 A1B	Gaussian	identity[d]	No
DCV142_A1B	Noise of D142 A1B	Gaussian	identity[d]	No
DCV143_A1B	Noise of D143 A1B	Gaussian	identity[d]	Yes
DCV145_A1B	Noise of D145 A1B	Gaussian	identity[d]	No
DCV152_A1B	Noise of D152 A1B	Gaussian	identity[d]	Yes
DCV161_A1B	Noise of D161 A1B	Gaussian	identity[d]	Yes
DCV165_A1B	Noise of D165 A1B	Gaussian	identity[d]	No
CCV11-1_C	Noise of C11-1 C	Gaussian	identity[d]	Yes
CCV12-1_C	Noise of C12-1 C	Gaussian	identity[d]	Yes
CCV12-2_C	Noise of C12-2 C	Gaussian	identity[d]	No
CCV13_C	Noise of C13 C	Gaussian	identity[d]	No
CCV101_C	Noise of C101 C	Gaussian	identity[d]	Yes
CCV103_C	Noise of C103 C	Gaussian	identity[d]	Yes
CCV104_C	Noise of C104 C	Gaussian	identity[d]	Yes
CCV105_C	Noise of C105 C	Gaussian	identity[d]	Yes
CCV107_C	Noise of C107 C	Gaussian	identity[d]	No
CCV108_C	Noise of C108 C	Gaussian	identity[d]	Yes
CCV110_C	Noise of C110 C	Gaussian	identity[d]	Yes
CCV116_C	Noise of C116 C	Gaussian	identity[d]	Yes
CCV117_C	Noise of C117 C	Gaussian	identity[d]	Yes
CCV118_C	Noise of C118 C	Gaussian	identity[d]	Yes
CCV127_C	Noise of C127 C	Gaussian	identity[d]	No
CCV128_C	Noise of C128 C	Gaussian	identity[d]	Yes
DCV17-1_C	Noise of D17-1 C	Gaussian	identity[d]	No
DCV108_C	Noise of D108 C	Gaussian	identity[d]	Yes
DCV109_C	Noise of D109 C	Gaussian	identity[d]	No
DCV112_C	Noise of D112 C	Gaussian	identity[d]	No
DCV116_C	Noise of D116 C	Gaussian	identity[d]	No
DCV117_C	Noise of D117 C	Gaussian	identity[d]	No
DCV119_C	Noise of D119 C	Gaussian	identity[d]	Yes
DCV121_C	Noise of D121 C	Gaussian	identity[d]	No
DCV123_C	Noise of D123 C	Gaussian	identity[d]	No
DCV128_C	Noise of D128 C	Gaussian	identity[d]	No
DCV130_C	Noise of D130 C	Gaussian	identity[d]	Yes
DCV131_C	Noise of D131 C	Gaussian	identity[d]	No

continued on following page

Table S6—continued

Parameter ID	Description	Distribution	Link function	Confounding factor
DCV135_C	Noise of D135 C	Gaussian	identity[d]	No
DCV139_C	Noise of D139 C	Gaussian	identity[d]	No
DCV141_C	Noise of D141 C	Gaussian	identity[d]	No
DCV146_C	Noise of D146 C	Gaussian	identity[d]	Yes
DCV148_C	Noise of D148 C	Gaussian	identity[d]	No
DCV153_C	Noise of D153 C	Gaussian	identity[d]	No
DCV157_C	Noise of D157 C	Gaussian	identity[d]	No
DCV159_C	Noise of D159 C	Gaussian	identity[d]	No
C123_A1B	Small bud ratio	Beta-binomial	logit[b]	No
C124_A1B	Medium bud ratio	Beta-binomial	logit[b]	No
C125_A1B	Large bud ratio	Beta-binomial	logit[b]	Yes
A107_A1B	Actin c ratio	Beta-binomial	logit[b]	Yes
A108_A1B	Actin d ratio	Beta-binomial	logit[b]	No
A109_A1B	Actin e ratio	Beta-binomial	logit[b]	Yes
A112_A1B	Actin cd ratio	Beta-binomial	logit[b]	Yes
A113_A1B	Actin n ratio	Binomial	logit[b]	No
C123_C	Small bud ratio	Binomial	logit[b]	No
C124_C	Medium bud ratio	Beta-binomial	logit[b]	No
C125_C	Large bud ratio	Beta-binomial	logit[b]	No
A109_C	Actin e ratio	Beta-binomial	logit[b]	No
A110_C	Actin f ratio	Beta-binomial	logit[b]	No
C120	small bud ratio	Beta-binomial	logit[b]	Yes
C121	medium bud ratio	Beta-binomial	logit[b]	Yes
C122	large bud ratio	Beta-binomial	logit[b]	Yes
C123	small bud ratio to budded cells	Beta-binomial	logit[b]	No
C124	medium bud ratio to buded cells	Beta-binomial	logit[b]	No
C125	large bud ratio to buded cells	Beta-binomial	logit[b]	No
A107	actin c ratio	Beta-binomial	logit[b]	Yes
A108	actin d ratio	Beta-binomial	logit[b]	Yes
A109	actin e ratio	Beta-binomial	logit[b]	No
A110	actin f ratio	Beta-binomial	logit[b]	No

continued on following page

Table S6—continued

Parameter ID	Description	Distribution	Link function	Confounding factor
A116	actin c ratio to budded cells	Beta-binomial	logit[b]	No
A117	actin d ratio to budded cells	Beta-binomial	logit[b]	No
A118	actin e ratio to budded cells	Beta-binomial	logit[b]	No
A119	actin f ratio to budded cells	Beta-binomial	logit[b]	No
D202	nuclear C ratio	Beta-binomial	logit[b]	Yes
D205	nuclear F ratio	Beta-binomial	logit[b]	Yes
D210	nuclear A ratio to nuclear AA1BC cells	Beta-binomial	logit[b]	Yes
D213	nuclear C ratio to nuclear AA1BC cells	Beta-binomial	logit[b]	Yes

[a]log is defined as $\eta(y) = \log(y)$

[b]logit is defined as $\eta(y) = \text{logit}(y) = \log(y) - \log(1-y)$

[c]1/logit is defined as $\eta(y) = \text{logit}(1/y)$

[d]identity is defined as $\eta(y) = y$

Table S7 The models of the probability distributions and descriptions of the 247 parameters.

Parameter ID	Description	Distribution	Link function	Confounding factor
C11-1_A	Whole cell size	Gamma	log[a]	No
C12-1_A	Whole cell outline length	Gamma	log[a]	No
C13_A	Whole cell fitness for ellipse	Gamma	log[a]	No
C103_A	Long axis length in whole cell	Gamma	log[a]	No
C104_A	Short axis length in whole cell	Gamma	log[a]	No
C126_A	Brightness difference of cell wall	Gamma	log[a]	No
C127_A	Thickness difference of cell wall	Gamma	log[a]	No
A7-1_A	Size of actin region	Gamma	log[a]	No
A8-1_A	Actin region brightness	Gamma	log[a]	No
A120_A	Total length of actin patch link	Gamma	log[a]	No
A121_A	Maximal distance between patches	Gamma	log[a]	No
A122_A	Number of bright actin patches	Gamma	log[a]	No
D14-1_A	Nuclear size	Gamma	log[a]	No
D15-1_A	Nuclear brightness	Gamma	log[a]	No
D17-1_A	Nuclear fitness for ellipse	Gamma	log[a]	No
D102_A	Distance between nuclear gravity center and mother tip	Gamma	log[a]	No
D117_A	Distance between nuclear gravity center and cell center	Gamma	log[a]	No
D127_A	Distance between nuclear brightest point and cell tip	Gamma	log[a]	No
D135_A	Distance between nuclear brightest point and cell center	Gamma	log[a]	No
D154_A	Angle between C1D1-1 and C1C1-2	Gamma	log[a]	No
D155_A	Angle between C1D2-1 and C1C1-2	Gamma	log[a]	No
D173_A	Maximal distance between nuclear gravity center and nuclear outline	Gamma	log[a]	No
D176_A	Nuclear long axis length	Gamma	log[a]	No
D188_A	Distance between nuclear gravity center and brightest point	Gamma	log[a]	No
D191_A	Average of nuclear brightness	Gamma	log[a]	No
C11-1_A1B	Mother cell size	Gamma	log[a]	No
C12-1_A1B	Mother cell outline length	Gamma	log[a]	No
C13_A1B	Mother cell fitness for ellipse	Gamma	log[a]	No
C101_A1B	Whole cell size	Gamma	log[a]	No
C102_A1B	Whole cell outline length	Gamma	log[a]	No
C103_A1B	Long axis length in mother	Gamma	log[a]	No
C104_A1B	Short axis length in mother	Gamma	log[a]	No
C105_A1B	Neck position	Gamma	log[a]	No
C106_A1B	Bud direction	Gamma	log[a]	No
C107_A1B	Long axis length in bud	Gamma	log[a]	No
C108_A1B	Short axis length in bud	Gamma	log[a]	No
C109_A1B	Neck width	Gamma	log[a]	No
C110_A1B	Distance between bud tip and mother long axis extension	Gamma	log[a]	No
C111_A1B	Distance between bud tip and mother short axis extension	Gamma	log[a]	No
C112_A1B	Distance between middle point of neck and mother center	Gamma	log[a]	No
C113_A1B	Distance between bud tip and mother long axis through middle point of neck	Gamma	log[a]	No
C114_A1B	Bud axis ratio	Gamma	log[a]	No
C116_A1B	Axis ratio ratio	Gamma	log[a]	No

continued on following page

Table S7—continued

Parameter ID	Description	Distribution	Link function	Confounding factor
C128_A1B	Distance between middle point of neck and mother hip	Gamma	log[a]	No
A7-1_A1B	Size of actin region in mother	Gamma	log[a]	No
A7-2_A1B	Size of actin region in bud	Gamma	log[a]	No
A8-1_A1B	Total brightness of actin region in mother	Gamma	log[a]	No
A8-2_A1B	Total brightness of actin region in bud	Gamma	log[a]	No
A120_A1B	Total length of actin patch link	Gamma	log[a]	No
A121_A1B	Maximal distance between patches	Gamma	log[a]	No
A122_A1B	Number of bright actin patches	Gamma	log[a]	No
A123_A1B	Ratio of actin patches to actin region	Gamma	log[a]	No
D14-3_A1B	Nuclear size	Gamma	log[a]	No
D15-3_A1B	Nuclear brightness	Gamma	log[a]	No
D104_A1B	Distance between nuclear gravity center and mother tip	Gamma	log[a]	No
D110_A1B	Distance between nuclear gravity center and middle point of neck	Gamma	log[a]	No
D118_A1B	Distance between nuclear gravity center and mother center	Gamma	log[a]	No
D126_A1B	Distance between nuclear gravity center and mother hip	Gamma	log[a]	No
D129_A1B	Distance between nuclear brightest point and mother tip	Gamma	log[a]	No
D132_A1B	Distance between nuclear brightest point and middle point of neck	Gamma	log[a]	No
D136_A1B	Distance between nuclear brightest point and mother center	Gamma	log[a]	No
D142_A1B	Distance between nuclear brightest point and mother hip	Gamma	log[a]	No
D143_A1B	Distance between nuclear outline point D6-1 and middle point of neck	Gamma	log[a]	No
D145_A1B	Distance between nuclear outline point D7 and mother hip	Gamma	log[a]	No
D152_A1B	Mobility of nucleus in mother	Gamma	log[a]	No
D154_A1B	Angle between C1D1-1 and C1C1-2	Gamma	log[a]	No
D170_A1B	Angle between C4-1D2-1 and C4-1C1	Gamma	log[a]	No
D175_A1B	Maximal distance between nuclear gravity center and nuclear outline	Gamma	log[a]	No
D178_A1B	Nuclear long axis length	Gamma	log[a]	No
D181_A1B	Nuclear short axis length	Gamma	log[a]	No
D190_A1B	Distance between nuclear gravity center and brightest point	Gamma	log[a]	No
C11-1_C	Mother cell size	Gamma	log[a]	No
C11-2_C	Bud cell size	Gamma	log[a]	No
C12-1_C	Mother cell outline length	Gamma	log[a]	No
C12-2_C	Bud cell outline length	Gamma	log[a]	No
C101_C	Whole cell size	Gamma	log[a]	No
C102_C	Whole cell outline length	Gamma	log[a]	No
C103_C	Long axis length in mother	Gamma	log[a]	No
C104_C	Short axis length in mother	Gamma	log[a]	No
C107_C	Long axis length in bud	Gamma	log[a]	No
C108_C	Short axis length in bud	Gamma	log[a]	No
C109_C	Neck width	Gamma	log[a]	No
C111_C	Distance between bud tip and mother short axis extension	Gamma	log[a]	No
C112_C	Distance between middle point of neck and mother center	Gamma	log[a]	No
C113_C	Distance between bud tip and mother long axis through middle point of neck	Gamma	log[a]	No
C126_C	Brightness difference of cell wall	Gamma	log[a]	No

continued on following page

Table S7—continued

Parameter ID	Description	Distribution	Link function	Confounding factor
C128_C	Distance between middle point of neck and mother hip	Gamma	log[a]	No
A7-1_C	Size of actin region in mother	Gamma	log[a]	No
A8-1_C	Total brightness of actin region in mother	Gamma	log[a]	No
A120_C	Total length of actin patch link	Gamma	log[a]	No
A121_C	Maximal distance between patches	Gamma	log[a]	No
D14-2_C	Nuclear size in bud	Gamma	log[a]	No
D15-1_C	Nuclear brightness in mother	Gamma	log[a]	No
D15-2_C	Nuclear brightness in bud	Gamma	log[a]	No
D15-3_C	Nuclear brightness in whole cell	Gamma	log[a]	No
D17-2_C	Nuclear fitness for ellipse in bud	Gamma	log[a]	No
D103_C	Distance between nuclear gravity center in mother and mother tip	Gamma	log[a]	No
D116_C	Distance between two nuclear gravity centers	Gamma	log[a]	No
D121_C	Distance between nuclear gravity center in bud and bud tip	Gamma	log[a]	No
D125_C	Distance between nuclear gravity center in mother and mother hip	Gamma	log[a]	No
D128_C	Distance between nuclear brightest point in mother and mother tip	Gamma	log[a]	No
D130_C	Distance between nuclear brightest point in mother and middle point of neck	Gamma	log[a]	No
D131_C	Distance between nuclear brightest point in bud and middle point of neck	Gamma	log[a]	No
D134_C	Distance between two nuclear brightest points	Gamma	log[a]	No
D139_C	Distance between nuclear brightest point in bud and bud tip	Gamma	log[a]	No
D141_C	Distance between nuclear brightest point in mother and mother hip	Gamma	log[a]	No
D145_C	Distance between nuclear outline point D7 in mother and mother hip	Gamma	log[a]	No
D169_C	Angle between C4-1D1-1 and C4-1C1	Gamma	log[a]	No
D170_C	Angle between C4-1D2-1 and C4-1C1	Gamma	log[a]	No
D174_C	Maximal distance between nuclear gravity center and nuclear outline in bud	Gamma	log[a]	No
D177_C	Nuclear long axis length in bud	Gamma	log[a]	No
D180_C	Nuclear short axis length in bud	Gamma	log[a]	No
D185_C	Relative distance of two nuclear gravity centers to middle point of neck	Gamma	log[a]	No
D186_C	Relative distance of two nuclear brightest points to middle point of neck	Gamma	log[a]	No
A101_A	Actin region ratio in whole cell	Beta	logit[b]	No
A102_A1B	Bud actin region ratio to total region	Beta	logit[b]	No
A102_C	Bud actin region ratio to total region	Beta	logit[b]	No
A104_A1B	Relative distance of actin patch center from neck in bud	Zero-inflated beta	logit[b]	No
A104_C	Relative distance of actin patch center from neck in bud	Zero-inflated beta	logit[b]	No
C117_C	Cell outline ratio	Beta	logit[b]	No
C118_A1B	Cell size ratio	Beta	logit[b]	No
D105_A	Ratio of D102 to C103	Beta	logit[b]	No
D107_A1B	Ratio of D104 to C103	Beta	logit[b]	No
D114_A1B	Ratio of D110 to C128	Beta	logit[b]	No
D147_A	Relative distance of nuclear gravity center to cell center	Beta	logit[b]	No

continued on following page

Table S7—continued

Parameter ID	Description	Distribution	Link function	Confounding factor
D147_A1B	Relative distance of nuclear gravity center to mother center	Beta	logit[b]	No
D147_C	Relative distance of nuclear gravity center in mother to mother center	Beta	logit[b]	No
D148_A	Relative distance of nuclear brightest point to cell center	Beta	logit[b]	No
D148_A1B	Relative distance of nuclear brightest point to mother center	Beta	logit[b]	No
D148_C	Relative distance of nuclear brightest point in mother to mother center	Beta	logit[b]	No
D182_A	Nuclear axis ratio	Beta	2/logit[c]	No
D184_A1B	Nuclear axis ratio	Beta	2/logit[c]	No
C115_A	Whole cell axis ratio	Beta	1/logit[d]	No
C115_C	Mother axis ratio	Beta	1/logit[d]	No
CCV11-1_A	Noise of C11-1 A	Gaussian	identity[e]	No
CCV12-1_A	Noise of C12-1 A	Gaussian	identity[e]	No
CCV13_A	Noise of C13 A	Gaussian	identity[e]	No
CCV103_A	Noise of C103 A	Gaussian	identity[e]	No
CCV104_A	Noise of C104 A	Gaussian	identity[e]	No
CCV115_A	Noise of C115 A	Gaussian	identity[e]	No
ACV7-1_A	Noise of A7-1 A	Gaussian	identity[e]	No
ACV101_A	Noise of A101 A	Gaussian	identity[e]	No
ACV120_A	Noise of A120 A	Gaussian	identity[e]	No
ACV121_A	Noise of A121 A	Gaussian	identity[e]	No
ACV122_A	Noise of A122 A	Gaussian	identity[e]	No
ACV123_A	Noise of A123 A	Gaussian	identity[e]	No
DCV14-1_A	Noise of D14-1 A	Gaussian	identity[e]	No
DCV15-1_A	Noise of D15-1 A	Gaussian	identity[e]	No
DCV16-1_A	Noise of D16-1 A	Gaussian	identity[e]	No
DCV102_A	Noise of D102 A	Gaussian	identity[e]	No
DCV105_A	Noise of D105 A	Gaussian	identity[e]	No
DCV127_A	Noise of D127 A	Gaussian	identity[e]	No
DCV173_A	Noise of D173 A	Gaussian	identity[e]	No
DCV176_A	Noise of D176 A	Gaussian	identity[e]	No
DCV179_A	Noise of D179 A	Gaussian	identity[e]	No
DCV191_A	Noise of D191 A	Gaussian	identity[e]	No
DCV194_A	Noise of D194 A	Gaussian	identity[e]	No
CCV11-1_A1B	Noise of C11-1 A1B	Gaussian	identity[e]	No
CCV12-1_A1B	Noise of C12-1 A1B	Gaussian	identity[e]	No
CCV12-2_A1B	Noise of C12-2 A1B	Gaussian	identity[e]	No
CCV13_A1B	Noise of C13 A1B	Gaussian	identity[e]	No
CCV101_A1B	Noise of C101 A1B	Gaussian	identity[e]	No
CCV102_A1B	Noise of C102 A1B	Gaussian	identity[e]	No
CCV103_A1B	Noise of C103 A1B	Gaussian	identity[e]	No
CCV104_A1B	Noise of C104 A1B	Gaussian	identity[e]	No
CCV105_A1B	Noise of C105 A1B	Gaussian	identity[e]	No

continued on following page

Table S7—continued

Parameter ID	Description	Distribution	Link function	Confounding factor
CCV108_A1B	Noise of C108 A1B	Gaussian	identity[e]	No
CCV110_A1B	Noise of C110 A1B	Gaussian	identity[e]	No
CCV112_A1B	Noise of C112 A1B	Gaussian	identity[e]	No
CCV115_A1B	Noise of C115 A1B	Gaussian	identity[e]	No
CCV116_A1B	Noise of C116 A1B	Gaussian	identity[e]	No
CCV117_A1B	Noise of C117 A1B	Gaussian	identity[e]	No
CCV118_A1B	Noise of C118 A1B	Gaussian	identity[e]	No
CCV126_A1B	Noise of C126 A1B	Gaussian	identity[e]	No
CCV127_A1B	Noise of C127 A1B	Gaussian	identity[e]	No
CCV128_A1B	Noise of C128 A1B	Gaussian	identity[e]	No
ACV7-1_A1B	Noise of A7-1 A1B	Gaussian	identity[e]	No
ACV8-1_A1B	Noise of A8-1 A1B	Gaussian	identity[e]	No
ACV102_A1B	Noise of A102 A1B	Gaussian	identity[e]	No
ACV120_A1B	Noise of A120 A1B	Gaussian	identity[e]	No
ACV121_A1B	Noise of A121 A1B	Gaussian	identity[e]	No
ACV122_A1B	Noise of A122 A1B	Gaussian	identity[e]	No
DCV14-3_A1B	Noise of D14-3 A1B	Gaussian	identity[e]	No
DCV15-3_A1B	Noise of D15-3 A1B	Gaussian	identity[e]	No
DCV17-3_A1B	Noise of D17-3 A1B	Gaussian	identity[e]	No
DCV104_A1B	Noise of D104 A1B	Gaussian	identity[e]	No
DCV107_A1B	Noise of D107 A1B	Gaussian	identity[e]	No
DCV110_A1B	Noise of D110 A1B	Gaussian	identity[e]	No
DCV126_A1B	Noise of D126 A1B	Gaussian	identity[e]	No
DCV132_A1B	Noise of D132 A1B	Gaussian	identity[e]	No
DCV143_A1B	Noise of D143 A1B	Gaussian	identity[e]	No
DCV152_A1B	Noise of D152 A1B	Gaussian	identity[e]	No
DCV154_A1B	Noise of D154 A1B	Gaussian	identity[e]	No
DCV172_A1B	Noise of D172 A1B	Gaussian	identity[e]	No
DCV184_A1B	Noise of D184 A1B	Gaussian	identity[e]	No
DCV190_A1B	Noise of D190 A1B	Gaussian	identity[e]	No
DCV196_A1B	Noise of D196 A1B	Gaussian	identity[e]	No
A105_A	Actin a ratio	Beta-binomial	logit[b]	No
A106_A	Actin b ratio	Beta-binomial	logit[b]	No
A113_A	Actin n ratio	Binomial	logit[b]	No
C123_A1B	Small bud ratio	Binomial	logit[b]	No
C124_A1B	Medium bud ratio	Binomial	logit[b]	No
A107_A1B	Actin c ratio	Binomial	logit[b]	No
A108_A1B	Actin d ratio	Beta-binomial	logit[b]	No
A109_A1B	Actin e ratio	Beta-binomial	logit[b]	No

continued on following page

Table S7—continued

Parameter ID	Description	Distribution	Link function	Confounding factor
A112_A1B	Actin cd ratio	Beta-binomial	logit[b]	No
C124_C	Medium bud ratio	Binomial	logit[b]	No
A107_C	Actin c ratio	Binomial	logit[b]	No
A108_C	Actin d ratio	Binomial	logit[b]	No
A109_C	Actin e ratio	Binomial	logit[b]	No
A112_C	Actin cd ratio	Binomial	logit[b]	No
C119	no bud ratio	Beta-binomial	logit[b]	No
C120	small bud ratio	Beta-binomial	logit[b]	No
C121	medium bud ratio	Beta-binomial	logit[b]	No
C122	large bud ratio	Beta-binomial	logit[b]	No
C123	small bud ratio to budded cells	Beta-binomial	logit[b]	No
C124	medium bud ratio to buded cells	Binomial	logit[b]	No
A105	actin a ratio	Beta-binomial	logit[b]	No
A106	actin b ratio	Beta-binomial	logit[b]	No
A107	actin c ratio	Beta-binomial	logit[b]	No
A108	actin d ratio	Beta-binomial	logit[b]	No
A109	actin e ratio	Beta-binomial	logit[b]	No
A110	actin f ratio	Binomial	logit[b]	No
A111	actin ae ratio	Beta-binomial	logit[b]	No
A112	actin bcd ratio	Beta-binomial	logit[b]	No
A114	actin a ratio to no bud cells	Beta-binomial	logit[b]	No
A115	actin b ratio to no bud cells	Beta-binomial	logit[b]	No
A116	actin c ratio to budded cells	Beta-binomial	logit[b]	No
A117	actin d ratio to budded cells	Beta-binomial	logit[b]	No
A118	actin e ratio to budded cells	Beta-binomial	logit[b]	No
D199	nuclear A ratio	Beta-binomial	logit[b]	No
D200	nuclear A1 ratio	Beta-binomial	logit[b]	No
D201	nuclear B ratio	Binomial	logit[b]	No
D202	nuclear C ratio	Beta-binomial	logit[b]	No
D203	nuclear D ratio	Beta-binomial	logit[b]	No

continued on following page

Table S7—continued

Parameter ID	Description	Distribution	Link function	Confounding factor
D204	nuclear E ratio	Beta-binomial	logit[b]	No
D206	nuclear A ratio to no bud cells	Beta-binomial	logit[b]	No
D207	nuclear A1 ratio to budded cells	Beta-binomial	logit[b]	No
D208	nuclear B ratio to budded cells	Binomial	logit[b]	No
D209	nuclear C ratio to budded cells	Beta-binomial	logit[b]	No
D210	nuclear A ratio to nuclear AA1BC cells	Beta-binomial	logit[b]	No
D211	nuclear A1 ratio to nuclear AA1BC cells	Beta-binomial	logit[b]	No
D212	nuclear B ratio to nuclear AA1BC cells	Binomial	logit[b]	No
D213	nuclear C ratio to nuclear AA1BC cells	Beta-binomial	logit[b]	No
D214	nuclear A1 ratio to nuclear A1BC cells	Binomial	logit[b]	No
D215	nuclear B ratio to nuclear A1BC cells	Binomial	logit[b]	No
D216	nuclear C ratio to nuclear A1BC cells	Beta-binomial	logit[b]	No

[a]log is defined as $\eta(y) = \log(y)$

[b]logit is defined as $\eta(y) = \text{logit}(y) = \log(y) - \log(1-y)$

[c]2/logit is defined as $\eta(y) = \text{logit}(2/y)$

[d]1/logit is defined as $\eta(y) = \text{logit}(1/y)$

[d]identity is defined as $\eta(y) = y$

References

Akaike, H. (1998). Information Theory and an Extension of the Maximum Likelihood Principle. In: Selected Papers of Hirotugu Akaike, ed. E. Parzen, K. Tanabe, and G. Kitagawa, Springer New York, pp 199–213.

Amberg, D. C., Basart, E., and Botstein, D. (1995). Defining protein interactions with yeast actin in vivo. Nat. Struct. Biol. *2*, 28–35.

Bachhawat, A. K., Manolson, M. F., Murdock, D. G., Garman, J. D., and Jones, E. W. (1993). The *VPH2* gene encodes a 25 kDa protein required for activity of the yeast vacuolar H^+-ATPase. Yeast *9*, 175–184.

Balderhaar, H. J. K., and Ungermann, C. (2013). CORVET and HOPS tethering complexes - coordinators of endosome and lysosome fusion. J. Cell Sci. *126*, 1307–1316.

Baryshnikova, A., Costanzo, M., Myers, C. L., Andrews, B., and Boone, C. (2013). Genetic Interaction Networks : Toward an Understanding of Heritability. Annu. Rev. Genomics Hum. Genet. *14*, 111–133.

Beeler, T., Gable, K., Zhao, C., and Dunn, T. (1994). A novel protein, CSG2p, is required for Ca^{2+} regulation in *Saccharomyces cerevisiae*. J. Biol. Chem. *269*, 7279–7284.

Ben-Aroya, S., Coombes, C., Kwok, T., O'Donnell, K. A., Boeke, J. D., and Hieter, P. (2008). Toward a comprehensive temperature-sensitive mutant repository of the essential genes of *Saccharomyces cerevisiae*. Mol. Cell *30*, 248–258.

Berridge, M. J., Bootman, M. D., and Roderick, H. L. (2003). Calcium signalling : dynamics, homeostasis and remodelling. Nat. Rev. Mol. Cell Biol. *4*, 517-529

Bose, I., Irazoqui, J. E., Moskow, J. J., Bardes, E. S., Zyla, T. R., and Lew, D. J. (2001). Assembly of scaffold-mediated complexes containing Cdc42p, the exchange factor Cdc24p, and the effector Cla4p required for cell cycle-regulated phosphorylation of Cdc24p. J. Biol. Chem. *276*, 7176–7186.

Chang, Y., Schlenstedt, G., Flockerzi, V., and Beck, A. (2010). Properties of the intracellular transient receptor potential (TRP) channel in yeast, Yvc1. FEBS Lett. *584*, 2028–2032.

Costanzo, M. *et al.* (2010). The genetic landscape of a cell. Science *327*, 425–431.

Cui, J., and Kaandorp, J. A. (2006). Mathematical modeling of calcium homeostasis in yeast cells. Cell Calcium *39*, 337–348.

Cui, J., Kaandorp, J. A., Ositelu, O. O., Beaudry, V., Knight, A., Nanfack, Y. F., and Cunningham, K. W. (2009). Simulating calcium influx and free calcium concentrations in yeast. Cell Calcium *45*, 123–132.

Cunningham, K. W. (2011). Acidic calcium stores of *Saccharomyces cerevisiae*. Cell Calcium *50*, 129–138.

Cunningham, K. W., and Fink, G. R. (1994). Calcineurin-dependent growth control in *Saccharomyces cerevisiae* mutants lacking *PMC1*, a homolog of plasma membrane Ca^{2+} ATPases. J. Cell Biol. *124*, 351–363.

Cunningham, K. W., and Fink, G. R. (1996). Calcineurin inhibits *VCX1*-dependent H^{+}/Ca^{2+} exchange and induces Ca^{2+} ATPases in *Saccharomyces cerevisiae*. Mol. Cell. Biol. *16*, 2226–2237.

Cyert, M. S. (2001). Genetic analysis of calmodulin and its targets in *Saccharomyces cerevisiae*. Annu. Rev. Genet. *35*, 647–672.

Cyert, M. S. (2003). Calcineurin signaling in *Saccharomyces cerevisiae*: how yeast go crazy in response to stress. Biochem. Biophys. Res. Commun. *311*, 1143–1150.

Cyert, M. S., and Philpott, C. C. (2013). Regulation of cation balance in *Saccharomyces cerevisiae*. Genetics *193*, 677–713.

Demaurex, N., and Frieden, M. (2003). Measurements of the free luminal ER Ca^{2+} concentration with targeted "cameleon" fluorescent proteins. Cell Calcium *34*, 109–119.

Denis, V., and Cyert, M. S. (2002). Internal Ca^{2+} release in yeast is triggered by hypertonic shock and mediated by a TRP channel homologue. J. Cell Biol. *156*, 29–34.

Dixon, S. J., Costanzo, M., Baryshnikova, A., Andrews, B., and Boone, C. (2009). Systematic mapping of genetic interaction networks. Annu. Rev. Genet. *43*, 601–625.

Dunn, T., Gable, K., and Beeler, T. (1994). Regulation of cellular Ca^{2+} by yeast vacuoles. J. Biol. Chem. *269*, 7273–7278.

Eilam, Y. (1982). Studies on calcium efflux in the yeast *Saccharomyces cerevisiae*. Microbios *35*, 99–110.

Eilam, Y., Lavi, H., and Grossowicz, N. (1985). Cytoplasmic Ca^{2+} Homeostasis Maintained by a Vacuolar Ca^{2+} Transport System in the Yeast *Saccharomyces cerevisiae*. Microbiology *131*, 623–629.

Fischer, M., Schnell, N., Chattaway, J., Davies, P., Dixon, G., and Sanders, D. (1997). The *Saccharomyces cerevisiae CCH1* gene is involved in calcium influx and mating. FEBS Lett. *419*, 259–262.

Forster, C., and Kane, P. M. (2000). Cytosolic Ca^{2+} homeostasis is a constitutive function of the V-ATPase in *Saccharomyces cerevisiae*. J. Biol. Chem. *275*, 38245–38253.

Fujimura-Kamada, K., Hirai, T., and Tanaka, K. (2012). Essential role of the NH2-terminal region of Cdc24 guanine nucleotide exchange factor in its initial polarized localization in *Saccharomyces cerevisiae*. Eukaryot. Cell *11*, 2–15.

Haarer, B., and Brown, S. (1990). Structure and function of profilin. Cell Motil. Cytoskeleton *74*, 71–74.

Haarer, B. K., Corbett, A., Kweon, Y., Petzold, A. S., Silver, P., and Brown, S. S. (1996). *SEC3* mutations are synthetically lethal with profilin mutations and cause defects in diploid-specific bud-site selection. Genetics *144*, 495–510.

Haarer, B. K., Lillie, S. H., Adams, A. E., Magdolen, V., Bandlow, W., and Brown, S. S. (1990). Purification of profilin from *Saccharomyces cerevisiae* and analysis of profilin-deficient cells. J. Cell Biol. *110*, 105–114.

Halachmi, D., and Eilam, Y. (1993). Calcium homeostasis in yeast cells exposed to high concentrations of calcium. Roles of vacuolar H^+-ATPase and cellular ATP. FEBS Lett. *316*, 73–78.

Heitman, J., Movva, N. R., Hiestand, P. C., and Hall, M. N. (1991). FK506-binding protein proline rotamase is a target for the immunosuppressive agent FK506 in *Saccharomyces cerevisiae*. Proc. Natl. Acad. Sci. U. S. A. *88*, 1948–1952.

Hirata, R., Umemoto, N., Ho, M. N., Ohya, Y., Stevens, T. H., and Anraku, Y. (1993). *VMA12* is essential for assembly of the vacuolar H^+-ATPase subunits onto the vacuolar membrane in *Saccharomyces cerevisiae*. J. Biol. Chem. *268*, 961–967.

Ho, M. N., Hirata, R., Umemoto, N., Ohya, Y., Takatsuki, a, Stevens, T. H., and Anraku, Y. (1993). *VMA13* encodes a 54-kDa vacuolar H^+-ATPase subunit required for activity but not

assembly of the enzyme complex in *Saccharomyces cerevisiae*. J. Biol. Chem. *268*, 18286–18292.

Idrissi, F.-Z., Wolf, B. L., and Geli, M. I. (2002). Cofilin, but not profilin, is required for myosin-I-induced actin polymerization and the endocytic uptake in yeast. Mol. Biol. Cell *13*, 4074–4087.

Iida, H., Nakamura, H., Ono, T., Okumura, M. S., and Anraku, Y. (1994). *MID1*, a novel *Saccharomyces cerevisiae* gene encoding a plasma membrane protein, is required for Ca^{2+} influx and mating. Mol. Cell. Biol. *14*, 8259–8271.

Imamura, H., Tanaka, K., Hihara, T., Umikawa, M., Kamei, T., Takahashi, K., Sasaki, T., and Takai, Y. (1997). Bni1p and Bnr1p: downstream targets of the Rho family small G-proteins which interact with profilin and regulate actin cytoskeleton in *Saccharomyces cerevisiae*. EMBO J. *16*, 2745–2755.

Iwaki, A., Ohnuki, S., Suga, Y., Izawa, S., and Ohya, Y. (2013). Vanillin inhibits translation and induces messenger ribonucleoprotein (mRNP) granule formation in *Saccharomyces cerevisiae*: application and validation of high-content, image-based profiling. PLoS One *8*, e61748.

Jin, K. *et al.* (2012). PhenoM: a database of morphological phenotypes caused by mutation of essential genes in *Saccharomyces cerevisiae*. Nucleic Acids Res. *40*, D687–D694.

Jonikas, M. C. *et al.* (2009). Comprehensive characterization of genes required for protein folding in the endoplasmic reticulum. Science *323*, 1693–1697.

Kamei, T., Tanaka, K., Hihara, T., Umikawa, M., Imamura, H., Kikyo, M., Ozaki, K., and Takai, Y. (1998). Interaction of Bnr1p with a novel Src homology 3 domain-containing Hof1p. Implication in cytokinesis in *Saccharomyces cerevisiae*. J. Biol. Chem. *273*, 28341–28345.

Kane, P. M. (2006). The where, when, and how of organelle acidification by the yeast vacuolar H^+-ATPase. Microbiol. Mol. Biol. Rev. *70*, 177–191.

Kwok, E. Y., Severance, S., and Kosman, D. J. (2006). Evidence for iron channeling in the Fet3p-Ftr1p high-affinity iron uptake complex in the yeast plasma membrane. Biochemistry *45*, 6317–6327.

Lemmon, M. A. (2008). Membrane recognition by phospholipid-binding domains. Nat. Rev. Mol. Cell Biol. *9*, 99–111.

Levy, S. F., and Siegal, M. L. (2008). Network hubs buffer environmental variation in *Saccharomyces cerevisiae*. PLoS Biol. *6*, e264.

Li, Z. *et al.* (2011). Systematic exploration of essential yeast gene function with temperature-sensitive mutants. Nat. Biotechnol. *29*, 361–367.

Longtine, M. S., Iii, A. M. K., Demarini, D. J., and Shah, N. G. (1998). Additional Modules for Versatile and Economical PCR-based Gene Deletion and Modification in *Saccharomyces cerevisiae*. *961*, 953–961.

Mani, R., St Onge, R. P., Hartman, J. L., Giaever, G., and Roth, F. P. (2008). Defining genetic interaction. Proc. Natl. Acad. Sci. U. S. A. *105*, 3461–3466.

Marcoux, N., Bourbonnais, Y., Charest, P. M., and Pallotta, D. (1998). Overexpression of *MID2* suppresses the profilin-deficient phenotype of yeast cells. Mol. Microbiol. *29*, 515–526.

Martin, D. C., Kim, H., Mackin, N. A., Maldonado-Báez, L., Evangelista, C. C., Beaudry, V. G., Dudgeon, D. D., Naiman, D. Q., Erdman, S. E., and Cunningham, K. W. (2011). New regulators of a high affinity Ca^{2+} influx system revealed through a genome-wide screen in yeast. J. Biol. Chem. *286*, 10744–10754.

McNeil, J. B., McIntosh, E. M., Taylor, B. V, Zhang, F. R., Tang, S., and Bognar, A. L. (1994). Cloning and molecular characterization of three genes, including two genes encoding serine hydroxymethyltransferases, whose inactivation is required to render yeast auxotrophic for glycine. J. Biol. Chem. *269*, 9155–9165.

Missiaen, L., Robberecht, W., van den Bosch, L., Callewaert, G., Parys, J. B., Wuytack, F., Raeymaekers, L., Nilius, B., Eggermont, J., and De Smedt, H. (2000). Abnormal intracellular Ca^{2+} homeostasis and disease. Cell Calcium *28*, 1–21.

Miyamoto, S., Ohya, Y., Ohsumi, Y., and Anraku, Y. (1987). Nucleotide sequence of the *CLS4* (*CDC24*) gene of *Saccharomyces cerevisiae*. Gene *54*, 125–132.

Miyamoto, S., Ohya, Y., Sano, Y., Sakaguchi, S., Iida, H., and Anraku, Y. (1991). A *DBL*-homologous region of the yeast *CLS4/CDC24* gene product is important for Ca^{2+}-modulated bud assembly. Biochem. Biophys. Res. Commun. *181*, 604–610.

Mnaimneh, S. *et al.* (2004). Exploration of essential gene functions via titratable promoter alleles. Cell *118*, 31–44.

Monschau, N., Sahm, H., and Stahmann, K. (1998). Threonine aldolase overexpression plus threonine supplementation enhanced riboflavin production in *Ashbya gossypii*. Appl. Environ. Microbiol. *64*, 4283–4290.

Nelder, A. J. A., and Wedderburn, R. W. M. (1972). Generalized Linear Models. J. R. Stat. Soc. Ser. A *135*, 370–384.

Nonaka, H., Tanaka, K., Hirano, H., Fujiwara, T., Kohno, H., Umikawa, M., Mino, A., and Takai, Y. (1995). A downstream target of *RHO1* small GTP-binding protein is *PKC1*, a homolog of protein kinase C, which leads to activation of the MAP kinase cascade in *Saccharomyces cerevisiae*. EMBO J. *14*, 5931–5938.

Ohnuki, S., Kobayashi, T., Ogawa, H., Kozone, I., Ueda, J.-Y., Takagi, M., Shin-Ya, K., Hirata, D., Nogami, S., and Ohya, Y. (2012). Analysis of the biological activity of a novel 24-membered macrolide JBIR-19 in *Saccharomyces cerevisiae* by the morphological imaging program CalMorph. FEMS Yeast Res. *12*, 293–304.

Ohnuki, S., Nogami, S., Kanai, H., Hirata, D., Nakatani, Y., Morishita, S., and Ohya, Y. (2007). Diversity of Ca^{2+}-induced morphology revealed by morphological phenotyping of Ca^{2+}-sensitive mutants of *Saccharomyces cerevisiae*. Eukaryot. Cell *6*, 817–830.

Ohnuki, S., Oka, S., Nogami, S., and Ohya, Y. (2010). High-content, image-based screening for drug targets in yeast. PLoS One *5*, e10177.

Ohtani, M., Saka, A., Sano, F., Ohya, Y., and Morishita, S. (2004). Development of image processing program for yeast cell morphology. J. Bioinform. Comput. Biol. *1*, 695–709.

Ohya, Y. *et al.* (2005). High-dimensional and large-scale phenotyping of yeast mutants. Proc. Natl. Acad. Sci. U. S. A. *102*, 19015–19020.

Ohya, Y., Miyamoto, S., Ohsumi, Y., and Anraku, Y. (1986a). Calcium-sensitive *cls4* mutant of *Saccharomyces cerevisiae* with a defect in bud formation. J. Bacteriol. *165*, 28–33.

Ohya, Y., Ohsumi, Y., and Anraku, Y. (1986b). Isolation and characterization of Ca^{2+}-sensitive mutants of *Saccharomyces cerevisiae*. J. Gen. Microbiol. *132*, 979–988.

Ohya, Y., Umemoto, N., Tanida, I., Ohta, a, Iida, H., and Anraku, Y. (1991a). Calcium-sensitive *cls* mutants of *Saccharomyces cerevisiae* showing a Pet- phenotype are ascribable to defects of vacuolar membrane H^+-ATPase activity. J. Biol. Chem. *266*, 13971–13977.

Okada, H., Abe, M., Asakawa-Minemura, M., Hirata, A., Qadota, H., Morishita, K., Ohnuki, S., Nogami, S., and Ohya, Y. (2010). Multiple functional domains of the yeast l,3-beta-glucan synthase subunit Fks1p revealed by quantitative phenotypic analysis of temperature-sensitive mutants. Genetics *184*, 1013–1024.

Okada, H., Ohnuki, S., Roncero, C., Konopka, J. B., and Ohya, Y. (2014). Distinct roles of cell wall biogenesis in yeast morphogenesis as revealed by multivariate analysis of high-dimensional morphometric data. Mol. Biol. Cell *25*, 222–233.

Oltmanns, O., and Bacher, A. (1972). Biosynthesis of riboflavine in *Saccharomyces cerevisiae*: the role of genes rib_1 and rib_7 . J. Bacteriol. *110*, 818–822.

Ostrander, D. B., Gorman, J. A., and Carman, G. M. (1995). Regulation of profilin localization in *Saccharomyces cerevisiae* by phosphoinositide metabolism. J. Biol. Chem. *270*, 27045–27050.

Pan, X., Ye, P., Yuan, D. S., Wang, X., Bader, J. S., and Boeke, J. D. (2006). A DNA integrity network in the yeast *Saccharomyces cerevisiae*. Cell *124*, 1069–1081.

Patton, J. L., and Lester, R. L. (1992). Phosphatidylinositol phosphate, phosphatidylinositol bisphosphate, and the phosphoinositol sphingolipids are found in the plasma membrane and stimulate the plasma membrane H^+-ATPase of *Saccharomyces cerevisiae*. Arch. Biochem. Biophys. *292*, 70–76.

Pittman, J. K., Cheng, N.-H., Shigaki, T., Kunta, M., and Hirschi, K. D. (2004). Functional dependence on calcineurin by variants of the *Saccharomyces cerevisiae* vacuolar Ca^{2+}/H^+ exchanger Vcx1p. Mol. Microbiol. *54*, 1104–1116.

Pozos, T. C., Sekler, I., and Cyert, M. S. (1996). The product of *HUM1*, a novel yeast gene, is required for vacuolar Ca^{2+}/H^+ exchange and is related to mammalian Na^+/Ca^{2+} exchangers. Mol. Cell. Biol. *16*, 3730–3741.

Qadota, H., Python, C. P., Inoue, S. B., Arisawa, M., Anraku, Y., Zheng, Y., Watanabe, T., Levin, D. E., and Ohya, Y. (1996). Identification of yeast Rho1p GTPase as a regulatory subunit of 1,3-beta-glucan synthase. Science *272*, 279–281.

Robertson, A. S., Smythe, E., and Ayscough, K. R. (2009). Functions of actin in endocytosis. Cell. Mol. Life Sci. *66*, 2049–2065.

Sambade, M., Alba, M., Smardon, A. M., West, R. W., and Kane, P. M. (2005). A genomic screen for yeast vacuolar membrane ATPase mutants. Genetics *170*, 1539–1551.

Schuldiner, M. *et al.* (2005). Exploration of the function and organization of the yeast early secretory pathway through an epistatic miniarray profile. Cell *123*, 507–519.

Shitamukai, A., Hirata, D., Sonobe, S., and Miyakawa, T. (2004). Evidence for antagonistic regulation of cell growth by the calcineurin and high osmolarity glycerol pathways in *Saccharomyces cerevisiae*. J. Biol. Chem. *279*, 3651–3661.

Sikorski, R. S., and Hieter, P. (1989). A system of shuttle vectors and yeast host strains designed for efficient manipulation of DNA in *Saccharomyces cerevisiae*. Genetics *122*, 19–27.

Stathopoulos, A. M., and Cyert, M. S. (1997). Calcineurin acts through the *CRZ1/TCN1*-encoded transcription factor to regulate gene expression in yeast. Genes Dev. *11*, 3432–3444.

Suzuki, R., and Shimodaira, H. (2006). Pvclust: an R package for assessing the uncertainty in hierarchical clustering. Bioinformatics *22*, 1540–1542.

Takita, Y. (1997). Genes involved in Ca^{2+} homeostasis in budding yeast *Saccharomyces cerevisiae*. The University of Tokyo.

Takita, Y., Ohya, Y., and Anraku, Y. (1995). The *CLS2* gene encodes a protein with multiple membrane-spanning domains that is important Ca^{2+} tolerance in yeast. Mol. Gen. Genet. *246*, 269–281.

Tanida, I., Hasegawa, A., Iida, H., Ohya, Y., and Anraku, Y. (1995). Cooperation of calcineurin and vacuolar H^{+}-ATPase in intracellular Ca^{2+} homeostasis of yeast cells. J. Biol. Chem. *270*, 10113–10119.

Tanida, I., Takita, Y., Hasegawa, A., Ohya, Y., and Anraku, Y. (1996). Yeast Cls2p/Csg2p localized on the endoplasmic reticulum membrane regulates a non-exchangeable intracellular Ca^{2+} pool cooperatively with calcineurin. FEBS Lett. *379*, 38–42.

Toenjes, K. A., Sawyer, M. M., and Johnson, D. I. (1999). The guanine-nucleotide-exchange factor Cdc24p is targeted to the nucleus and polarized growth sites. Curr. Biol. *9*, 1183–1186.

Tong, A. H. Y. *et al.* (2004). Global mapping of the yeast genetic interaction network. Science *303*, 808–813.

Umemoto, N., Ohya, Y., and Anraku, Y. (1991). *VMA11*, a novel gene that encodes a putative proteolipid, is indispensable for expression of yeast vacuolar membrane H^{+}-ATPase activity. J. Biol. Chem. *266*, 24526–24532.

De Waard, M., Gurnett, C. A., and Campbell, K. P. (1996). Structural and functional diversity of voltage-activated calcium channels. Ion Channels *4*, 41–87.

Wada, Y., Ohsumi, Y., and Anraku, Y. (1992). Genes for directing vacuolar morphogenesis in *Saccharomyces cerevisiae*. I. Isolation and characterization of two classes of *vam* mutants. J. Biol. Chem. *267*, 18665–18670.

Wang, J. M., and Sun, C. (2010). Calcium and neurogenesis in Alzheimer's disease. Front. Neurosci. *4*, 194.

Wertman, K. F., Drubin, D. G., and Botstein, D. (1992). Systematic mutational analysis of the yeast *ACT1* gene. Genetics *132*, 337–350.

Williams, R. J. P. (1999). Calcium: the developing role of its chemistry in biological evolution. In: Calcium as A Cellular Regulator, ed. C. Ernesto, and K. B. Claude, Oxford University Press, 3–27.

Winzeler, E. A. *et al.* (1999). Functional characterization of the *S. cerevisiae* genome by gene deletion and parallel analysis. Science *285*, 901–906.

Xu, H., and Wickner, W. (2006). Bem1p is a positive regulator of the homotypic fusion of yeast vacuoles. J. Biol. Chem. *281*, 27158–27166.

Yang, M., Ohnuki, S., and Ohya, Y. (2014). Unveiling nonessential gene deletions that confer significant morphological phenotypes beyond natural yeast strains. BMC Genomics *15*, 932.

Yoshida, M., Ohnuki, S., Yashiroda, Y., and Ohya, Y. (2013). Profilin is required for Ca^{2+} homeostasis and Ca^{2+}-modulated bud formation in yeast. Mol. Genet. Genomics *288*, 317–328.

Yu, Y., Jiang, Y. W., Wellinger, R. J., Carlson, K., Roberts, J. M., and Stillman, D. J. (1996). Mutations in the homologous *ZDS1* and *ZDS2* genes affect cell cycle progression. Mol. Cell. Biol. *16*, 5254–5263.

Yvert, G., Ohnuki, S., Nogami, S., Imanaga, Y., Fehrmann, S., Schacherer, J., and Ohya, Y. (2013). Single-cell phenomics reveals intra-species variation of phenotypic noise in yeast. BMC Syst. Biol. *7*, 54.

Zhao, Y., Du, J., Zhao, G., and Jiang, L. (2013). Activation of calcineurin is mainly responsible for the calcium sensitivity of gene deletion mutations in the genome of budding yeast. Genomics *101*, 49–56.

Zheng, Y., Bender, A., and Cerione, R. A. (1995). Interactions among proteins involved in bud-site selection and bud-site assembly in *Saccharomyces cerevisiae*. J. Biol. Chem. *270*, 626–630.